Technische Universität München
TUM School of Engineering and Design

Simulative and experimental investigations of the in-situ alloying during the powder bed fusion of metals using a laser beam

Andreas Wimmer

Vollständiger Abdruck der von der TUM School of Engineering and Design der Technischen Universität München zur Erlangung eines

Doktors der Ingenieurwissenschaften (Dr.-Ing.)

genehmigten Dissertation.

Vorsitz: Prof. Dr.-Ing. Nikolaus A. Adams

Prüfende der Dissertation:

1. Prof. Dr.-Ing. Michael F. Zäh
2. Prof. Dr. Christophe Desrayaud
3. Prof. Dr.-Ing. Peter Eberhard

Die Dissertation wurde am 01.07.2024 bei der Technischen Universität München eingereicht und durch die TUM School of Engineering and Design am 21.03.2025 angenommen.

Editors' Preface

In times of global challenges, such as climate change, the transformation of mobility, and an ongoing demographic change, production engineering is crucial for the sustainable advancement of our industrial society. The impact of manufacturing companies on the environment and society is highly dependent on the equipment and resources employed, the production processes applied, and the established manufacturing organization. The company's full potential for corporate success can only be taken advantage of by optimizing the interaction between humans, operational structures, and technologies. The greatest attention must be paid to becoming as resource-saving, efficient, and resilient as possible to operate flexibly in the volatile production environment.

Remaining competitive while balancing the varying and often conflicting priorities of sustainability, complexity, cost, time, and quality requires constant thought, adaptation, and the development of new manufacturing structures. Thus, there is an essential need to reduce the complexity of products, manufacturing processes, and systems. Yet, at the same time, it is also vital to gain a better understanding and command of these aspects.

The research activities at the Institute for Machine Tools and Industrial Management (*iwb*) aim to continuously improve product development and manufacturing planning systems, manufacturing processes, and production facilities. A company's organizational, manufacturing, and work structures, as well as the underlying systems for order processing, are developed under strict consideration of employee-related requirements and sustainability issues. However, the use of computer-aided and artificial intelligence-based methods and the necessary increasing degree of automation must not lead to inflexible and rigid work organization structures. Thus, questions concerning the optimal integration of ecological and social aspects in all planning and development processes are of utmost importance.

The volumes published in this book series reflect and report the results from the research conducted at *iwb*. Research areas covered span from the design and development of manufacturing systems to the application of technologies in manufacturing and assembly. The management and operation of manufacturing systems, quality assurance, availability, and autonomy are overarching topics affecting all areas of our research. In this series, the latest results and insights from our application-oriented research are published, and it is intended to improve knowledge transfer between academia and a wide industrial sector.

Rüdiger Daub *Gunther Reinhart* *Michael Zäh*

Preface

This dissertation was elaborated during my work as a research associate and as a member of the management board of the Institute for Machine Tools and Industrial Management (*iwb*) at the Technical University of Munich.

First of all, I would like to thank Prof. Dr.-Ing. Michael F. Zaeh, full professor of the Chair for Machine Tools and Manufacturing Technology, for giving me the opportunity to pursue a doctorate and for his favorable and generous support during my research work. Additionally, I would like to thank him for the opportunity to be a member of the institute's management board and to be in charge of the Additive Manufacturing Department.

I would also like to thank Prof. Dr. Christophe Desrayaud and Prof. Dr.-Ing. Prof. E.h. Peter Eberhard for their careful review of this dissertation as co-examiners and Prof. Dr.-Ing. Nikolaus A. Adams for chairing the doctoral examination.

Many thanks to the colleagues at the *iwb*, particularly the members of the department for Additive Manufacturing as well as the members of the institute's management board. The valuable discussions with you have been an enrichment to my work.

Finally, I would like to express my sincere gratitude to my family and friends who have given me the strength and support to overcome any situation in life. A big *thank you* goes to my wife Dr. Katharina Wimmer for the continuous support and backing she has provided me.

Munich, May 2025 *Andreas Wimmer*

Content

List of abbreviations

Abbreviation	Description
AM	Additive manufacturing
AA	Aluminum alloy
ALE	Arbitrary Lagrangian Eulerian
ASTM	American Society for Testing and Materials
BCC	Body-centered cubic
BSE	Backscattered Electron Imaging
BTR	Brittle temperature range
CFD	Computational Fluid Dynamics
cf.	compare (lat.: confer)
CMOS	Complementary metal-oxide semiconductor
CTE	Coefficient of thermal expansion
DED	Directed Energy Deposition
DEM	Discrete Element Method
DMLM	Direct Metal Laser Melting
DMLS	Direct Metal Laser Sintering
EDS	Energy Dispersive X-ray Spectroscopy
EDX	Energy Dispersive X-ray
e.g.	for example (lat.: exempli gratia)
FCC	Face-centered cubic
FE	Finite Element
FVM	Finite Volume Method
HAZ	Heat-affected zone
HCS	Hot cracking susceptibility
IA	Industrial application
IMT	Institut Mines-Télécom
IQR	Interquartile range
IR	Infrared
ISO	International Organization for Standardization
iwb	Institute for Machine Tools and Industrial Management of the Technical University of Munich

i.e.	That is (to say) (lat.: id est)
LAMMPS	Large-scale Atomic Molecular Massively Parallel Simulator
LB	Laser beam
LIBS	Laser-induced Breakdown Spectroscopy
LMF	Laser Metal Fusion
MGBs	Migrated grain boundaries
/M	Metallic material
P	Publication
PBF-LB/M	Powder bed fusion of metals using a laser beam
PMZ	Partially melted zone
RA	Research activities
RDG	Rappaz Drezet Gremaud
RFs	Research findings
ROF	Rate of feeding
ROS	Rate of shrinkage
RP	Research progress
SEM	Scanning Electron Microscopy
SGBs	Solidification grain boundaries
SLM	Selective Laser Melting
SOs	Scientific objectives
SPH	Smoothed-Particle Hydrodynamics
SS	Stainless steel
SSGBs	Solidification subgrain boundaries
STEM	Scanning Transmission Electron Microscopy
TIG	Tungsten Inert Gas
TUM	Technical University of Munich
VOF	Volume of Fluid

List of symbols

Latin symbols

Symbol	Unit	Description
a	-	Marangoni number
A	m^2	Surface area
b	-	dendritic network tortuosity
c	m/s	Speed of light in a vacuum
C_0	-	Alloy composition coefficient
C_i	kg/m^3	Concentration of SPH particle i
C_j	kg/m^3	Concentration of SPH particle j
C_L	-	Composition coefficient of the liquid at the solid-liquid interface
d_{50}	m	Particle size corresponding to the cumulative frequency of 50 %
D	m^2/s	Diffusivity
D_i	m^2/s	Diffusivity of SPH particle i
D_j	m^2/s	Diffusivity of SPH particle j
$\mathbf{e}_{ij}$	-	Unit vector between the two SPH particles i and j
$\mathbf{g}$	m/s^2	Vector of the gravitational acceleration
f	-	Function
f_i	-	Function of SPH particle i
f_j	-	Function of SPH particle j
f_L	-	Liquid fraction
f_S	-	Solid fraction
$f_\mathrm{S,coal}$	-	Solid fraction at the coalescence temperature
$f_\mathrm{S,coh}$	-	Solid fraction at the coherence temperature
$\mathbf{F}_\mathrm{a}$	N	Force of additional interfacial effects
F_M	N	Marangoni force
h	Js	Planck constant
h_s	m	Smoothing length
k_B	J/K	Boltzmann constant
k_c	-	Cut-off constant
$k_\mathrm{c}h_\mathrm{s}$	m	Cut-off radius
L	m	Length of the porous network
L_C	m	Characteristic length
m	kg	Mass
m_L	-	Slope of the liquidus line

M	W/m^2	Radiant exitance
M_b	W/m^2	Radiant exitance of a black body
M_r	W/m^2	Radiant exitance of a real body
n	-	Number of neighboring SPH particles
$\mathbf{n}$	-	Unit normal vector
p	N/m^2	Pressure
p_f	N/m^2	Effective feeding pressure
$\tilde{p}_{ij}$	N/m^2	Inter-particle pressure
Δp_c	N/m^2	Critical pressure drop
$\mathbf{r}$	m	Position vector to the fixed point
$\mathbf{r}'$	m	Position vector to the variable point
r_{ij}	m	Distance between particle i and particle j
R	m	Traveling distance of the infrared radiation
ROF	1/s	Rate of feeding
ROS	1/s	Rate of shrinkage
s	-	SPH phase
$t_{0.40}$	s	the time when $f_\mathrm{S} = 0.40$
$t_{0.90}$	s	the time when $f_\mathrm{S} = 0.90$
$t_{0.99}$	s	the time when $f_\mathrm{S} = 0.99$
t_a	s	Available time of the stress relief process
t_f	s	Fragile time period
T	K	Temperature
$\dot{T}$	K/s	Average cooling rate during solidification
T_coal	K	Coalescence temperature
T_coh	K	Coherence temperature
T_E	K	Temperature of the environment
T_L	K	Liquidus temperature
T_O	K	Temperature of the object to be measured
T_S	K	Solidus temperature
ΔT	K	Difference between the solidus and the liquidus temperature
∇T	K/m	Temperature gradient
u_cc	-	Composition coefficient
$\mathbf{v}$	m/s	Velocity vector of an SPH particle
v_iso	m/s	Isothermal velocity
V	m^3	Volume
V_j	m^3	Volume of SPH particle j
w	m·K	Wien's displacement constant
w_epc	-	Equilibrium partitioning coefficient
W	-	Kernel function
Δx	m	SPH particle spacing
x	-	Laser scanning direction during the PBF-LB/M process

y	-	Direction transverse to the laser scanning direction during the PBF-LB/M process
z	-	Building direction during the PBF-LB/M process

Greek symbols

Symbol	Unit	Description
α	m^{-1}	Absorption coefficient
β	-	Shrinkage factor
$\delta(\mathbf{r}-\mathbf{r}')$	-	Dirac delta function
δ_S	-	Surface delta function
ε	-	Emissivity
$\dot{\varepsilon}_{\mathrm{d,\,max}}$	1/s	Maximum strain rate of the dendrites
ε_ext	-	External strain
ε_int	-	Internal strain
$\varepsilon_\mathrm{total}$	-	Total strain
$\mathrm{d}\varepsilon_\mathrm{total}/\mathrm{d}t$	1/s	Critical strain rate
$\mathrm{d}\varepsilon_\mathrm{total}/\mathrm{d}T$	1/K	Critical thermal deformation
ϕ	W	Radiant flux
ϕ_b	W	Black body radiation
ϕ_e	W	Emitted radiation
ϕ_in	W	Incoming radiation
ϕ_m	W	Measured radiation
ϕ_mt	W	Radiation of the measuring track
ϕ_out	W	Outgoing radiation
ϕ_r	W	Reflected radiation
ϕ_t	W	Transmitted radiation
η	kg/(m·s)	Dynamic viscosity
$\tilde{\eta}_{ij}$	kg/(m·s)	Combined dynamic viscosity of SPH particles i and j
γ	N/m	Surface tension
κ	W/(m·K)	Thermal diffusivity
λ	m	Wavelength
λ_2	m	Secondary dendrite spacing
λ_Peak	m	Peak wavelength
Ω	m^2	Integration area
Ψ_i^s	-	Color function of particle i and phase s
ρ	$\mathrm{kg/m^3}$	Density
ρ_0	$\mathrm{kg/m^3}$	Liquid density at the melting point
ρ_av	$\mathrm{kg/m^3}$	Average density between solid and liquid
ρ_i	$\mathrm{kg/m^3}$	Density of SPH particle i
ρ_j	$\mathrm{kg/m^3}$	Density of SPH particle j

ρ_S	kg/m^3	Solid density
σ	W·m^{-2}·K^{-4}	Stefan-Boltzmann constant
τ_A	-	Transmittance

1 Introduction

1.1 Accelerating the alloy design by the in-situ alloying method

The powder bed fusion of metals using a laser beam (PBF-LB/M) allows the fabrication of complex parts with a short lead time and reduced material waste (MEINERS 1999). Initially employed for rapid prototyping, PBF-LB/M achieved a sufficient level of maturity for the series production. Emerging new applications for the PBF-LB/M process drive the need for alloys specifically suitable for this technology.

According to GORSSE ET AL. (2017), customers had access to fewer than 50 commercially available alloys for the PBF-LB/M process in 2017. Besides the small selection, most of these alloys have been tailored to form a fine, stable, and homogeneous microstructure after conventional welding processes. In contrast, PBF-LB/M is characterized by a fast periodic heating and cooling, often resulting in metastable microstructures and defects (MUKHERJEE ET AL. 2016, p. 7). The limited variety of alloys and the lack of process-related optimization have attracted the attention of a growing number of third-party metal powder producers. However, since pre-alloyed metal powders are still primarily produced by gas atomization, they are expensive compared to feedstock forms used in conventional manufacturing processes (WOHLERS ET AL. 2020). According to KATZ-DEMYANETZ ET AL. (2020), the necessity to use pre-alloying as a mandatory route for producing new alloys significantly slows down the PBF-LB/M technology implementation since the process of pre-alloying is time-consuming.

A solution to accelerate the alloy design for PBF-LB/M is given intrinsically by the capability to create alloys via mixed powder feedstocks during the process. This so-called *in-situ alloying* method (SING ET AL. 2021) offers reduced cost, reduced lead time, and high composition flexibility compared to the production of pre-alloyed powders (KANG ET AL. 2017). With this technique, a commercially available alloy can be modified by adding a certain amount of elemental or alloy powder, referred to as an *additive* in this thesis.

Since most defects occurring in the PBF-LB/M process when using unsuitable alloys originate from melt pool instabilities, such as pores during the keyhole regime (MARTIN ET AL. 2019a, ZHAO ET AL. 2017), a reduction of these instabilities is of high interest. Via in-situ alloying, several properties, such as the heat input, the thermal gradient, the surface tension, or the solidification rate, can be altered during the PBF-LB/M process to positively influence the melt pool dynamics. In-situ alloying can also be used to modify the microstructure to tailor the mechanical properties of a part for a specific application (YADROITSEV ET AL. 2021). Furthermore, in-situ alloying is one of the most effective solutions to eliminate cracking during PBF-LB/M (WANG ET AL. 2019).

1.2 Challenges, objectives, and approach

Despite the significant advantages of the in-situ alloying method for the alloy development, there are still major challenges to be overcome:

- Experimental effort: Investigating the mixing and fusion behavior of a potential powder blend is time-consuming. HUBER ET AL. (2021) studied the fusion behavior of high-melting additives by preparing 220 samples and analyzing them with optical light microscopy and scanning electron microscopy. These examinations could be accelerated by methods for automated image recognition; however, the laborious process of preparing specimens and micrographs is still necessary.
- Process understanding: Using additives in a base powder changes the physical properties of the melt pool, such as the thermal conductivity or the laser absorption. To choose a suitable additive for a specific powder, a comprehensive understanding of the mechanisms of action during the melting and solidification process is essential. With only experimental investigations, a deeper analysis of the underlying physics and mechanisms of defect formation becomes difficult.

This dissertation aims at improving the in-situ alloying process by creating a methodology that is capable of investigating any material combination regarding its processability, its influence on the melt pool dynamics, and its susceptibility to defects. To achieve this, a three-stage approach was applied, as illustrated in Figure 1.1. In the first stage, the influence of additives on the melt pool during the PBF-LB/M process was investigated. An experimental methodology was developed that monitors the process zone with a high spatial and temporal resolution, quantifies the melt pool characteristics, and accounts for the peculiarities of the in-situ alloying method. In stage 2, a numerical framework was set up to comprehensively simulate the physical processes during the in-situ alloying in the melt pool. The model was validated with experimental in-situ data determined by the methodology of stage 1. Since the in-situ alloying method is one of the most promising methods to achieve PBF-LB/M samples that are free of hot cracks, stage 3 provides a framework that is capable of predicting the hot cracking susceptibility during the PBF-LB/M process and accounts for a change in the chemical composition.

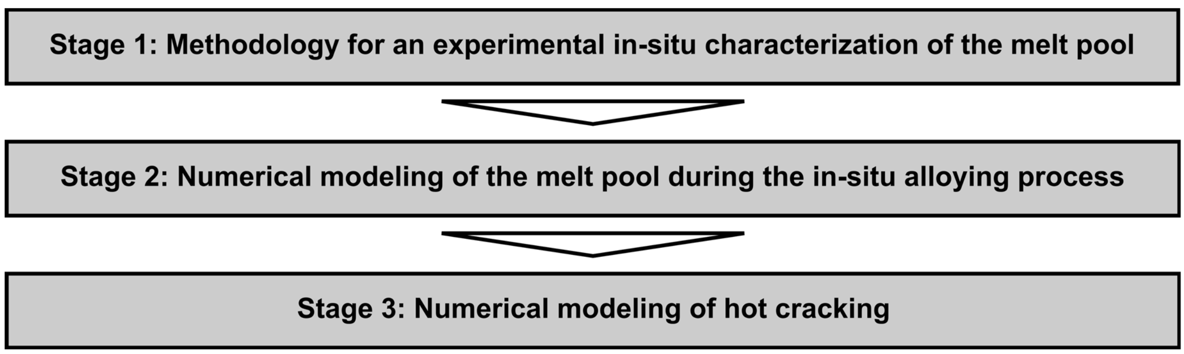

Figure 1.1: Methodological approach of this dissertation

The overall methodology provides an essential contribution to accelerate the design process of new alloys and improves the process understanding for the in-situ alloying method. This methodology can be applied to powder blends as well as to separated powder concentrations, also termed *multi-material*.

1.3 Structure of the thesis

This thesis is based on publications, also termed cumulative.

After the introduction in Chapter 1, Chapter 2 provides fundamentals of the PBF-LB/M process, the infrared (IR) thermography, the hot cracking formation, and the Smoothed-Particle Hydrodynamics (SPH) method. In Chapter 3, the state of the art is presented with a focus on experimental methods to characterize the melt pool during the PBF-LB/M process. Relevant publications regarding in-situ alloying and hot cracking complement the chapter. At the end of Chapter 3, the resulting conclusions and needs for action are discussed. Chapter 4 addresses these needs by introducing the research approach that underlies this thesis in more detail compared to Section 1.2. Here, the scientific objectives are formulated, and an overview of the methodological approach with the embedded publications is given. Chapter 5 represents the publication-based part of this thesis and briefly summarizes the main research findings and conclusions of the author. The publications are concerned with experimental and numerical investigations of the melt pool during the in-situ alloying process and frameworks to predict the hot cracking behavior of metal-based alloys. Chapter 5 ends with an assessment of the achievement of the scientific objectives defined in Chapter 4. Finally, the findings are summarized and discussed in Chapter 6, and an outlook is given on prospective industrial applications and research activities.

2 Fundamentals

2.1 Chapter overview

In this chapter, the fundamentals of the PBF-LB/M process are presented in Section 2.2, the basics of infrared thermography are discussed in Section 2.3, the relevant background of the hot cracking phenomena is provided in Section 2.4, and the SPH method is introduced in Section 2.5.

Based on remarks on the principles of the PBF-LB/M process in Subsection 2.2.1 and the terminology in Subsection 2.2.2, Subsection 2.2.3 provides characteristics of the melt pool and its connection to the process stability and defects. Subsection 2.2.4 introduces the in-situ alloying method based on the fundamentals of the previous subsections. The main assumptions of radiation emission and transport as well as the application of both for thermographic measurements, particularly for determining temperature values, are presented in Subsections 2.3.1 and 2.3.2. Subsection 2.4.1 is dedicated to the definition of the term *hot cracking* and the regions of a fusion weld that are used for describing the solidification path, solidification modes, and grain boundaries. Subsequently, the two main types of hot cracking relevant to this thesis are introduced: solidification cracking in Subsection 2.4.2 and liquation cracking in Subsection 2.4.3. For both cracking types, the currently most promising modeling approaches are described. Subsection 2.5.1 deals with fundamental assumptions of the SPH method and its unique discretization. Due to the presence of multiple material phases during the PBF-LB/M process, Subsection 2.5.2 presents an SPH formulation of the multi-phase flow.

2.2 Powder bed fusion of metals using a laser beam (PBF-LB/M)

2.2.1 Principles of the process

PBF-LB/M is a layer-by-layer additive manufacturing (AM) process for producing geometrically complex parts with a high degree of design freedom. In contrast to conventional manufacturing methods, the PBF-LB/M technology is characterized by the successive addition of material without the need for further tools, e.g., casting molds.

Historically, the invention of the PBF-LB/M process cannot be assigned to a single person. The roots of the layer-wise manufacturing technology of metals go back to the property right DE2263777A1 of CIRAUD (1973) and to the property right US4247508A of HOUSEHOLDER (1981). At that time, the high prices of laser systems and the lack of efficient computers made commercializing the above-presented patents almost impossible. The property right US4863538A of DECKARD (1989) resulted in the first commercial PBF-LB/M machines manufactured by the DTM Corporation in late 1992. The main parts of the machine were a feed cylinder, a part cylinder, a counter-rotating roller, and a CO_2 laser with respective optics. The company merged with the 3D Systems Corporation in the year 2001. The technology was then further developed by the company EOS GmbH, whose first machine was presented in the year 1994. In 2003, the company Trumpf SE + Co. KG introduced the TrumaForm LF 250 and the TrumaForm DMD 505 to the market. In recent years, there have been further technical developments within the machines, but no more substantial changes to the PBF-LB/M process. The PBF-LB/M technology has progressed from being a promising approach in a laboratory to a disruptive technology that is now being used in series production.

According to the DIN EN ISO/ASTM 52900:2022-03 standard, the PBF-LB/M process is divided into three steps: the *pre-process*, the *in-process*, and the *post-process*. The pre-process includes the preparation of the digital model of the part to be manufactured, the slicing of the digital model into single layers, and the filling of the powder into the machine.

Figure 2.1 shows a schematic representation of a PBF-LB/M machine to illustrate the necessary in-process steps for manufacturing a part. First, the building platform is lowered by a thickness of one layer. Subsequently, the powder reservoir is lifted and the recoater deposits one powder layer. The deposited layer is then exposed selectively by the laser beam to melt the solid material. After the solidification, the steps of lowering the building platform, powder deposition, and selective laser exposure are repeated layer by layer until the part is finished.

During the post-process, the part is separated from the building platform and the powder in the building platform is removed. Depending on the use of the part, it may then be post-processed by stress relief heat treatment or other procedures, including surface treatments.

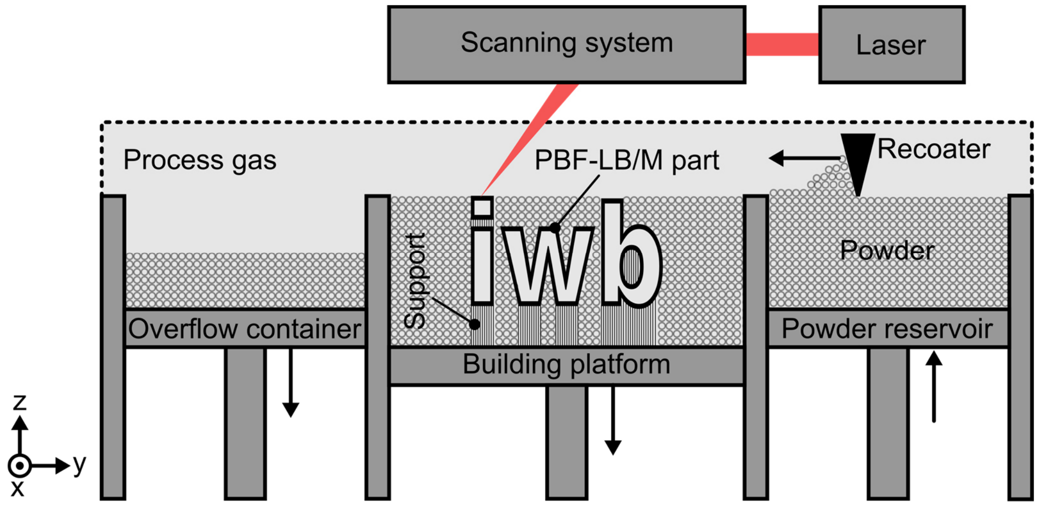

Figure 2.1: Schematic representation of a PBF-LB/M system with its main components

2.2.2 Terminology

The parallel development of the PBF-LB/M technology in several countries has resulted in differing names for the PBF-LB/M process in scientific and popular literature. The terms mainly used are Selective Laser Melting (SLM), LaserCusing, Laser Metal Fusion (LMF), Direct Metal Laser Sintering (DMLS), and Direct Metal Laser Melting (DMLM). For this reason, the terminology was addressed by the first standardization project in the field of AM: ISO and ASTM signed a cooperative agreement in 2011 to develop international AM standards that serve the global market (GUMPINGER ET AL. 2021). The first results were published in 2015 as the ISO/ASTM 52900:2015 "Additive manufacturing – General principles – Terminology". The standard defines terms for all AM technologies that use the principle of building physical three-dimensional geometries by the successive addition of material. The latest version DIN EN ISO/ASTM 52900:2022-03 still defines the terminology of PBF-LB/M as "the process category is powder bed fusion (PBF), using a laser beam (-LB), in a metallic material (/M)".

2.2.3 Melt pool characteristics

When the laser beam scans over the surface of a powder layer, the beam-matter interaction transfers light energy into thermal energy. If the thermal heat input is sufficient to melt the powder particles, the molten substrate and powder create a joint melt pool. The behavior of the melt pool and the solidification process depend on process parameters (e.g., laser power or scanning speed), powder material properties, and the build environment (YADROITSEV ET AL. 2021). These factors affect the evolution of phases, the recoil pressure, the surface tension, and the Marangoni effect, which are primarily responsible for the melt pool size and shape (KHAIRALLAH ET AL. 2016).

Marangoni effect

The mass transfer along an interface between two phases, which results from a surface tension gradient, is called the Marangoni effect. The causes for the surface tension gradient are either a concentration gradient within the material or a temperature gradient. The mass transfer, also called Marangoni flow, transports thermal energy. The Marangoni number a is the ratio of the thermal energy transport to the thermal diffusion and can be expressed as

$$a = -\frac{\partial \gamma}{\partial T} \frac{L_C \Delta T}{\eta \kappa}, \tag{1}$$

with the thermal diffusivity κ, the characteristic length L_C, the temperature T, the surface tension γ, and the dynamic viscosity η (FRIEDLANDER & SERRE 2003). For a large a, the Marangoni flow occurs, while for a small a the thermal diffusion dominates. In the latter case, there is no more Marangoni flow present.

As known from laser welding, the Marangoni effect significantly influences the shape of a melt pool (FUHRICH ET AL. 2001). Figure 2.2 depicts two distinct situations where the surface tension gradient affects the Marangoni flow: In (a), a high surface tension in the center leads to a

Marangoni force F_M towards the center with a subsequent deepening of the melt pool. In (b), high surface tensions at the borders lead to a counter-clockwise Marangoni flow with a subsequent widening of the melt pool.

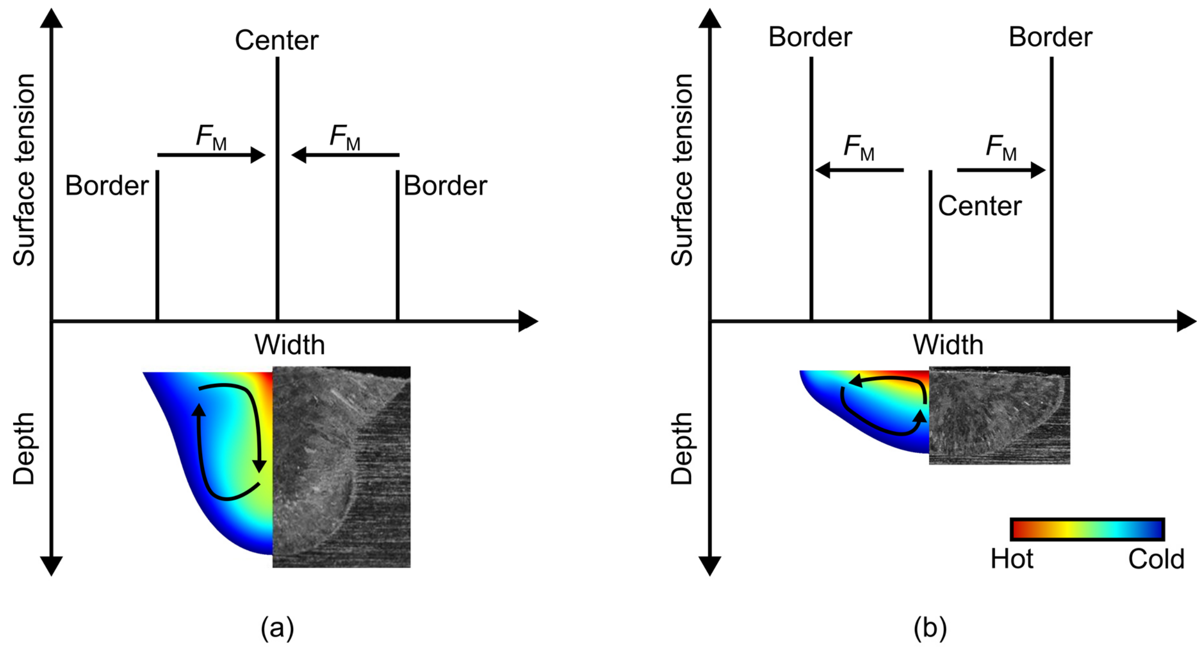

Figure 2.2: Shapes of the melt pool for different surface tensions; (a): high surface tension in the center; (b): high surface tensions at the borders; adapted from LIMMANEEVICHITR & KOU (2000) and from iwb lecture "Lasertechnik" (english: laser technology; access on December 26, 2022)

Conduction and keyhole mode

Similar to the laser welding process, the melt pool in the PBF-LB/M process is characterized by two distinctly different regimes: the conduction mode and the keyhole mode (see Figure 2.3).

In the conduction mode, the penetration depth increases linearly with an increasing energy input (YADROITSEV ET AL. 2021). The penetration depth results from the heat conduction between the powder material and the substrate. The aspect ratio, which is the ratio of the melt pool depth to the melt pool width, is typically 1:2 to 1:1. With an increasing energy input, the melt pool starts to deepen when the aspect ratio exceeds 1:1. This mode is called the transition mode. When the temperature of the melt pool is further increased by an increasing energy input, metal evaporation and plasma may occur. The conservation of momentum of the vaporized material is then responsible for a recoil pressure acting on the melt pool surface. As a consequence, a depression zone in the processed material forms, which results in the keyhole mode. The transition from the conduction mode to the keyhole mode is abrupt and critical, particularly for unstable melt pools.

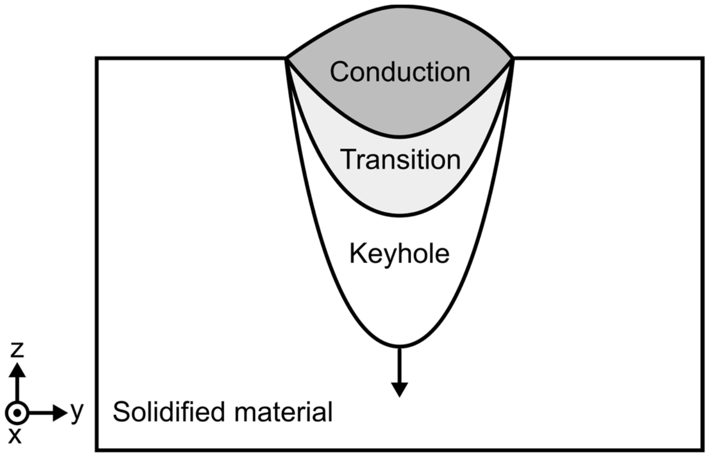

Figure 2.3: Schematic representation of the conduction, the transition, and the keyhole mode; adapted from YADROITSEV ET AL. (2021)

Defects

Figure 2.4 depicts the four primary defects associated with the melt pool. The keyhole is characterized by an unstable vapor cavity that can collapse during the reflowing of melt, leading to gas inclusions. This undesirable formation of porosity is highly provoked during the keyhole mode (KING ET AL. 2014). Regarding the lack of fusion defect, either a low energy input may cause melt pools that are smaller than two adjacent laser tracks, leading to insufficient melting, or a high energy input may result in thermal distortion of the part, separating the local support structures from the heat source and new feed material (COLLINS ET AL. 2016, p. 67). The segmentation of a scan track, also called balling effect, is attributed to the Plateau-Raleigh capillary instability, which causes a tendency to reduce the surface area (TOLOCHKO ET AL. 2004). Hot cracks occur due to the high cooling and solidification rates of the process that prevent the liquid back-feeding in the dendritic arms during the solidification (GIORJAO ET AL. 2021, p. 2515).

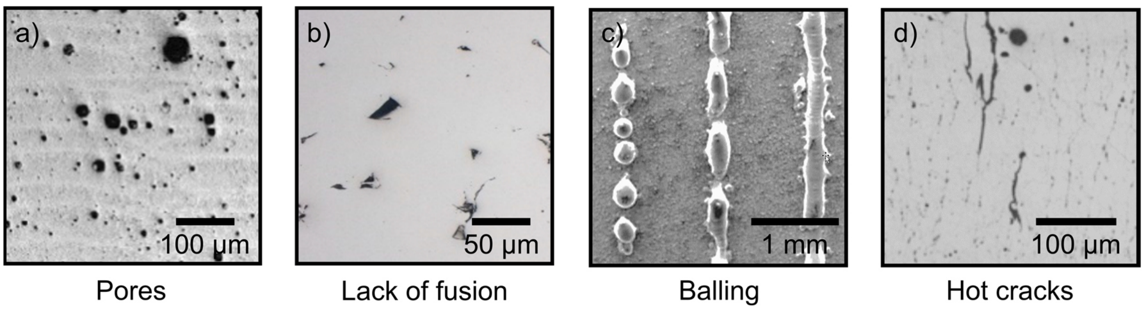

Figure 2.4: Images of the primary defects associated with the melt pool: a) porosity, b) lack of fusion defects, c) increasing balling effect from right to left, and d) hot cracks; the image of the porosity was adapted from WEINGARTEN ET AL. (2015), and the image of the lack of fusion defects from MOHR ET AL. (2020).

The above-mentioned defects may be avoided by finding an optimal process parameter window for a specific material. By means of full factor analysis or orthogonal designs, a high experimental effort is necessary to obtain a well-founded parameter set. A schematic representation of a processing map for an arbitrary material is shown in Figure 2.5. At low scanning speeds and laser powers, irregularities and insufficient melting can occur, leading to lack of fusion defects. At high laser powers and low scanning speeds, the penetration of the melt pool is deep, which may result in porosity. Spatters almost always occur; however, intensive spattering is present at high laser powers with high scanning speeds. Balling and humping effects may arise at low to medium laser powers and high scanning speeds.

Adjusting process parameters to obtain defect-free samples is often accompanied by a significant loss of productivity (COLLINS ET AL. 2016, p. 66). High-strength aluminum alloys (AAs), for example, are hardly processable by only changing the laser power, scanning speed, layer thickness, platform temperature, or scanning strategy during the PBF-LB/M process compared to standard parameters for aluminum processing (AVERSA ET AL. 2019, p. 6).

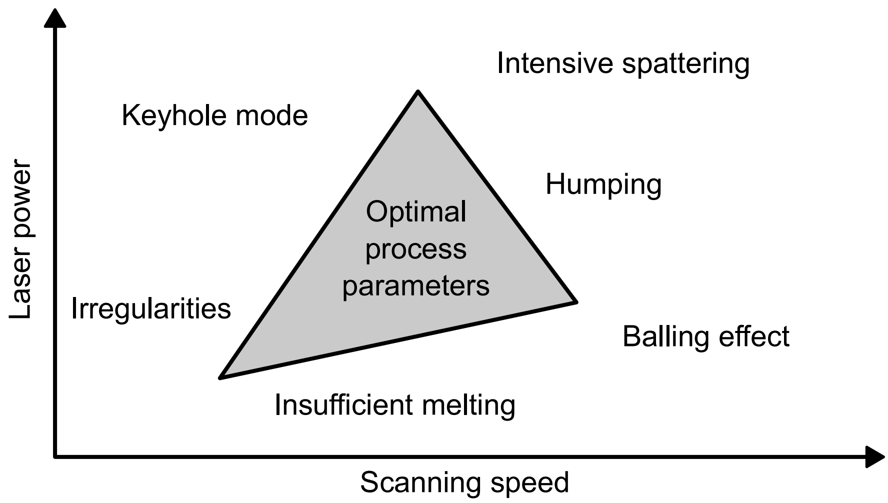

Figure 2.5: Schematic representation of a processing map for single tracks during PBF-LB/M; adapted from YADROITSEV ET AL. (2021)

2.2.4 In-situ alloying

In-situ alloying is defined as the process of combining different materials with various compositions and feeding them simultaneously into the melt pool (YADROITSEV ET AL. 2021).

Figure 2.6 depicts the two main steps for the in-situ alloying method. The mechanical mixing of the two or more powder materials is performed prior to the PBF-LB/M process with, for example, a roller mixer for a few hours. A subsequent analysis via Scanning Electron Microscopy (SEM) can verify the mixing result and the homogeneity of the mixture. Besides the mixing outside of the building chamber, several innovative multi-metal powder deposition systems have been presented, where two materials are mixed and melted during the layer-wise manufacturing process (ZHANG ET AL. 2020, YANG & EVANS 2004, WANG ET AL. 2020).

Adding alloys or elements to a base powder can alter the physical properties of the melt pool, e.g., viscosity, surface tension, and temperature field, resulting in a change of the PBF-LB/M process parameter window (SING ET AL. 2021). In addition, tailored part properties and functionalities can be achieved (BOURELL ET AL. 2017).

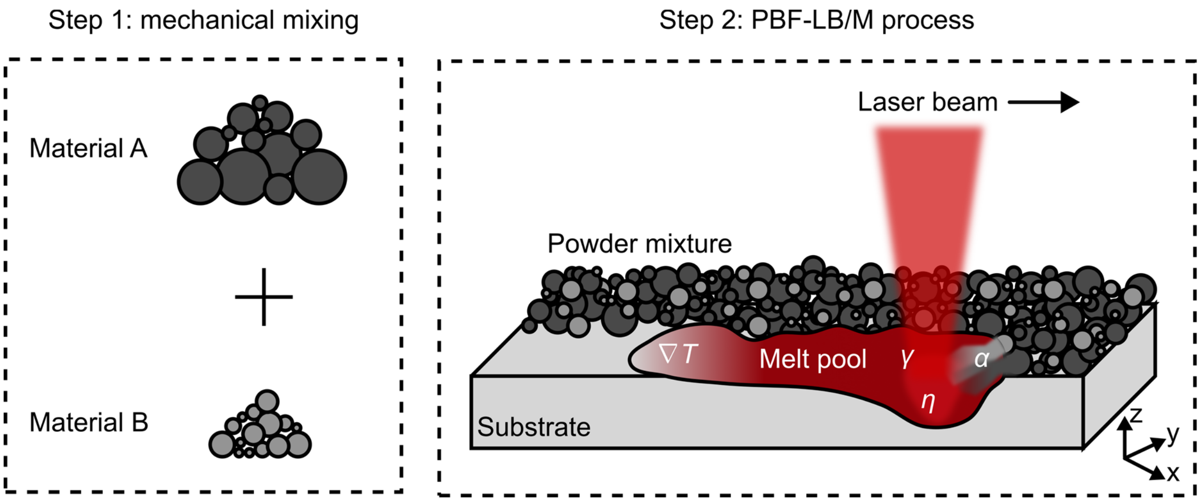

Figure 2.6: Principle of the in-situ alloying method; ∇T is the temperature gradient, η is the dynamic viscosity, γ is the surface tension, and α is the absorption coefficient.

In contrast to the approach of an alloy adaption and a subsequent gas atomization, in-situ alloying is cost-efficient and time-efficient since powders that have already been gas atomized can be used as an additive. The in-situ alloying method has the potential for a rapid design and verification of the processability of new alloys.

2.3 Infrared thermography

2.3.1 Radiation emission and transport

A physical body spontaneously and continuously emits electromagnetic radiation when its temperature is higher than 0 K. In addition to the temperature T of the physical body, the intensity of the electromagnetic radiation also depends on the wavelength λ. The temperature- and wavelength-dependent radiant flux ϕ that is emitted by a surface A per unit area is called radiant exitance M and is expressed as (MINKINA & DUDZIK 2009)

$$M(\lambda, T) = \frac{\mathrm{d}\phi(\lambda, T)}{\mathrm{d}A}. \tag{2}$$

According to theory, a black body completely absorbs the incoming radiation. The spectral radiant exitance of a black body M_b is given by Planck's law:

$$M_\mathrm{b}(\lambda, T) = \frac{2\pi h c^2}{\lambda^5 \left[\exp\left(\frac{hc}{\lambda k_\mathrm{B} T}\right) - 1\right]}, \tag{3}$$

where c is the speed of light in a vacuum, h is Planck's constant, and k_{B} is Boltzmann's constant (KREITH ET AL. 2000).

$M_{\mathrm{b}}(\lambda, T)$ over the wavelength is depicted in Figure 2.7 for different temperatures. At temperatures around 200 °C, a black body emits thermal radiation that is primarily infrared and invisible. With rising temperatures, the amount of infrared and visible radiation increases. Figure 2.7 also shows that the black body radiation curves peak at different wavelengths λ_{Peak} – the higher the temperature, the smaller the wavelength of the thermal radiation. This phenomenon was discovered by Wilhelm Wien several years before Planck and is formulated by Wien's displacement law:

$$\lambda_{\mathrm{Peak}} = \frac{w}{T} \, , \tag{4}$$

where w is the Wien displacement constant (MINKINA & DUDZIK 2009).

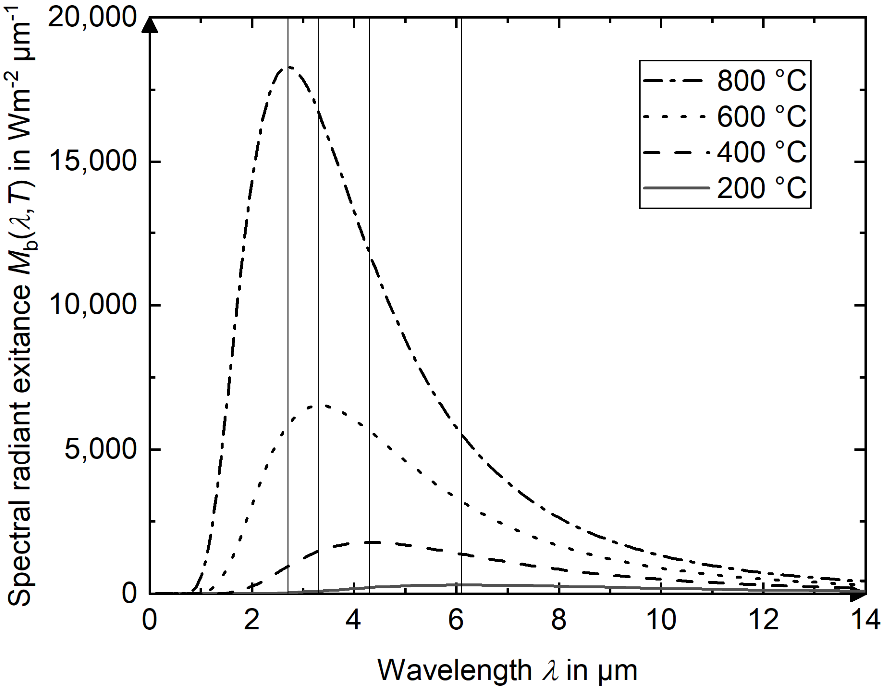

Figure 2.7: Spectral radiant exitance of a black body $M_{\mathrm{b}}(\lambda, T)$ according to Equation (3); the vertical lines indicate the shifting of the curve peak for different temperatures.

The Stefan-Boltzmann law describes the total radiant exitance of a black body at all wavelengths. It is obtained by integrating the wavelength in Equation (3) from zero to infinity (MINKINA & DUDZIK 2009):

$$M_{\mathrm{b}}(T) = \int_{\lambda=0}^{\lambda=\infty} M_{\mathrm{b}}(\lambda, T)\, \mathrm{d}\lambda = \int_{\lambda=0}^{\lambda=\infty} \frac{2\pi h c^2}{\lambda^5 \left[\exp\left(\frac{hc}{\lambda k_{\mathrm{B}} T}\right) - 1\right]}\, \mathrm{d}\lambda = \sigma T^4 \, , \tag{5}$$

where σ is the Stefan-Boltzmann constant. In reality, all physical bodies have a limited absorbing capacity, meaning that they do not satisfy Planck's law for a black body (Equation (3)).

To determine the absorbing capacity of the surface of a real body, the emissivity ε was introduced. It is the ratio of the spectral radiant exitance $M_{\mathrm{r}}(\lambda, T)$ of a real body to the spectral radiant exitance $M_{\mathrm{b}}(\lambda, T)$ of a black body (MINKINA & DUDZIK 2009):

$$\varepsilon(\lambda, T) = \frac{M_{\mathrm{r}}(\lambda, T)}{M_{\mathrm{b}}(\lambda, T)} \ . \tag{6}$$

With regard to ε, physical bodies can be divided as follows:

- black bodies: $\varepsilon(\lambda, T) = 1$,
- gray bodies: $0 < \varepsilon(\lambda, T) < 1$ and $\varepsilon(\lambda, T) = \text{constant}$, and
- real bodies: $0 < \varepsilon(\lambda, T) < 1$ and $\varepsilon(\lambda, T) = \text{variable}$.

Figure 2.8 shows the spectral radiant exitance over the wavelength for a black body, a gray body, and a real body. If the dependencies of the emissivity are known, the emitted radiation from real bodies can be determined by a weighted integration. If the dependencies are unknown, a wavelength-independent emission behavior is assumed in practical applications.

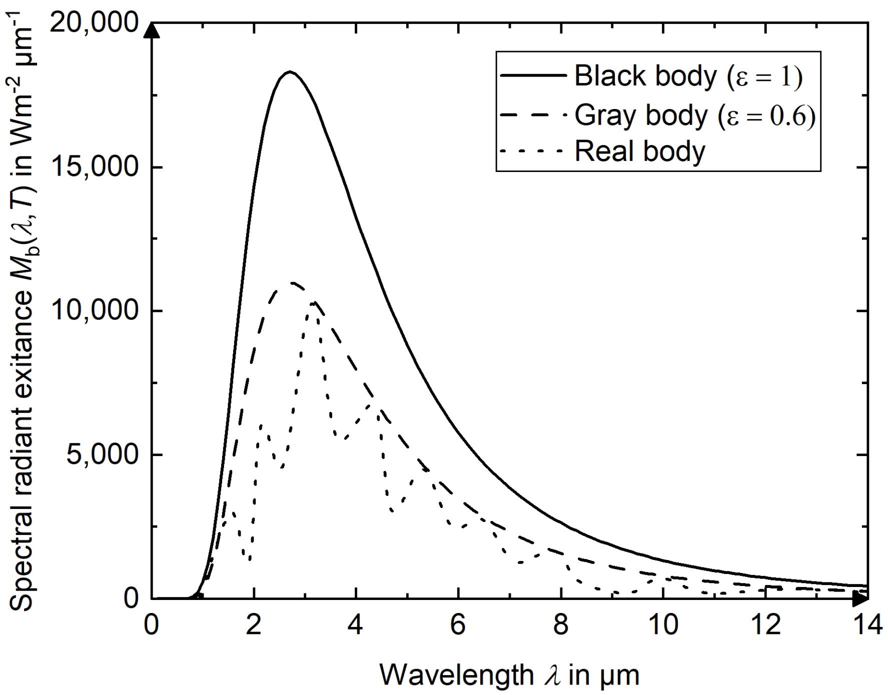

Figure 2.8: Schematic diagram of the spectral radiant exitance $M(\lambda, T)$ of a black body, a grey body, and a real body

When infrared radiation propagates through the atmosphere, it changes its power and spectral composition due to absorption and scattering at gas molecules or other objects. The atmospheric humidity is thereby the main absorbing component (VAVILOV 2020).

The attenuation of infrared radiation is described by the Bouguer law (VAVILOV 2020):

$$\tau_{\mathrm{A}} = e^{-\alpha R} \,, \tag{7}$$

where τ_{A} is the transmittance through a given atmosphere, α is the absorption coefficient of the medium, and R is the traveling distance of the infrared radiation. In practical applications, the transmittance of the atmosphere is often assumed to be free of turbulences and isotropic. This approximation is meaningful for distances less than 20 to 30 m, but it can play a crucial role, e.g., in satellite surveys (VAVILOV 2020).

2.3.2 Thermographic measurement

When measuring the emitted radiation ϕ_{e} of an object, two additional radiation shares must be considered: the reflected radiation ϕ_{r} and the transmitted radiation ϕ_{t}. The former is due to environmental radiation, while the latter is due to background radiation. Figure 2.9 illustrates the several radiations that must be considered when performing a thermographic measurement.

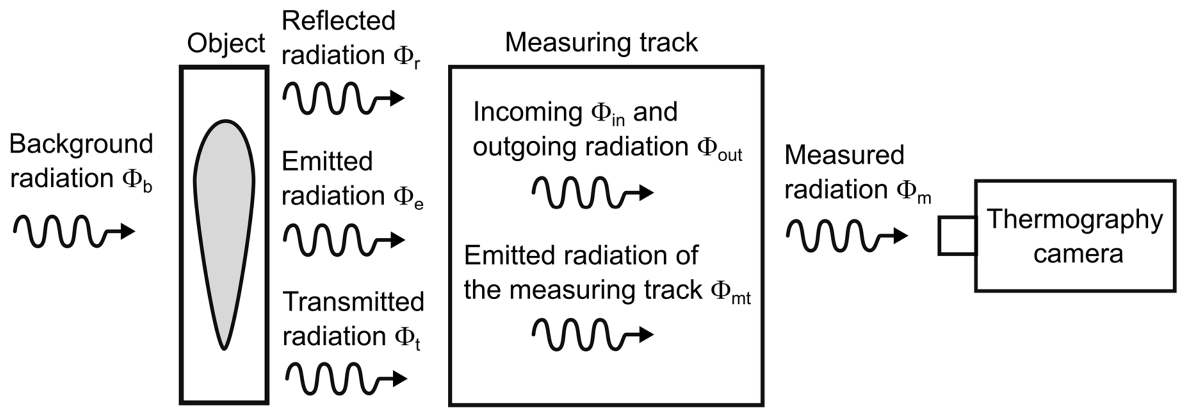

Figure 2.9: Thermographic measurement with radiation shares; adapted from INFRATEC GMBH (2004) and MINKINA & DUDZIK (2009)

Before entering the measuring track in Figure 2.9, the incoming radiation ϕ_{in} adds to (INFRATEC GMBH 2004)

$$\phi_{\mathrm{in}} = \phi_{\mathrm{r}} + \phi_{\mathrm{e}} + \phi_{\mathrm{t}} \,. \tag{8}$$

The incoming radiation ϕ_{in} is attenuated by the measurement track according to Equation (7), resulting in the outgoing radiation

$$\phi_{\mathrm{out}} = \tau_{\mathrm{A}} \cdot \phi_{\mathrm{in}} \,. \tag{9}$$

The measured radiation of the thermography camera is additionally influenced by the radiation emitted by the measuring track itself:

$$\phi_{\mathrm{m}} = \phi_{\mathrm{out}} + \phi_{\mathrm{mt}} \,. \tag{10}$$

In consideration of a non-transparent real body, the equation for a thermographic measuring system simplifies to

$$\phi_{\mathrm{m}} = \tau_{\mathrm{A}} \cdot [\varepsilon \cdot \phi_{\mathrm{b}}(T_{\mathrm{O}}) + (1-\varepsilon) \cdot \phi_{\mathrm{b}}(T_{\mathrm{E}})] + (1-\tau_{\mathrm{A}}) \cdot \phi_{\mathrm{b}}(T_{\mathrm{mt}}) \,, \tag{11}$$

where ϕ_{b} is the black body radiation, T_{O} is the temperature of the object to be measured, T_{E} is the temperature of the environment, and T_{mt} is the temperature of the measuring track. Solving Equation (11) for the temperature of the object to be measured results in the following term to be determined continuously by the thermographic system during the measurement:

$$T_{\mathrm{O}} = \phi_{\mathrm{b}}^{-1}\left(\frac{\frac{\phi_{\mathrm{m}} - (1-\tau_{\mathrm{A}}) \cdot \phi_{\mathrm{b}}(T_{\mathrm{mt}})}{\tau_{\mathrm{A}}} - (1-\varepsilon) \cdot \phi_{\mathrm{b}}(T_{\mathrm{E}})}{\varepsilon}\right). \tag{12}$$

2.4 Hot cracking

2.4.1 Definition and fundamentals

Hot cracking is a highly relevant weldability issue in many structural materials, including Ni-base alloys, steels, and AAs. SAVAGE ET AL. (1976) introduced a terminology to describe fusion weld and microstructure regions, as illustrated in Figure 2.10. These regions are crucial for describing the hot cracking phenomena.

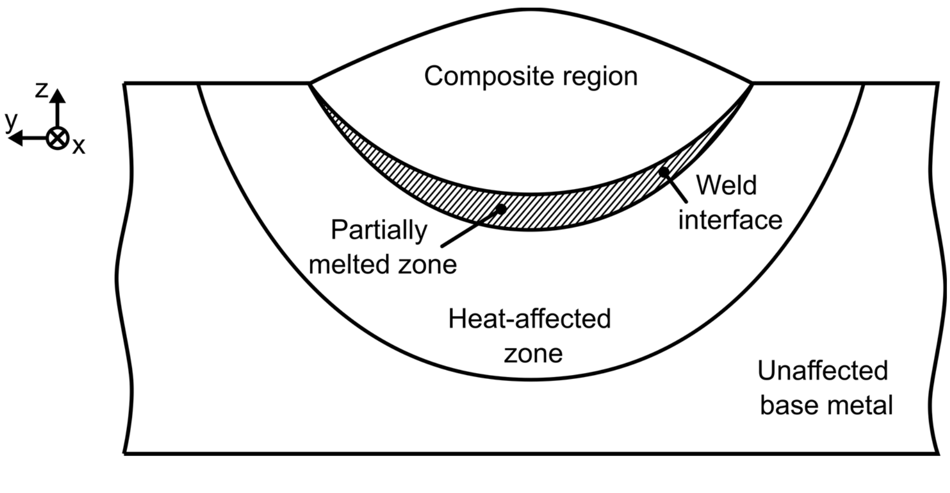

Figure 2.10: Regions of a fusion weld; adapted from SAVAGE ET AL. (1976, p. 7)

The composite region is the area where the base metal is mixed with a filler metal. The transition region between pure liquid and pure solid is described by the partially melted zone (PMZ), also known as the *mushy zone*. It is a mixture of liquid melt and crystalline solids (HILLS ET AL. 1983) and exists in all fusion welds of metal alloys since a transition from pure liquid to pure solid must occur across the fusion boundary. The heat-affected zone (HAZ), which is affected by the heat of the welding process, is a non-melted area separating the PMZ from the base metal.

Hot cracking is most often associated with cracking phenomena that occur during the manufacturing when a liquid is present along the grain boundaries in the fusion zone and in the PMZ (LIPPOLD 2015). These liquid films are considered to be the cause for extending the solidification range of an alloy. In scientific literature, the term *hot cracking* is often used for any crack that forms at elevated temperatures. In this work, the term hot cracking refers to three distinct types of cracking:

- *solidification cracking* that occurs in the fusion zone at the end of the solidification,
- *HAZ liquation cracking* that occurs in the PMZ, and
- *weld metal liquation cracking* that forms during reheating and is mainly observed in multi-layer welding processes or at repair welding.

In the following, essential terms for hot cracking are explained in detail.

Solidification path

The solidification path in Figure 2.11 describes the solid fraction within the PMZ as a function of the temperature. With decreasing temperatures, the solid fraction increases. The liquidus temperature T_L is defined as the temperature where no solid is present, whereby the solidus temperature T_S marks the temperature where no liquid is present.

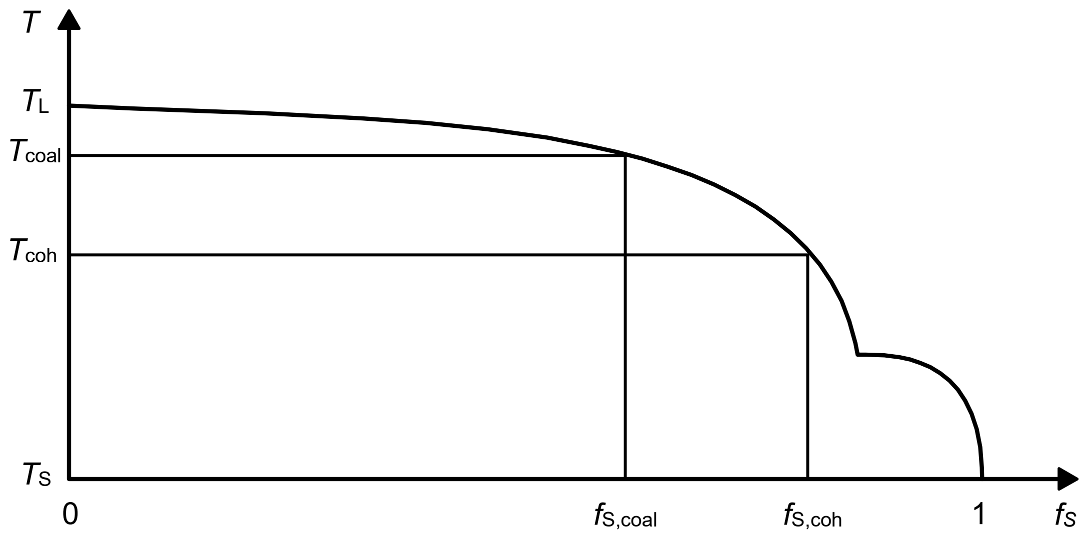

Figure 2.11: Relationship between temperature and solid fraction; adapted from DAHLE & STJOHN (1998, p. 37)

Further distinctive terms are the coalescence temperature T_{coal} and the coherence temperature T_{coh}. T_{coal} is defined as the temperature at which the dendrites join and build up the yield strength of the manufactured part. At T_{coh}, crystalline solids interlock with each other, leading to a rigid body. $f_{\mathrm{S,coal}}$ and $f_{\mathrm{S,coh}}$ are the corresponding solid fractions, respectively. Between T_{coh} and T_{S}, the yield strength increases rapidly and exhibits a more solid-like behavior. (DAHLE & STJOHN 1998, pp. 33–41)

Solidification modes

During the solidification of metals, multiple solidification modes can occur, as shown in Figure 2.12. The planar growth is apparent under conditions of low solidification rates, steep temperature gradients, or both. In most solidification processes, the plane front transforms into a cellular and then into more complex dendritic morphologies. In fusion welds and casting, cellular and cellular dendritic growth are the dominant solidification modes (LIPPOLD 2015).

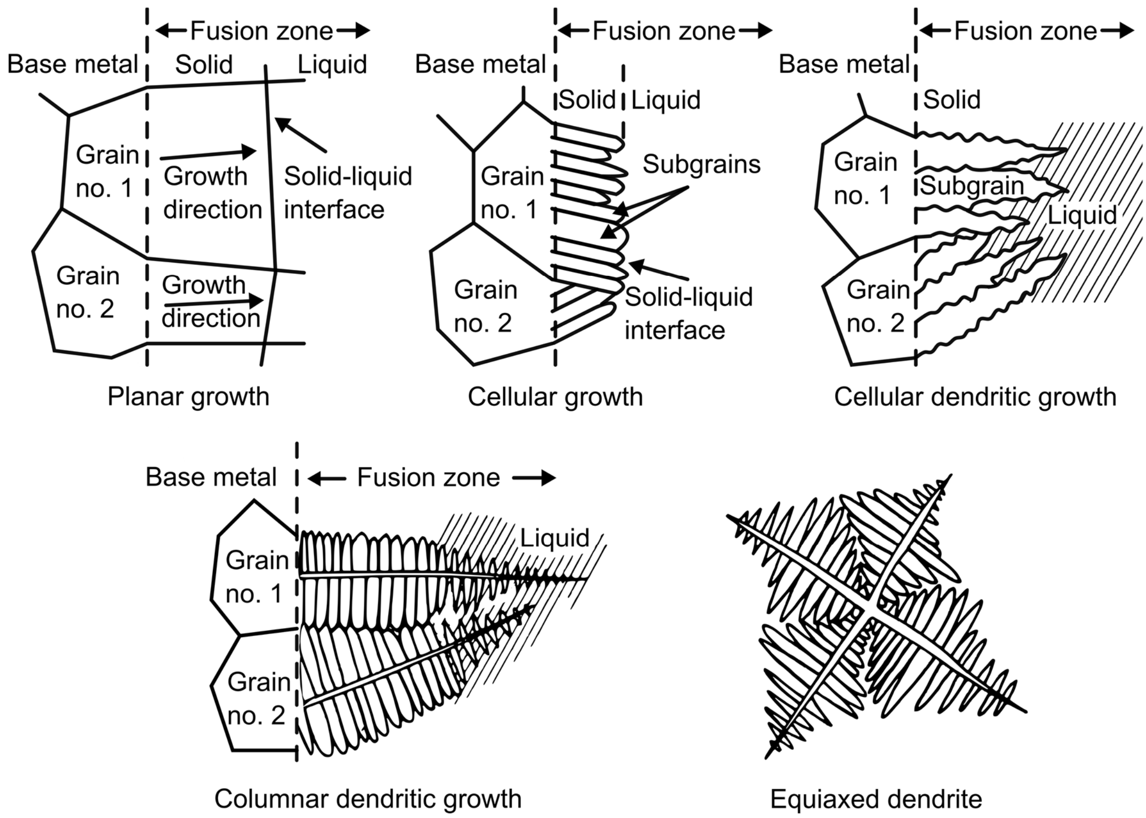

Figure 2.12: Solidification modes; adapted from LIPPOLD (2015, p. 20)

The particular solidification mode can be determined by the degree of constitutional undercooling (CHALMERS B. 1964). In metal alloys, the product of the temperature gradient and the solidification rate can also determine the solidification mode. The value of the product is termed as the cooling rate.

As illustrated in Figure 2.13, the equiaxed dendrite growth takes place when the solidification rate is high and the temperature gradient is low. If the temperature gradient is very high, planar growth is possible. An increasing cooling rate leads to finer structures, resulting in cellular or dendritic structures that are spaced more closely. Besides the temperature gradient and the solidification rate, the composition of the alloy influences the solidification mode.

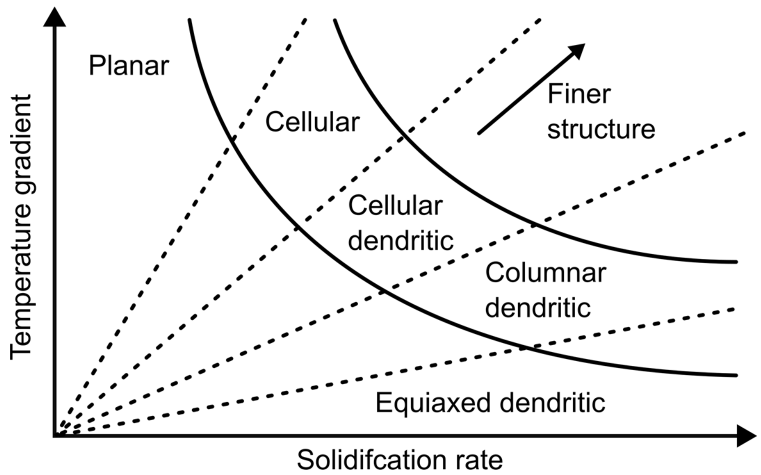

Figure 2.13: Solidification mode in dependence of the product of the temperature gradient and the solidification rate; adapted from LIPPOLD *(2015, p. 21)*

Grain boundaries

On a microscopic level, three different boundary types can be observed metallographically. These boundaries are associated with the defects occurring in and around the fusion zone. Figure 2.14 depicts a schematic representation of the boundaries present during the welding of a single-phase metal.

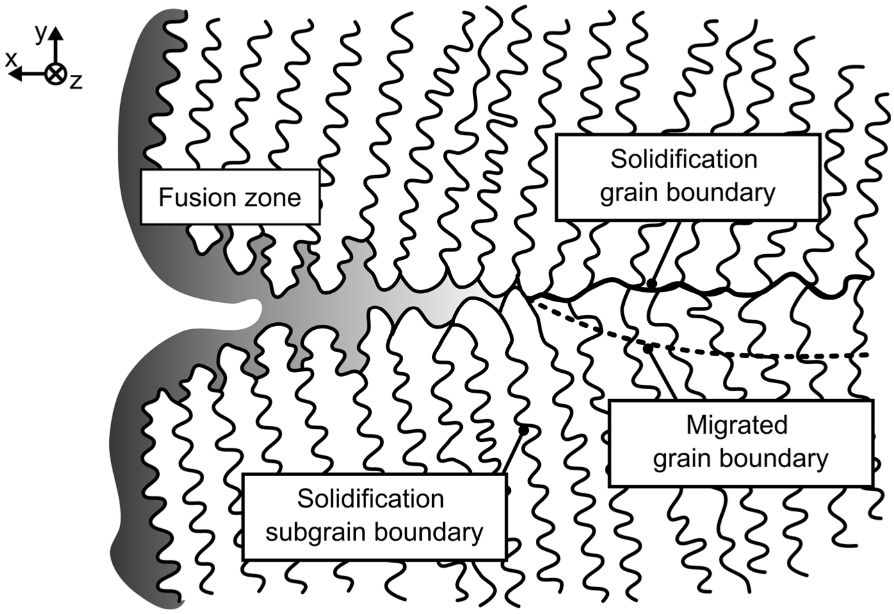

Figure 2.14: Schematic representation of boundaries occurring at the fusion zone on a microscopic level; adapted from LIPPOLD *(2015, p. 33)*

The finest resolvable boundaries in the microstructure are the solidification subgrain boundaries (SSGBs), which result from the formation of cells and dendrites during the solidification. Solidification grain boundaries (SGBs) form due to intersections of several SSGBs. The true crystallographic grain boundaries in the fusion zone are called migrated grain boundaries (MGBs) and retain the misorientation of the original SGBs, from which they migrated after solidification. The driving force for the migration is a lowering of the boundary energy by straightening and pulling away from the original SGB. A reheating, e.g., during the PBF-LB/M process, may lead to further boundary migration. (LIPPOLD 2015)

Weldability of aluminum

The weldability of aluminum alloys mainly depends on their susceptibility to hot cracking. By adding chemical elements to the alloy, the thermo-physical properties of the melt pool and, thus, the susceptibility to hot cracking can be influenced. MONTERO-SISTIAGA ET AL. (2016) showed that the density of the AA 7075 is significantly increased after the welding process by adding Si to the base material prior to the welding process. However, Figure 2.15 shows that the addition of Si or Mg to aluminum alloys only reduces the susceptibility to hot cracking from a certain amount of the respective element. The addition of a small amount of an element can lead to an increased susceptibility to hot cracking.

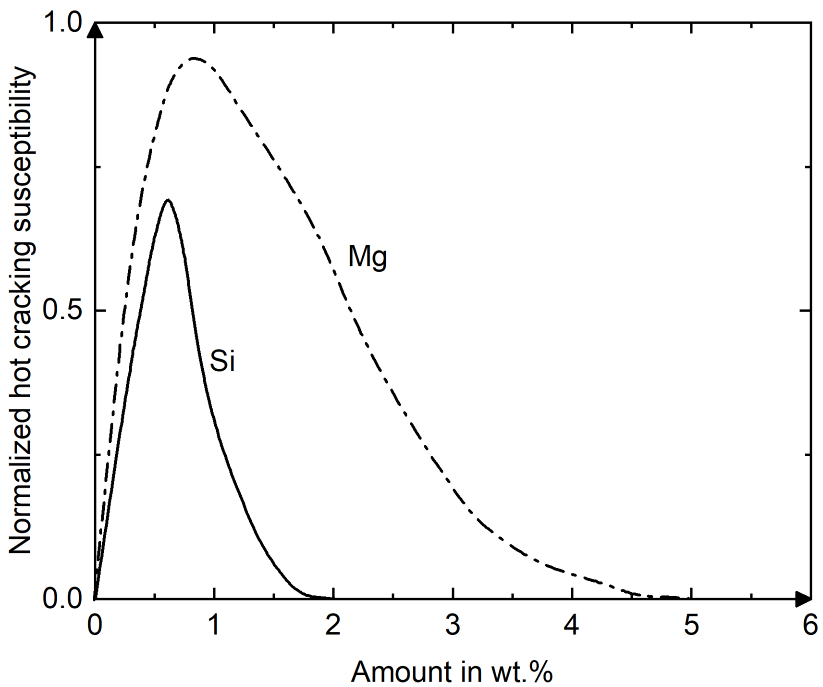

Figure 2.15: Hot cracking susceptibility of AlSi and AlMg alloys depending on the amount of Si and Mg; adapted from CICALĂ ET AL. (2005)

2.4.2 Solidification cracking

Solidification cracking occurs mainly along SGBs and, rarely, along SSGBs. Although this topic has been investigated over the past 50 years, the precise micro-mechanisms responsible for the solidification cracking are still not completely understood. In some cases, the susceptibility for solidification cracking can be minimized by changing the welding parameters, e.g., laser power or scanning velocity. However, a permanent solution to prevent the solidification cracking is usually not achieved. An adaption of the composition of the alloy to control the solidification process is often the preferred solution.

Since the 1940s, several theories for solidification cracking have been proposed (LIPPOLD 2015):

- **Shrinkage-brittleness theory**: According to this theory, cracking always occurs within an *effective interval* below T_{coh}. Within this interval, solid-solid bridging allows the strain to accumulate in the structure. At temperatures above T_{coh}, enough liquid is present to fill the cracks and, thus, avoid them.
- **Strain theory**: During solidification, a mushy stage and a liquid film stage are considered. The former occurs at temperatures above that of the liquid film stage, where a high amount of liquid is still present. During the liquid film stage, the solid grains are separated by a liquid film. When the local strain is high enough, separation along the solid-liquid interfaces may occur with a liquid film separating the solid grains. In contrast to the shrinkage-brittleness theory, cracking is of a solid-liquid type rather than a solid-solid type.
- **Generalized theory of super-solidus cracking**: In this theory, aspects of both the shrinkage-brittleness theory and the strain theory are considered. It conceives the idea of combining the T_{coh} with an additional solidification stage below this temperature, called *critical solidification range*. Within this range, the small amount of liquid is not able to fill fractures of the solid-solid bridges.
- **Modified generalized theory**: The previous theory was further developed by (MATSUDA ET AL. 1982) based on experiments with direct observation of the solidification cracking using high-speed cameras. The *critical solidification range* was divided into a film stage and a droplet stage. According to this theory, solidification cracking only occurs in the film stage due to the intensive solid-solid contact. However, the crack propagation may proceed in both stages.
- **Technological strength theory**: This theory considers the ductility of a material during the solidification. Possible cracking is seen as a result of the competition between the accumulation of thermally and/or mechanically induced strain and the recovery of ductility during the cooling. If the ductility of the material is exhausted due to a continuously applied strain, cracking may occur. The possibility that a material will resist the cracking is influenced by the solidification temperature range and the nature of grain boundary liquid films.

In conclusion to the above-presented theories, all mechanisms require a liquid film along the SGBs during solidification. If this liquid film is not sufficient to support the fractures caused by an accumulated strain, solidification cracking may occur. Controlling the liquid films along the SGBs is, therefore, the key to avoiding solidification cracking. As shown at a later stage in this dissertation (cf. Subsection 5.2.5), altering the thermo-physical properties of the melt pool by adding chemical elements is a promising approach for controlling these liquid films along the SGBs.

2.4.3 Liquation cracking

In the following, two types of liquation cracking, *HAZ liquation cracking* and *weld metal liquation cracking,* are discussed.

HAZ liquation cracking

This cracking type happens along the grain boundaries in the PMZ near the HAZ. By definition, the occurring cracks are intergranular and result from localized melting along the grain boundary interface of the PMZ and the HAZ. In the scientific literature, two mechanisms are proposed to describe this phenomenon: the penetration mechanism and the segregation mechanism. (LIPPOLD 2015, p. 84)

Figure 2.16 shows a schematic representation of the penetration mechanism consisting of three events. First, constitutional liquation occurs at a liquated particle outside the mobile grain boundary. This happens due to a lower melting temperature compared to the surrounding area.

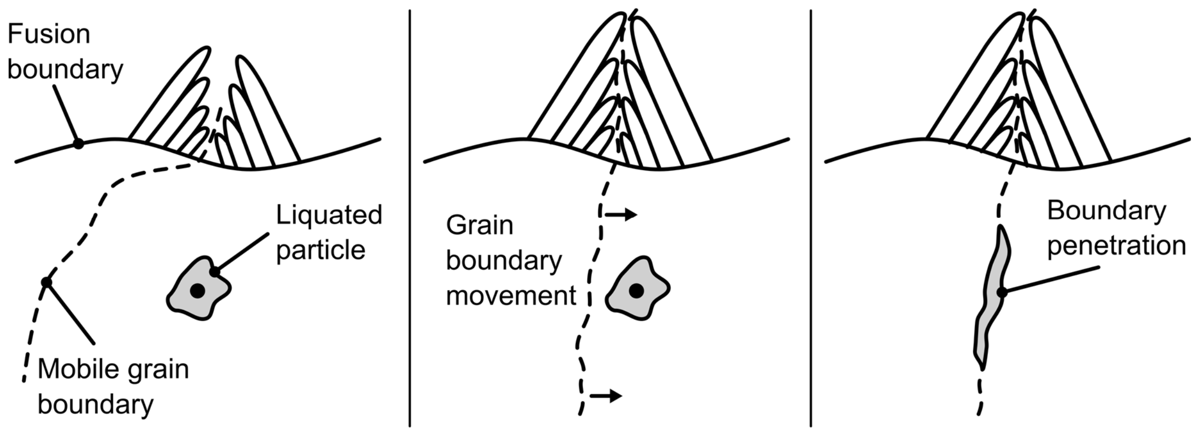

Figure 2.16: Schematic representation of the penetration mechanism; adapted from LIPPOLD (2015, p. 50)

In a second event, the grain boundary moves while the grain grows. Thirdly, the moving grain boundary and the liquated particle must be in contact. Depending on the physical properties of the used material, the liquid may then penetrate along the boundary, leading to a grain boundary liquid film. (LIPPOLD 2015, pp. 49–50)

In the segregation mechanism, the mobile grain boundary is supplemented with elements that reduce the melting point. These elements diffuse or segregate to the grain boundary while the boundary is moving, as illustrated in Figure 2.17. A liquid film is formed along the grain boundaries when the elements and the boundary come into contact.

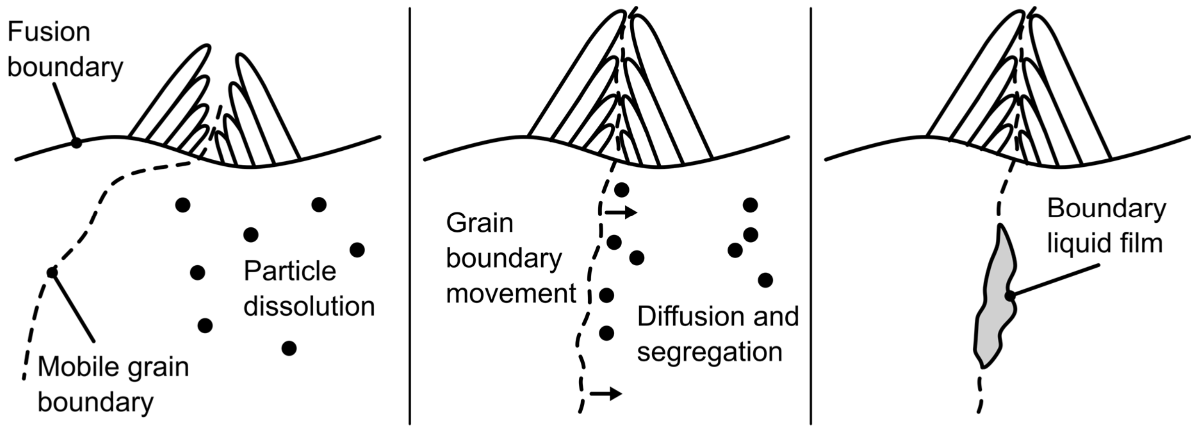

Figure 2.17: Schematic representation of the segregation mechanism; adapted from LIPPOLD (2015, p. 55)

Weld metal liquation cracking

Liquation cracking that forms when either SGBs or MGBs are reheated close to the fusion zone, as in multi-layer processes, is defined as weld metal liquation cracking. Within this mechanism, hot cracking occurs due to a clustering of impurity elements or segregations along the SGBs or MGBs. According to LIPPOLD (2015, pp. 122–127), the composition of the weld metal has the most significant influence on the liquation cracking susceptibility.

2.5 Smoothed-particle hydrodynamics

2.5.1 Discretization and fundamental assumptions

The SPH method was introduced in the 1970s by LUCY (1977) and GINGOLD & MONAGHAN (1977). The unique characteristic of this Lagrangian method is the discretization of the continuum to be simulated into a finite number of particles. These particles, also named SPH particles, represent the physical properties of interest by weighted interactions with neighboring particles. The weighting is performed by a kernel function W. Figure 2.18 shows a graphical representation of the kernel function and its integration area. Only those SPH particles j that are within the cut-off radius $k_\mathrm{c} h_\mathrm{s}$, with the cut-off constant k_c, contribute to the physical properties of the SPH particle i.

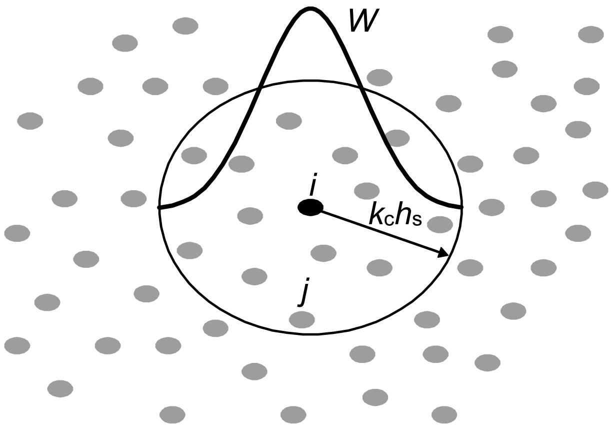

Figure 2.18: Illustration of the kernel function and its domain of influence; adapted from DUTRA FRAGA FILHO (2019, p. 18)

The SPH method is based on the mathematical identity, which is represented by the following equation:

$$f(\mathbf{r}) = \int_{\Omega} f(\mathbf{r}') \cdot \delta(\mathbf{r} - \mathbf{r}')\mathrm{d}\mathbf{r}' , \tag{13}$$

where $\mathbf{r}$ is the position vector to the fixed point, $\mathbf{r}'$ is the position vector to the variable point, $\delta(\mathbf{r} - \mathbf{r}')$ is the Dirac delta function, and Ω is the integration area (DUTRA FRAGA FILHO 2019, p. 18).

In the SPH method, the Dirac delta function is replaced by the kernel function W, also named the smoothing function:

$$f(\mathbf{r}) = \int_{\Omega} f(\mathbf{r}') \cdot W(\mathbf{r} - \mathbf{r}', h_\mathrm{s})\mathrm{d}\mathbf{r}' , \tag{14}$$

where h_s is the smoothing length, which is a measure for the width of the kernel (DUTRA FRAGA FILHO 2019). The kernel function defines the contribution of the neighboring particles to the values of the physical properties of the particle under consideration. The kernel function must satisfy the properties

- positivity: $W(\mathbf{r} - \mathbf{r}', h_\mathrm{s}) \geq 0$,
- symmetry: $W(\mathbf{r} - \mathbf{r}', h_\mathrm{s}) = W(\mathbf{r}' - \mathbf{r}, h_\mathrm{s})$,
- unity: $\int_{\Omega} W(\mathbf{r} - \mathbf{r}', h_\mathrm{s})\mathrm{d}\mathbf{r}' = 1$,
- compact support: $W(\mathbf{r} - \mathbf{r}', h_\mathrm{s}) = 0$, if $|\mathbf{r} - \mathbf{r}'| > k_\mathrm{c} h_\mathrm{s}$, and
- delta function property: $\lim_{h \to 0} W(\mathbf{r} - \mathbf{r}', h_\mathrm{s}) = \delta(\mathbf{r} - \mathbf{r}')$.

Any function that fulfills the above-mentioned properties can be used as a kernel function for the SPH method.

Discretization of the continuum

When discretizing the continuum with SPH particles, the value of a given function f can be calculated at the respective positions of the mass centers of the Lagrangian elements. These mass centers are infinitesimal volume elements defined as

$$\mathrm{d}\mathbf{r}' = \frac{m(\mathbf{r}')}{\rho(\mathbf{r}')} \,, \tag{15}$$

where $m(\mathbf{r}')$ is the mass and $\rho(\mathbf{r}')$ is the density of the infinitesimal volume element. (DUTRA FRAGA FILHO 2019)

By using the discretization of Equation (15), Equation (14) can be rewritten as

$$f_i \approx \sum_{j=1}^{n} m_j \frac{f_j}{\rho_j} W\big(\mathbf{r}_i - \mathbf{r}_j, h_\mathrm{s}\big) \,, \tag{16}$$

where f_i is the approximate value of the function at particle i, f_j is the approximate value of the function at the neighboring SPH particle j, m_j and ρ_j are the mass and the density of the neighboring SPH particle, respectively, and n is the number of neighboring SPH particles. The SPH particles represent not only the breakpoints for an interpolation but their temporal movement within the domain also represents a fluid flow (MONAGHAN 2005).

The approximation quality depends on the number of SPH particles within the integration area and the cut-off radius. According to LIU & LIU (2003), a number of 57 neighboring SPH particles is a good compromise between accuracy and computional speed for the three-dimensional case when the particles are placed in a lattice with a smoothing length of 1.2 times the particle spacing, and $k_\mathrm{c} = 2$.

Derivatives

The basic form of the approximation of the gradient of Equation (16) is given by

$$\nabla f_i \approx \sum_{j=1}^{n} m_j \frac{f_j}{\rho_j} \nabla W\big(\mathbf{r}_i - \mathbf{r}_j, h_\mathrm{s}\big) \,. \tag{17}$$

It should be noted that W must be differentiable (ADAMI 2014). According to MONAGHAN (1992, p. 545), another variant of Equation (17) can be achieved by using the identity

$$\varphi \nabla f = \nabla(\varphi f) - f \nabla \varphi \,, \tag{18}$$

which yields

$$\nabla f_i \approx \varphi_i \sum_{j=1}^{n} m_j \left(\frac{f_i}{{\varphi_i}^2} + \frac{f_j}{{\varphi_j}^2} \right) \nabla W\left(\mathbf{r}_i - \mathbf{r}_j, h_\mathrm{s}\right), \tag{19}$$

where φ is a differentiable scalar quantity (ADAMI 2014).

Mass conservation

In SPH, each particle carries a constant portion of mass which remains unaffected during a simulation. Therefore, the mass conservation is intrinsically satisfied. The classic form of the density field approximation, also called the density summation approach, is obtained by substituting f for ρ in Equation (16):

$$\rho_i = \sum_{j=1}^{n} m_j\, W\left(\mathbf{r}_i - \mathbf{r}_j, h_\mathrm{s}\right). \tag{20}$$

Momentum conservation

The momentum conservation of an isothermal fluid can be expressed by the Navier-Stokes equation as

$$\frac{\mathrm{d}(\rho\mathbf{v})}{\mathrm{d}t} = -\nabla p + \eta \nabla^2 \mathbf{v} + \rho \mathbf{g} + \mathbf{F}_\mathrm{a}, \tag{21}$$

with the velocity vector $\mathbf{v}$ of an SPH particle, the pressure p, the dynamic viscosity η, and the gravitational acceleration vector $\mathbf{g}$ (ADAMI 2014). The vectorial force $\mathbf{F}_\mathrm{a}$ describes additional interfacial effects such as the surface tension.

Using the formulation for derivatives in SPH according to Equation (19) and inserting it into Equation (21), the acceleration of an SPH particle is given by

$$\frac{\mathrm{d}\mathbf{v}_i}{\mathrm{d}t} = \mathbf{g}_i - \frac{1}{m_i} \sum_{j=1}^{n} \left(V_i^2 + V_j^2\right) \frac{\partial W}{\partial r_{ij}} \left[\tilde{p}_{ij} \mathbf{e}_{ij} + \eta \frac{\mathbf{v}_i - \mathbf{v}_j}{r_{ij}} \right], \tag{22}$$

with the unit vector $\mathbf{e}_{ij}$ between the two SPH particles i and j, the distance $r_{ij} = \left|\mathbf{r}_i - \mathbf{r}_j\right|$ between particle i and particle j, the reformulation of the gradient of the kernel $\nabla W\left(\mathbf{r}_i - \mathbf{r}_j, h_\mathrm{s}\right) = \frac{\partial W}{\partial r_{ij}} \mathbf{e}_{ij}$, and the volume V of the respective SPH particle (ADAMI 2014). For a single SPH phase, the inter-particle pressure is given by $\tilde{p}_{ij} = \frac{1}{2}\left(p_i - p_j\right)$.

Difficulties arise when the standard SPH formulation from above is applied to multi-phase flows. Significant differences in the physical density between, e.g., two materials, are not permitted because the standard SPH formulation implicitly assumes that the density gradient is much smaller than that of the smoothing kernel (MONAGHAN 1994, MONAGHAN & KOCHARYAN 1995). To account for this problem, new SPH formulations for the multi-phase flows were formulated.

2.5.2 Formulation of the multi-phase flow

To handle multi-phase problems effectively with SPH, the single-phase model needs to be modified. First, each SPH phase must be tagged with a marker to identify the respective SPH phase. Second, the physical models must be modified in a way that interactions of SPH particles within the same phase happen in the single-phase model, and interactions of SPH particles of two different SPH phases take into account the different properties of the respective SPH phase (ADAMI 2014). HU & ADAMS (2006) presented a multi-phase formulation that can be applied to any type of interaction. For example, the dynamic viscosity η of the single-phase in Equation (22) can be replaced by the combined viscosity (ADAMI 2014):

$$\tilde{\eta}_{ij} = \frac{2\eta_i\eta_j}{\eta_i + \eta_j}. \tag{23}$$

The combined viscosity $\tilde{\eta}_{ij}$ is reduced to that of a single-phase if the SPH particles i and j belong to the same phase. When using the density summation of Equation (20) in multi-phase problems, HU & ADAMS (2006) used a formulation where neighboring SPH particles only affect the specific volume of the SPH particle i:

$$\rho_i = m_i \sum_j W\left(\mathbf{r}_i - \mathbf{r}_j, h_s\right). \tag{24}$$

The formulation is independent of the mass of the neighboring SPH particles and, therefore, well suited for problems where neighboring SPH particles differ significantly in the value for the mass. In the PBF-LB/M process, this is highly relevant due to the temperature dependence and physical phase dependence of the density value. For example, the interface between SPH particles in the solid and liquid may have a large density gradient – between gas and liquid even higher.

Color function

With the concept of a color function, it is possible to model interface phenomena, such as surface tension or laser-matter interaction. The underlying approach is to perform a unit jump at the interface of two SPH phases.

The color function Ψ is defined as

$$\Psi_i^s = \begin{cases} 1, & \text{if particle } i \text{ belongs to phase } s, \\ 0, & \text{else,} \end{cases} \tag{25}$$

with $s = 1, \dots, S$ (HU & ADAMS 2006). According to BRACKBILL ET AL. (1992) and ADAMI (2014), the normal direction of the interface can be described by the gradient of the color function as

$$\mathbf{n}\delta_S = \nabla\Psi\,, \tag{26}$$

with the surface delta function δ_S and the unit normal vector

$$\mathbf{n} = \frac{\nabla\Psi}{|\nabla\Psi|}\,. \tag{27}$$

The concept is illustrated in Figure 2.19, where a two-fluid situation is present. Using a surface delta function, the concept of a color function combines a sharp SPH phase transition with a smooth discretization interface within the transition band.

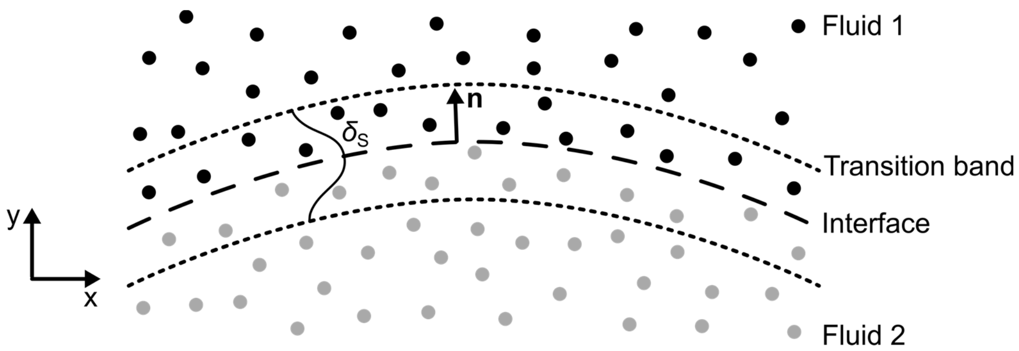

Figure 2.19: Illustration of a two-fluid situation with SPH particles of two different SPH phases, the surface delta function δ_S, and the unit normal vector $\mathbf{n}$ to the surface; adapted from ADAMI (2014, p. 15)

General remarks

When modeling physical problems involving fluids or transport phenomena, the Eulerian approach is the most common. Due to the necessity of using a mesh or grid, it is often challenging when dealing with fluid problems such as free surfaces, mobile interfaces, or topological changes. Generating a mesh or a grid at each numerical iteration leads to a time-consuming process. According to DUTRA FRAGA FILHO (2019, p. 2), the Lagrangian SPH method has several advantages when dealing with fluid dynamics and multi-phase flows:

- conservation of mass, which avoids undesirable numerical diffusion,
- free surface flows are treated naturally by the moving SPH particles, and
- there is no need for re-meshing at each numerical iteration.

Due to the high computational costs of the Lagrangian approach, the Eulerian approach was favored for a long time. The development progress of multi-core processors and parallelization methods in the last years enables the use of particle-based methods with several million SPH particles in the discretization domain. (DUTRA FRAGA FILHO 2019, p. 2)

3 State of the art

3.1 Chapter overview

Based on the fundamentals presented in Chapter 2, Chapter 3 describes the state of the art in the field of experimental and numerical investigations of the in-situ alloying process and its influence on hot cracking. Section 3.2 provides the literature on the experimental in-situ characterization of the melt pool. Section 3.3 discusses the publications and findings regarding the in-situ alloying during PBF-LB/M and related processes. Within this section, both experimental (Subsection 3.3.1) and numerical (Subsection 3.3.2) investigations of the melt pool are described. An overview of the relevant literature regarding hot cracking during PBF-LB/M and related processes is given in Section 3.4, with a focus on AAs in Subsection 3.4.1. This section is completed by a literature review of the topic modeling and numerical simulation of hot cracking during PBF-LB/M and related processes in Subsection 3.4.2. The state of the art is summarized in Section 3.5, and the need for action is presented.

3.2 Experimental in-situ characterization of the melt pool

The melt pool and its shape are associated with various properties of PBF-LB/M parts (MANI ET AL. 2015, SCIME & BEUTH 2019, CLIJSTERS ET AL. 2014). For example, a lengthened melt pool is associated with a high energy input and, thus, with a high temperature gradient along the building direction. Since the grain growth depends on the temperature gradient, the microstructure development within PBF-LB/M parts is also affected (ANTONYSAMY ET AL. 2013). The melt pool cross-section, typically measured by width and depth, can be correlated to the lack of fusion formation due to insufficient melt pool overlapping (QIU ET AL. 2019).

Machine learning or simulation models often use melt pool characteristics, such as the geometry or the thermal profile, as calibration and validation data (KHANZADEH ET AL. 2019, ZHANG ET AL. 2019, EGOROV ET AL. 2020).

To conclude, knowledge about the melt pool geometry and the temperature profile with high accuracy is of great interest within the scientific community. In particular, data obtained during the process is even more valuable for advanced calibration and validation of simulation models and for insights into the process to increase the process understanding.

X-ray imaging

Recently, high-speed X-ray imaging has been used intensively to investigate the melt pool dynamics in real-time during the PBF-LB/M process. X-ray imaging is sensitive to variations in the absorptivity of the investigated material. Therefore, the different phases that occur during the PBF-LB/M process, i.e., solid, liquid, and gas, can be distinguished from each other, allowing for the capture of the highly dynamic melt pool behavior.

ZHAO ET AL. (2017) presented an approach for in-situ monitoring of the PBF-LB/M process using high-speed X-ray imaging and diffraction. The samples studied in their experiments consisted of two carbon plates, a Ti-6Al-4V plate with a thickness of 450 µm and a height of 3 mm, and a Ti-6Al-4V powder layer of 100 µm in thickness. The Ti-6Al-4V plate and powder were located between the carbon plates. They demonstrated that several scientifically relevant phenomena in PBF-LB/M, such as phase transformation, solidification rate, and melt pool dynamics, can be analyzed with this setup. Following this work, numerous authors studied the complex melt pool dynamics using high-speed X-ray imaging: CALTA ET AL. (2018) found that the formation of keyhole pores along the melt track is due to vapor recoil forces, CUNNINGHAM ET AL. (2019) showed that there is a well-defined threshold from the conduction to the keyhole mode, KISS ET AL. (2019) observed a vapor bubble motion due to melt pool currents and a bubble splitting into clusters of smaller voids while the material rapidly cools down, LEUNG ET AL. (2018) uncovered mechanisms of pore migration by a Marangoni-driven flow, MARTIN ET AL. (2019b) investigated pore mitigation strategies based on laser power variations, PARAB ET AL. (2018) and PARAB ET AL. (2019) studied rapid oscillations of the keyhole and high-velocity rotating powder particles, BOBEL ET AL. (2019) demonstrated that the primary source of the pore formation originates from gas inclusions within the powder, and GUO ET AL. (2022) showed that powder agglomeration, keyhole oscillation, and melting-mode switching are the main mechanisms for causing melt flow instabilities.

GILLESPIE ET AL. (2021) used high-speed X-ray imaging in combination with immersion ultrasound to study the laser-generated stationary melt pool in a test bench without the presence of powder. Both signals were successfully synchronized to determine the melt pool depth. The time-of-flight and amplitude in the pulse-echo configuration were observed to have a linear relationship to the depth of the melt pool.

GOULD ET AL. (2021) combined high-speed infrared with high-speed X-ray imaging. While the high-speed X-ray setup enabled the observation of surface and subsurface phenomena, including vapor depression, porosity formation, powder and spatter ejection, and melt pool dynamics, the high-speed infrared imaging recorded the thermal information of the melt pool from the side and top-down orientation. They demonstrated that this technique is able to determine the three-dimensional melt pool geometry. The infrared detector had a pixel size of 30 µm, which could only be used to obtain qualitative information about the melt pool geometry. WANG ET AL. (2022a) used a similar approach to determine the melt pool dimensions in the conduction mode and in the keyhole mode. With a spatial resolution of 3.6 µm and a frame rate of 1,000 Hz, the melt pool was observed with high details by the infrared imaging system. The authors found correlations between the high-speed X-ray data and the high-speed infrared data. By this, they concluded that the high-speed infrared imaging could potentially give insights without the need of the high-speed X-ray imaging.

Infrared and visual (non-infrared) imaging

KRAUSS ET AL. (2012) investigated process errors originating from insufficient heat dissipation. For this, they captured thermal images of the process zone during PBF-LB/M with an uncooled microbolometer detector with a resolution of 640 x 480 pixels and a frame rate of 50 Hz. The detector was mounted outside the building chamber of a commercial PBF-LB/M machine at an angle of 45° to the building platform. With the used frame rate, the laser scanned two hatch lines within each frame, making locating and quantifying the melt pool impossible. However, an error detection was still possible. LANE ET AL. (2016) used a similar setup to the one in KRAUSS ET AL. (2012) and performed preliminary Finite Element (FE) simulations of the melt pool to design the camera and optics setup for capturing the melt pool region at a high magnification. They achieved a horizontal pixel size of 53.3 µm at 1,800 Hz. The setup could not fully capture the temperature evolution over time of the melt pool and the solidification region.

HEIGEL & LANE (2018) complemented their methodology by calibrating the temperature using the liquidus-solidus transition. A similar approach was performed a few years before for the laser cladding process by DOUBENSKAIA ET AL. (2013). The algorithm of HEIGEL & LANE (2018) located the discontinuity by identifying the minimum of the second spatial derivative of each pixel in the temperature profile. The pixel dimensions in the horizontal and vertical axes were 36 µm and 52 µm, respectively. With this, they were able to determine the melt pool length during the PBF-LB/M process. However, the quantitative measurements were only valid for very long melt pools due to the large pixel dimensions.

The methodology of HEIGEL & LANE (2018) was also applied by CHENG ET AL. (2018) to study the melt pool size of Inconel 718 during PBF-LB/M in dependence on the part height and the scanning speed. The authors used an Ytterbium laser source (wavelength 1060–1100 nm) and a LumaSense MCS640 near-infrared thermal imager. With a pixel size of 55 µm in the vertical direction and 47 µm in the horizontal direction, they determined the melt pool size to be 390 µm and 230 µm in length and width, respectively, for a scanning speed of 400 mm/s and a laser power of 180 W. A maximum of two pixels were detected within the phase transition, which means that the results are subject to a high degree of uncertainty.

ZHENG ET AL. (2019) implemented an infrared camera co-axially to the laser beam to extract the melt pool width using the phase transition method. Despite the pixel size of 53 µm, the comparison with single-tracks from the experiments showed a good agreement for the melt pool width. Furthermore, they showed that motion blur phenomena are insignificant due to the rapid cooling of the melt pool, which is an indication that there is a negligible information overlap between two subsequent infrared images.

SONG ET AL. (2017) used an off-axis visual imaging system to investigate different methods for the melt pool edge extraction. They compared the Otsu method, the fixed-threshold method, and the phase congruency method with a Log-Gabor filter to extract the melt pool edge. The Log-Gabor filter can simultaneously analyze the space and frequency characteristics of a signal. Due to the robustness of the phase congruency method against optical disturbances, such as blurred areas, spatters, or melt pool fluctuations, the authors attributed a high potential to the method for the in-situ process monitoring during the PBF-LB/M process.

LE ET AL. (2021) presented a low-cost off-axis visual imaging system based on a metal-oxide-semiconductor (CMOS) camera to inspect the melt pool during PBF-LB/M. A perspective transformation method was applied to transform the captured side-view image into a top-view image. The gray level intensity profile of the captured image was then analyzed regarding its discontinuity during the phase transition to determine the melt pool dimensions. The pixel size was approximated to 20 µm at a frame rate of 7,400 Hz. For the material Inconel 718, the obtained melt pool width deviated by 13 % and the melt pool length by 3 % compared to experimental results reported in the literature.

HOOPER (2018) developed a method that uses co-axial imaging with two high-speed cameras recording in the visible spectrum implemented in a commercial Renishaw AM250 PBF-LB/M machine. By using two band pass filters with different wavelengths, the authors were able to measure the real temperature with high precision, which was validated by a thermocouple. The temperature fields were captured at 100,000 Hz with a resolution of 20 µm per pixel. In addition to the geometry of the melt pool surface, the authors were able to correlate the exposure parameters (i.e., laser power and scanning speed) and the part geometry with thermal gradients and cooling rates of the melt pool. A similar method was used by VALLABH ET AL. (2022); however, the melt pool monitoring was performed with a co-axial imaging system consisting of only a single camera-based two-wavelength pyrometer. They correlated the measured temperature signatures of the surface of the melt pool with ex-situ determined melt pool depths, widths, and grain lengths. FURUMOTO ET AL. (2022) visualized the melt pool behavior during PBF-LB/M using a combination of high-speed visual imaging and two-color pyrometry. They showed that the temperature field of the melt pool was influenced by the morphological changes of the metal powder induced by physical and thermal interactions.

The approach from GOOSSENS & VAN HOOREWEDER (2021) combined data determined by in-situ co-axial visual imaging with melt pool data obtained by analytical modeling for fast virtual sensing of the melt pool depth. A comparison with metallographic investigations yielded an average relative error of the predicted melt pool depth for the full parameter set of 9.9 %.

3.3 In-situ alloying during PBF-LB/M and related processes

Several researchers have been investigating the in-situ alloying during PBF-LB/M and related processes. However, the majority concentrated on the resulting microstructure and less on the resulting melt pool dynamics and occurring phenomena in the process zone. The literature review described in the following provides a comprehensive study regarding experimental investigations of the process zone during the in-situ alloying as well as related modeling and numerical simulation approaches.

3.3.1 Experimental investigations of the process zone

KANG ET AL. (2017) studied the material Al12Si, whereby the authors mixed elemental powder instead of using a pre-alloyed one. The elemental powders were mixed using a tumbling mixer and processed via PBF-LB/M. They showed that the PBF-LB/M process parameters can manipulate the rate of Si solubility in Al. A coarser microstructure at an increased energy density was attributed to a nano-sized Si agglomeration and rejection of Si from Al due to a longer melt pool retention. The authors further investigated the macro-segregation of the primary Si phase during PBF-LB/M. The results indicated that the macro-segregation is significantly influenced by the size and temperature of the melt pool.

HANEMANN ET AL. (2019) blended AlSi10Mg powder with Si powder by using a shaker box. They showed a tailorability of the coefficient of thermal expansion (CTE) with the adjustment of the Si content during the PBF-LB/M process. A decrease in the CTE of 43 % compared to pure Al was achieved at an Si content of 50 wt.%.

The in-situ alloying of AlCu materials can be difficult due to the melting point difference between Al and Cu, which leads to an incomplete diffusion of Cu and, subsequently, to macro-segregation (WANG ET AL. 2018, BOSIO ET AL. 2022, SKELTON ET AL. 2022). In addition to composition gradients, microstructural gradients were also observed by the authors around the partially diffused Cu areas. This problem was tackled by MARTINEZ ET AL. (2019) with a pre-heated powder bed and by BARTKOWIAK ET AL. (2011) by blending the Al powder with microscopic Cu particles ($d_{50} = 3$ µm). Both studies achieved promising results without the occurrence of macro-segregations after the PBF-LB/M process.

WANG ET AL. (2022b) investigated the influence of powder mixtures containing Mo, Nb, Ti, and V on the melt pool properties during the laser-based DED process by using X-ray imaging. They found that the Ti powder melts the fastest during the in-situ alloying process, Ti and V powders melt near their initial location, and Mo and Nb powders melt when traveling with the melt flow. Furthermore, they found that a uniform distribution of the elements in the melt pool is supported by the melt flow.

3.3.2 Modeling and numerical simulation of the melt pool

Several researchers investigated the melt pool dynamics during PBF processes with simulation models (KÖRNER ET AL. 2011, KHAIRALLAH & ANDERSON 2014). WEIRATHER (2023) used the SPH method to simulate the PBF-LB/M process. The model included the physics of the surface tension, the Marangoni flow, the melting and solidification, the process gas, and the evaporation with resulting recoil pressure.

Although the above-mentioned numerical models considered a wide range of physical phenomena that occur during the process (e.g., melting, solidification, vaporization, surface tension, or convection), the effects of in-situ alloying or multi-material processing were considered only in a very limited way (WEI & LI 2021, MEHRPOUYA ET AL. 2022). The publications that have addressed this issue are presented in the following.

Mesh-based methods

DONG ET AL. (2021) used the FE method in the software *Comsol Multiphysics* to simulate a ball-milled Ti powder that was blended with elemental powders of Al and V. They considered phase changes, convection, and radiation. Simplifications were made concerning the powder bed, as it was assumed to be continuous. The influence of the flow of the alloy droplet on the temperature field was not considered, and the laser heat source was defined as a surface heat source. The mixing effects in the liquid phase of the blended materials were not considered.

CHEN ET AL. (2019) proposed a multi-layer three-dimensional FE model for multi-material products to study the effects of the PBF-LB/M process parameters on the thermal behavior of the interface between Ti6Al4V and TiB_2. The mixing of the two materials in the liquid phase was not modeled.

GAN ET AL. (2017) investigated the thermal behavior and the composition transport during the laser-based Directed Energy Deposition (DED) process by using the Arbitrary Lagrangian Eulerian (ALE) formulation. The three-dimensional numerical model was used to study the distribution of the elements Ni, Cr, and Fe during a multi-layer scenario. Simplifications of the model were done by a temperature- and composition-independent surface tension, and by neglecting thermal radiation, vaporization effects, and micro-segregations of solutes during the solidification process.

KÜNG ET AL. (2021) presented a two-dimensional Lattice-Boltzmann model to simulate the mixing of materials during the PBF-LB/M process. The model considered the effects of diffusion caused by the gradient of the chemical potential and included concentration-dependent material properties. The solidification was modeled by using an analytically described phase diagram of completely miscible components. The phenomena of diffusion and heat conduction were validated with data from analytical calculations. For the multi-material PBF-LB/M process, a partitioning of the melt pool into an inner well-mixed region surrounded by the melt of the lower-melting component was observed.

FLINT ET AL. (2020) presented a multi-component thermal fluid dynamics framework, based on the Volume of Fluid (VOF) method, that allows predicting the alloy system development due to melting, vaporization, condensation, and solidification. The framework was applied to the electron-beam welding process. SUN ET AL. (2020) used the VOF method to investigate a mixed Inconel 718/Cu10Sn powder bed in the PBF-LB/M process. The mixing behavior was simulated by solving the continuity equation for the volume fraction of the components. By doing that, the influence of the distinct thermo-physical properties of the two alloys on the melt pool characteristics was investigated.

TANG ET AL. (2022) extended the model of SUN ET AL. (2020) by, among others, adding a ray-tracing heat source. The results were compared to those of SUN ET AL. (2020) and showed a significantly different topological depression of the melt pool.

CHOUHAN ET AL. (2022) presented a model based on the Finite Volume Method (FVM) to investigate the mixing behavior of Al and Cu during a single-track PBF-LB/M process. The physics of melting, solidification, surface tension, recoil pressure, and diffusion-based mixing were considered in the model. The Discrete Element Method (DEM) was used to create the powder bed in the model. By introducing a mixing index, the authors were able to quantify the homogeneity of the molten material. They showed that the Marangoni convection and the recoil pressure control the distribution of Cu in the liquid Al and that the shape of the melt pool is substantially influenced by the mixing. A comparison of the melt pool depth and width between the simulation and the experiment yielded deviations of up to 17 % for the depth and up to 24 % for the width.

GU ET AL. (2020) used a similar modeling approach for the materials stainless steel (SS) 316L and Cu10Sn during the PBF-LB/M process, both separately and with an interface. It was found that the phase migration at the interface depends on the convective fluid flow inside the melt pool. The mixing of materials due to a concentration gradient and a validation of the melt pool geometry were not part of the publication.

Mesh-free methods

The mechanisms of actions of the in-situ alloying or the multi-material processing during PBF-LB/M have been subjected to only a few mesh-free method investigations.

SORKIN ET AL. (2017) investigated a multi-material process by means of molecular dynamics. The open-source Large-scale Atomic Molecular Massively Parallel Simulator (LAMMPS) was used to model the melting of the materials Fe and Al on a nanometer scale. Since most of the relevant physics during PBF-LB/M, including Marangoni convection, multi-phase flows, and recoil pressure, were neglected, the model did not reveal the complexity of the melt pool behavior.

RUSSELL ET AL. (2018) used the SPH method to model the melt pool as an isothermally incompressible viscous fluid using the Navier-Stokes equations. Their model included several phenomena, such as surface tension, Marangoni convection, volumetric laser absorption, convection, and radiation. The simulation model was validated with one micrograph from the experiment and showed a good agreement regarding the melt pool depth and melt pool width. They used the simulation model to trace the SPH particles during the liquid phase for a multi-material scenario. A scenario was created in which every third powder particle was given twice the thermal conductivity of its neighbors. Due to this increased thermal conductivity, the thermal energy generated by the laser was transported faster to the borders of the melt pool, which resulted in a faster melting and therefore in a widening and deepening of the melt pool. Simplifications of the simulation model were done by neglecting the deformation of the solid phase, by neglecting the process gas, by modeling only in two dimensions, and by neglecting the concentration-dependent diffusion during the multi-material mixing in the liquid phase.

3.4 Hot cracking during PBF-LB/M and related processes

Since this thesis analyses the influence of compositional variations, the literature review described in the following focuses on the hot cracking susceptibility and approaches to alter it by changing the alloy composition.

3.4.1 Aluminum-based alloys

Due to their high strength and low density, AAs, such as the 2000, 6000, and 7000 series, are highly demanded. However, the advantages of precipitation hardening also entail a larger solidification interval in the AAs, which may lead to hot cracking during the solidification of PBF-LB/M parts (SING ET AL. 2021).

For the congeneric laser beam welding process, the positive effect of additives on the hot cracking susceptibility has been intensively researched over the last decades. By feeding a filler wire into the leading edge of the melt pool, the additive is mixed with the base material in the liquid phase. Positive effects on the hot cracking susceptibility were observed for the 2000 series with 2319, 2014, or 4000 series filler wires; for the 5000 series with 5083, 5754, 4047, or 4043 filler wires; for the 6000 series with 4043 or 4047 filler wires; and for the 7000 series with 5183 or 5052 filler wires (ION 2000). Since the effect of additives on the hot cracking susceptibility during the laser beam welding process has already been extensively investigated, various scientific findings can be partially transferred to the comparatively new PBF-LB/M process.

MARTIN ET AL. (2017) introduced Zr nanoparticles to the AA 7075 and the AA 6061 to control the solidification during the PBF-LB/M process. The idea was to induce heterogeneous nucleation sites by forming Al_3Zr nucleation phases when Zr is melted with Al. The effect can be used to achieve equiaxial fine grains. Here, in-situ alloying is favorable since rapid grain coarsening can occur during the atomization process of pre-alloyed powders. For both AAs, the authors achieved crack-free samples. Crack-free samples were also obtained by adding Si to the AA 7075 (MONTERO-SISTIAGA ET AL. 2016). However, avoiding hot cracks due to the Si addition comes at the expense of a reduced ductility compared to the unmodified AA 7075. ZHANG ET AL. (2017) tackled the hot cracking phenomena of AlCuMg by the addition of Zr. They showed a significantly reduced hot cracking susceptibility by the grain refining effect. The addition of Zr led to a decrease in the elongation while the tensile strength and yield strength increased. RIENER ET AL. (2022) processed the AlMgSi1Zr alloy during the PBF-LB/M process, whereby 0.5 wt.% Zr and 0.5 wt.% Ti were added prior to the process via mechanical mixing. They observed a crack-free fully equiaxed structure and particles containing Zr and Ti, which acted as heterogeneous grain refiners by building a semi-coherent interface. Further studies on the grain refining effect by adjusting the chemical composition were conducted for the additives Si (LI ET AL. 2020, ZHOU ET AL. 2020b), Sc (SPIERINGS ET AL. 2017, MARTIN ET AL. 2017), Zr (LI ET AL. 2020, SPIERINGS ET AL. 2017, MERTENS ET AL. 2021), ZnO (DADBAKHSH ET AL. 2018), and TiB_2 (ZHOU ET AL. 2020b, MAIR ET AL. 2021).

HOLZER ET AL. (2016) discussed the influence of the energy input during the laser beam welding process of AA 7075 on the change of the element concentration and the resulting hot cracking susceptibility. The concentration of the elements in the cross-sections of different weld seams produced by varying scanning speeds was measured by Energy Dispersive X-ray Spectroscopy (EDS). The measurements showed a loss of the volatile elements Mg and Zn. Calculations of the thermo-physical data for each resulting alloy system, i.e., the alloy composition after the vaporization, indicated a decreasing solidification interval, where the solidus temperature increased and the liquid viscosity decreased. According to the authors, the changed properties presumably decreased the hot cracking susceptibility.

WARRINGTON & MCCARTNEY (1989) discussed the hot cracking phenomena of Al-Cu alloys as a function of the alloy composition during the direct chill casting process. At 6 wt.% Cu, they observed a cracking susceptibility that was highly influenced by the grain structure and type.

WU ET AL. (2022) investigated the hot cracking susceptibility of AAs during the PBF-LB/M process regarding the addition of Li. Correlations between the microstructure evolution and the hot cracking susceptibility (*HCS*) were established to reveal the mechanism behind the cracking. They found that the higher stability of the intergranular liquid film led to a higher *HCS* at the grain boundaries compared to the *HCS* within the grains.

HUBER (2014) used the Laser-induced Breakdown Spectroscopy (LIBS) to investigate the welding behavior of materials with low weldability. By analyzing the chemical composition of the metal vapor during the laser beam welding process, conclusions about the composition of the weld seam and defects were drawn. The capability of the methodology was demonstrated for the AA 6060, which is known to be prone to hot cracks. By using an additional filler wire, chemical elements were introduced into the melt pool and thus into the weld seam. The results show that an Mg content between 0.5 wt.% and 1.25 wt.% prevents the formation of hot cracks.

3.4.2 Modeling and numerical simulation

This subsection builds on the fundamentals of hot cracking presented in Section 2.4 and supplements them concerning the current state of the art. Most modeling approaches for the hot cracking phenomena were derived from the casting theory. They can be divided into three categories according to the cracking mechanism: based on the mechanical theory, based on the non-mechanical theory, and based on both the mechanical and the non-mechanical theory (ZHANG ET AL. 2021b).

Mechanical theory

The hot crack initiation starting from a thermo-mechanical stressing was formulated with the help of a strain-based model by PROKHOROV (1956) and PROKHOROV (1971) (as cited by LIPPOLD (2015)). Within this model, the brittle temperature range (BTR) was postulated as the range where hot cracking occurs when a critical strain is reached. A hot crack formation is initiated when the total strain $\varepsilon_{\text{total}}$, which is the sum of the internal strain ε_{int} and the external strain $\varepsilon_{\mathrm{ext}}$, is lower than the ductility (KANNENGIESSER & BOELLINGHAUS 2014, p. 398). The strain resulting from the volume change during the phase transition (liquid to solid) and the thermal strain are part of $\varepsilon_{\mathrm{int}}$, while $\varepsilon_{\mathrm{ext}}$ is due to external mechanical stressing. According to the theory, the critical strain rate $\mathrm{d}\varepsilon_{\mathrm{total}}/\mathrm{d}t$ and the critical thermal deformation $\mathrm{d}\varepsilon_{\mathrm{total}}/\mathrm{d}T$ can be written as (KANNENGIESSER & BOELLINGHAUS 2014, p. 398)

$$\frac{\mathrm{d}\varepsilon_{\mathrm{total}}}{\mathrm{d}T} = \frac{\mathrm{d}\varepsilon_{\mathrm{total}}}{\mathrm{d}t} \Big/ \frac{\mathrm{d}T}{\mathrm{d}t} \ . \tag{28}$$

Non-mechanical theory

The model of FEURER (1977) is based on a situation of competition: the volume shrinkage of the melt during the solidification (rate of shrinkage (*ROS*)) competes with its capability to fill free spaces between emerging dendrites (rate of feeding (*ROF*)). For a hot crack formation, the following condition must be fulfilled:

$$ROF < ROS \ , \tag{29}$$

with

$$ROF = \frac{f_{\mathrm{L}}^2 \lambda_2^2 p_{\mathrm{f}}}{24\pi b^3 \eta L^2} \tag{30}$$

and

$$ROS = \frac{(\rho_0 - \rho_{\mathrm{S}} + u_{\mathrm{cc}} w_{\mathrm{epc}} C_{\mathrm{L}}) \dot{T} f_{\mathrm{L}}^{(2-w_{\mathrm{epc}})}}{\rho_{\mathrm{av}} (1 - w_{\mathrm{epc}}) m_{\mathrm{L}} C_0} \ , \tag{31}$$

where f_{L} is the liquid fraction, λ_2 is the secondary dendrite spacing, b is the dendritic network tortuosity, η is the dynamic viscosity, p_{f} is the effective feeding pressure, L is the length of the porous network, ρ_0 is the liquid density at the melting point, ρ_{S} is the solid density, ρ_{av} is the average density between solid and liquid, u_{cc} is the composition coefficient, w_{epc} is the equilibrium partitioning coefficient, C_{L} is the composition of the liquid at the solid-liquid interface, $\dot{T}$ is the average cooling rate during solidification, m_{L} is the slope of the liquidus line, and C_0 is the alloy composition (CONIGLIO & CROSS 2013).

Smaller dendrites and the associated reduced feeding pressure of the melt are believed to enhance the *ROF*. Within the model, the influence of external mechanical stressing is neglected. According to KANNENGIESSER & BOELLINGHAUS (2014), the material-specific physical quantities for calculating the *ROF* and *ROS* are challenging to determine. By means of the *ROF*/*ROS* condition, WOLF ET AL. (2005) showed for Tungsten Inert Gas (TIG) welding that the curvature radius of the melt pool front significantly affects the formation of hot cracks. In particular, an increasing hot cracking susceptibility (*HCS*) was found for decreasing curvature radii.

CLYNE & DAVIES (1979) proposed a hot cracking criterion based on FEURER (1977) with the assumption that liquid metal cannot move freely during the final stage of solidification. Therefore, the strains that already accumulated are not influenced by the liquid metal. The *HCS* is defined as the ratio of the fragile time period t_f that may cause hot cracking to the available time t_a of the stress relief process, during which a high *ROF* occurs, and is given by

$$HCS_\mathrm{CD} = \frac{t_\mathrm{f}}{t_\mathrm{a}} = \frac{t_{0.99} - t_{0.90}}{t_{0.90} - t_{0.40}} \ , \tag{32}$$

where $t_{0.99}$ is the time when the solid fraction f_S is equal to 0.99, $t_{0.90}$ is the time when $f_\mathrm{S} = 0.90$, and $t_{0.40}$ is the time when $f_\mathrm{S} = 0.40$ (ZHANG ET AL. 2021b).

Mechanical and non-mechanical theory

The authors Rappaz, Drezet, and Gremaud proposed the RDG model (RAPPAZ ET AL. 1999), in which hot cracking is induced by a microvoid formation. The void is assumed to be formed due to a high strain rate generated by a thermal expansion perpendicular to the dendrite axes. A pressure drop close to the root of the dendrites is generated due to the resulting deformation. The molten phase then fills the created spaces. Because of premature solidification, a complete compensation might not be ensured, leading to micropores and, therefore, to hot cracking.

The RDG model is defined as

$$\dot{\varepsilon}_\mathrm{d,\,max} = \frac{|\nabla T|}{B(T)}\left(\frac{\lambda_2^2 |\nabla T| \Delta p_\mathrm{c}}{180(1+\beta)\eta} - \frac{v_\mathrm{iso}\beta H(T)}{1+\beta}\right), \tag{33}$$

with

$$B(T) = \int_{T_\mathrm{S}}^{T_\mathrm{L}} \frac{\int_{T_\mathrm{S}}^{T_\mathrm{L}} f_\mathrm{s}(T)\mathrm{d}T f_\mathrm{s}(T)^2}{(1-f_\mathrm{s}(T))^3}\mathrm{d}T \tag{34}$$

and

$$H(T) = \int_{T_\mathrm{S}}^{T_\mathrm{L}} \frac{f_\mathrm{s}(T)^2}{(1-f_\mathrm{s}(T))^2}\mathrm{d}T \ , \tag{35}$$

where $\dot{\varepsilon}_\mathrm{d,\,max}$ describes the maximum strain rate of the dendrites, T is the temperature, ∇T is the thermal gradient, λ_2 is the secondary dendrite spacing, Δp_c is the critical pressure drop, β is the shrinkage factor, v_iso is the isothermal velocity, η is the dynamic viscosity, T_S is the solidus temperature, and T_L is the liquidus temperature.

The main outcome of the RDG model is the *HCS*, given by

$$HCS_{\mathrm{RDG}} \sim \frac{1}{\dot{\varepsilon}_{\mathrm{d,\,max}}} \ . \tag{36}$$

Further model extensions and experimental findings were reported by several authors: WANG ET AL. (2004) found that, in alloys with a high *HCS*, solidification cracks may be avoided when the grain boundary angle is below a critical value, WOLF ET AL. (2005) showed that the location of solidification cracks can be correlated with the position-dependent strain rates along the solidification front and with the position-dependent curvature of the melt pool, ZHOU ET AL. (2020a) demonstrated that the *HCS* results of the RDG model are consistent with experimental findings for the 7065 alloy, and SONAWANE ET AL. (2021) used the RDG model together with simulations based on ROSENTHAL (1946) to analyze the *HCS* for the AA 6061 during the PBF-LB/M process. They found that stable liquid films correlate with grain boundary misorientations. According to the authors, these misorientations cause a sudden increase in the pressure drop, which leads to hot cracking.

KOU (2015b) developed a criterion for the hot crack formation, which was concretized and applied to various materials by KOU (2015a). Within this cracking model, the separation of grains from each other is caused by tensile deformation and the growth in the lateral direction towards each other is caused by solidification processes. The model also considers the liquid feeding between the grains, which is caused by a volume reduction of the material during the transition from the liquid state to the solid state. The change in volume leads to a suction effect that forces the liquid to fill the space created. The criterion characterizing the *HCS* was introduced as the maximum steepness of the curve in a $T - f_{\mathrm{S}}^{1/2}$ diagram up to a certain threshold. Blending the powder with additives alters the solidification path, leading to a variation in the *HCS*. The Kou criterion for the *HCS* is defined as

$$HCS_{\mathrm{Kou}} \sim \max\left(\left|\frac{\mathrm{d}T}{\mathrm{d}f_S^{\frac{1}{2}}}\right|\right) . \tag{37}$$

The Kou model was used by several authors to investigate the *HCS*. For example, LIU ET AL. (2017) investigated the solidification interval for the 5086 alloy in the arc welding process and used the Kou model for an interpretation. An experimental setup was introduced that was able to quench the mushy zone with molten Wood's metal. They found that a large amount of Mg back-diffusion occurred from quenching the mushy zone during solidification. The calculated $T - f_{\mathrm{S}}^{1/2}$ curves showed that the maximum of $\left|\mathrm{d}T/\mathrm{d}f_{\mathrm{S}}^{1/2}\right|$ was reduced significantly by the back-diffusion of Mg. The composition-dependent hot cracking susceptibility of Al-Si alloys was analyzed by HYER ET AL. (2021) for the PBF-LB/M process. They calculated the hot cracking susceptibility by using the Scheil-Gulliver solidification modeling with the relationship $\left|\mathrm{d}T/\mathrm{d}f_{\mathrm{S}}^{1/2}\right|$, similarly to LIU ET AL. (2017), and validated the calculations by comparing them to experimentally determined data of six binary Al-Si alloys with varying Si content. The experiment showed a significant number of hot cracks for the alloys containing

1 wt.% and 2 wt.% Si. The results agreed with the calculated high magnitudes of $\left|\mathrm{d}T/\mathrm{d}f_\mathrm{S}^{1/2}\right|$ for the respective alloys. SHAONING ET AL. (2018) used a two-dimensional phase field simulation to determine the $T - f_\mathrm{S}^{1/2}$ curve, which is required as input into the Kou model, to investigate the *HCS* of Al-Mg and Al-Cu alloys during welding.

CHEN ET AL. (2021) evaluated the RDG and the Kou model regarding the *HCS* for Al-Li alloys. They used a two-dimensional phase field model to predict the solidification microstructure of the investigated alloy. In addition, a Computational Fluid Dynamics (CFD) simulation was performed based on the geometries from the simulated microstructure features to predict the inter-dendritic pressure distribution. The simulation results were compared with predictions of the RDG and the Kou model. It was found that the feeding pressure drop varies as a function of the grain orientation, which is in contrast to the RDG model, where this parameter is assumed to be constant. The Kou model was found to be insufficient to calculate materials for which a transition from columnar to equiaxed grains occurs because the values of $\left|\mathrm{d}T/\mathrm{d}f_\mathrm{S}^{1/2}\right|$ near $f_\mathrm{S} = 1$ are the same for both states.

3.5 Conclusions and need for action

Section 3.2 provided a comprehensive overview of experimental techniques to characterize the melt pool during the process. Numerous publications have been issued in this area of research in the last few years. In particular, techniques using high-speed X-ray imaging, IR imaging, or visual imaging with multiple cameras and bandpass filters have shown great potential in capturing the melt pool dynamics. Although the X-ray offers insights into the process with high temporal and spatial resolution, it can only be applied to experimental setups on a laboratory scale. The transferability to commercial PBF-LB/M machines has not yet been sufficiently demonstrated. In addition, temperature measurements are not possible, which is a major disadvantage, since the PBF-LB/M process is mainly driven by thermal effects.

In contrast, IR or visual imaging systems with bandpass filters offer alternatives that can be integrated into existing commercial PBF-LB/M systems with reasonable effort. However, the high temporal and spatial resolution required to capture the melt pool in detail, both geometrically and in terms of the temperature, poses significant challenges for both systems. Publications that report on test setups that are close to commercial systems are rare and only partially meet the requirements from above. The determined dimensions of the melt pool geometry often have significant uncertainties because either the pixel dimensions are too large for the melt pool or the in-situ determined data have been insufficiently validated with alternative measurement methods.

Section 3.3 covered the method of in-situ alloying, which was discussed for PBF-LB/M and related processes. It can be stated that the in-situ alloying with its impact on the microstructure and the mechanical properties was studied intensively over the last years. Regarding the effect of additives on the melt pool properties, however, only a few studies for both experiment and simulation exist. The physical mechanisms in and around the melt pool, including the melt flow and the solidification behavior, determine the chemical homogeneity during the in-situ alloying process. Therefore, a fundamental understanding of these relationships is crucial, especially for the emerging microstructure and defect formation.

It is not yet clear up to which diameter an additive is melted sufficiently to still be suitable for a homogeneous mixing in the liquid phase. In addition, the influence of additives on the physical properties of the melt pool, such as the temperature field or the surface tension, has not been sufficiently investigated. Especially, experimental in-situ data of the melt pool dynamics or the temperature field, including the influence of additives, are rare. Concerning the mixing behavior of a multi-material situation, only limited knowledge exists. A few authors have recently addressed the extent to which the mixing of two powder materials takes place by diffusion, convection, or other physically-based mechanisms, but the results are partially contradictory. So further studies are required.

The reliability of numerical models highly depends on the quality and quantity of experimentally determined calibration and validation data of the in-situ alloying process. Due to the lack of physically-based simulation tools that are capable of modeling the melt pool during the in-situ alloying and which have been validated with comprehensive experimental data, the significance of the above-presented findings must be viewed critically and further substantiated.

Section 3.4 provided a comprehensive review of literature dealing with hot cracking in AAs and the modeling of the hot cracking mechanisms. Several studies have shown that changing the chemical composition via in-situ alloying could significantly reduce or even completely prevent hot cracking in AAs during the PBF-LB/M process. Although hot cracking has been studied for several decades for related processes such as welding, the PBF-LB/M-specific process characteristics restrict the transferability of several findings. As the most promising hot cracking models depend on the temperature field within the mushy zone, i.e., the thermal gradient, the *HCS* may be significantly influenced by process inherent dynamics. The majority of the presented publications, however, focused on the grain refining effect of the in-situ alloying to reduce the *HCS*. Quantitative findings on the effect of additives on the thermal gradient in the mushy zone are rare. Regarding the application of the RDG and the Kou model for the PBF-LB/M process, initial limited progress has been made.

The conclusions on the research fields presented above form the basis for the research deficit described below. It is noteworthy that the following statements refer to the state of the art at the respective time of the publications according to Chapter 5 of this dissertation.

- Since the defects generated during the PBF-LB/M process, i.e., lack of fusion defects and pores, highly depend on the melt pool dynamics, additives may have a stabilizing effect. Experimental data that quantifies the influence of additives on the melt pool properties during the PBF-LB/M process was not available prior to this work.
  Previous experimental setups are either pure test benches with a challenging transferability to commercial PBF-LB/M machines or lack temporal or spatial resolution. The lacking of a validated experimental methodology, including an experimental setup that is comparable to commercial PBF-LB/M machines and is

capable of quantifying the melt pool characteristics with a high spatial and temporal resolution, is a research deficit. In particular, the in-situ characteristics, i.e., the melt pool length and the temperature field, will give new insights into the process dynamics and will lead to more comprehensive validations of simulation models.

- Regarding the process understanding of the in-situ alloying, particularly within the melt pool, only limited information about the process underlying physics is available. A physically-based, validated, three-dimensional PBF-LB/M process model that can handle a multi-phase and multi-material situation is not known to date.
- There is a research deficit for predicting the *HCS* of PBF-LB/M parts with physically-based process models. Simulation tools that are capable of in-situ alloying and predicting its influence on the *HCS* were previously unknown. Current research activities focus on analytical modeling of the melt pool temperature field with the Rosenthal equation or using phase-field modeling. Since the temperature field in the mushy zone depends on the phenomena that happen prior to that point in time, a comprehensive modeling of the process as a whole, i.e., from the laser-material interaction until the full solidification of the melt pool, might be essential for the predictive capabilities of the current state of the art hot cracking models.

The research gaps described above provide the basis for the research approach presented in the following chapter.

4 Research approach

4.1 Chapter overview

This chapter outlines the research approach of this thesis, which led to the publications presented in Chapter 5. The basis of this chapter is given by the state of the art, and, in particular, by the need for action, described in Chapter 3. The scientific objectives (SOs) to address this need are described in Section 4.2. The methodological approach to achieve these SOs is explained in Section 4.3, followed by an overview of the five publications embedded in this thesis in Section 4.4.

4.2 Scientific objectives

To date, the methodologies for designing new alloys for the PBF-LB/M process intended to minimize the formation of defects usually require high experimental efforts. Although the in-situ alloying method offers a promising and faster approach to evaluate new alloy compositions than the atomization method, it requires a high experimental effort to analyze the quality of a powder mixture, e.g., the mixing behavior or the influence on minimizing defects. The investigation of defects is usually performed by a time-consuming part building, micro sectioning, and microscopic imaging. In addition, there are significant gaps in the fundamental understanding of the mechanisms of action occurring during the in-situ alloying process.

The global objective of this thesis is to improve the in-situ alloying process by creating a methodology capable of investigating any material combination regarding its processability, its influence on the melt pool dynamics, and its susceptibility to defects. Three SOs can be derived from the global objective and characterize the need for action prior to this thesis (cf. Section 3.5):

SO1 The influence of additives on the characteristics of the melt pool needs to be quantified. For this reason, a method has to be developed that is capable of determining the melt pool geometry and the temperature field of the process zone with a high temporal and spatial resolution. Therefore, a suitable measurement concept had to be selected, installed, and calibrated. The system should provide similar conditions for the process as a commercial PBF-LB/M machine and be suitable for investigating several powder mixtures. In addition, an algorithm had to be developed to determine the melt pool geometry automatically. To demonstrate the capability of the methodology, a well-known and processable alloy and a suitable additive needed to be selected. Both should differ significantly in their physical properties, e.g., surface tension, in order to achieve a measurable change in the melt pool characteristics.

SO2 A holistic approach is required to model the relevant mechanisms of action within the melt pool during the in-situ alloying. The specific models had to be calibrated and verified with appropriate scenarios. Usually, PBF-LB/M simulation models are validated with data obtained from ex-situ measurements, e.g., cross-sections. However, these do not exhibit the dynamics prevailing during the process. To validate the global simulation model, reliable experimental data are necessary that are determined in in-situ mode for the best possible comparison of simulation and experiment. With the validated simulation model, the mixing behavior of a multi-material scenario and the relevant physical mechanisms should be investigated.

SO3 Since the in-situ alloying method is one of the most effective methods to prevent parts from hot cracking, a predictive simulative framework needed to be developed. Appropriate hot cracking models that account for a change in the chemical composition were to be analyzed and selected. Combining a physically-based numerical process model with a hot cracking model is novel for the PBF-LB/M process and must therefore be evaluated regarding its prediction capabilities. For this reason, a research-relevant alloy with a high susceptibility to hot cracking during the PBF-LB/M process had to be chosen, as well as an additive that alters the physical properties of the melt pool significantly. Experimental data should assess the validity of the numerical framework.

4.3 Methodological approach

This section presents the methodological approach (see Figure 4.1) that was applied in this thesis based on the SOs formulated in Section 4.2. The approach pursued in this dissertation consists of three stages, of which the results and unique findings are documented in five publications (P), referred to as P1 to P5.

Stage 1: Methodology for an experimental in-situ characterization of the melt pool

The goal in this stage was to achieve SO1. Since the use of high-speed thermography and the calibration of the liquid-solid phase transition has proven to be suitable for characterizing the melt pool during the PBF-LB/M process (cf. Section 3.2), both methods were applied in this dissertation to characterize the melt pool. Preliminary studies were performed on a commercial PBF-LB/M machine to investigate the influence of additives on the temperature profile and the mixing behavior of the melt pool (P1). An experimental method with an increased optical resolution was developed to determine the liquid-solid phase transition with high precision. Subsequently, an algorithm was set up for a reproducible and automated evaluation of the temperature profile to calculate the melt pool dimensions (P2). The elaborated methods were merged in a novel experimental test bench that is capable of analyzing the melt pool with high temporal and spatial resolution, that is suitable for utilizing different powder blends, and that creates similar conditions as commercial PBF-LB/M machines.

The overall methodology was applied to determine the melt pool depth and melt pool length during the processing of several powder blends (P3).

Stage 2: Numerical modeling of the melt pool during the in-situ alloying process

In this stage, SO2 was addressed. The SPH method was chosen for the numerical modeling of the melt pool during the in-situ alloying process. The decisive factors for the decision were that a multi-phase flow formulation exists (cf. Section 2.5.2), that free surfaces are represented in a natural appearance (cf. Section 2.5.1), and that the method has already been proven to model the basic mechanisms of action of the PBF-LB/M process very accurately (WEIRATHER ET AL. 2019, WEIRATHER 2023). To account for the in-situ alloying process, the numerical model of WEIRATHER (2023) was extended to handle multi-materials and their physical properties. In addition, the mixing of multi-materials within the liquid phase was modeled by implementing a concentration-dependent diffusion, which distributes the weighted physical properties of the respective material according to the locally prevailing concentration. This stage is complemented by a verification and a validation of the model with in-situ data determined with the methodology of stage 1. The results of stage 2 were published in P4.

Stage 3: Numerical modeling of hot cracking by means of SPH

This stage aimed at achieving SO3. The RDG model and the Kou model were selected, since both account for a change in the chemical composition. A numerical framework was set up in which the validated multi-material SPH simulation of stage 2 was combined with the RDG model. The powder blends were simulated during the PBF-LB/M process until the solidification, and the thermal gradient served as an input for the RDG model at each time step. The predicted *HCS* of both models was compared with experimental data that was determined by means of the experimental setup of stage 1. For the materials, the research-relevant AA 7075 was chosen as the base powder due to its high *HCS* during the PBF-LB/M process, and Si was chosen as an additive. The type of the crack was analyzed, and the meaningfulness of the hot cracking models was discussed. The results of this stage were published in P5.

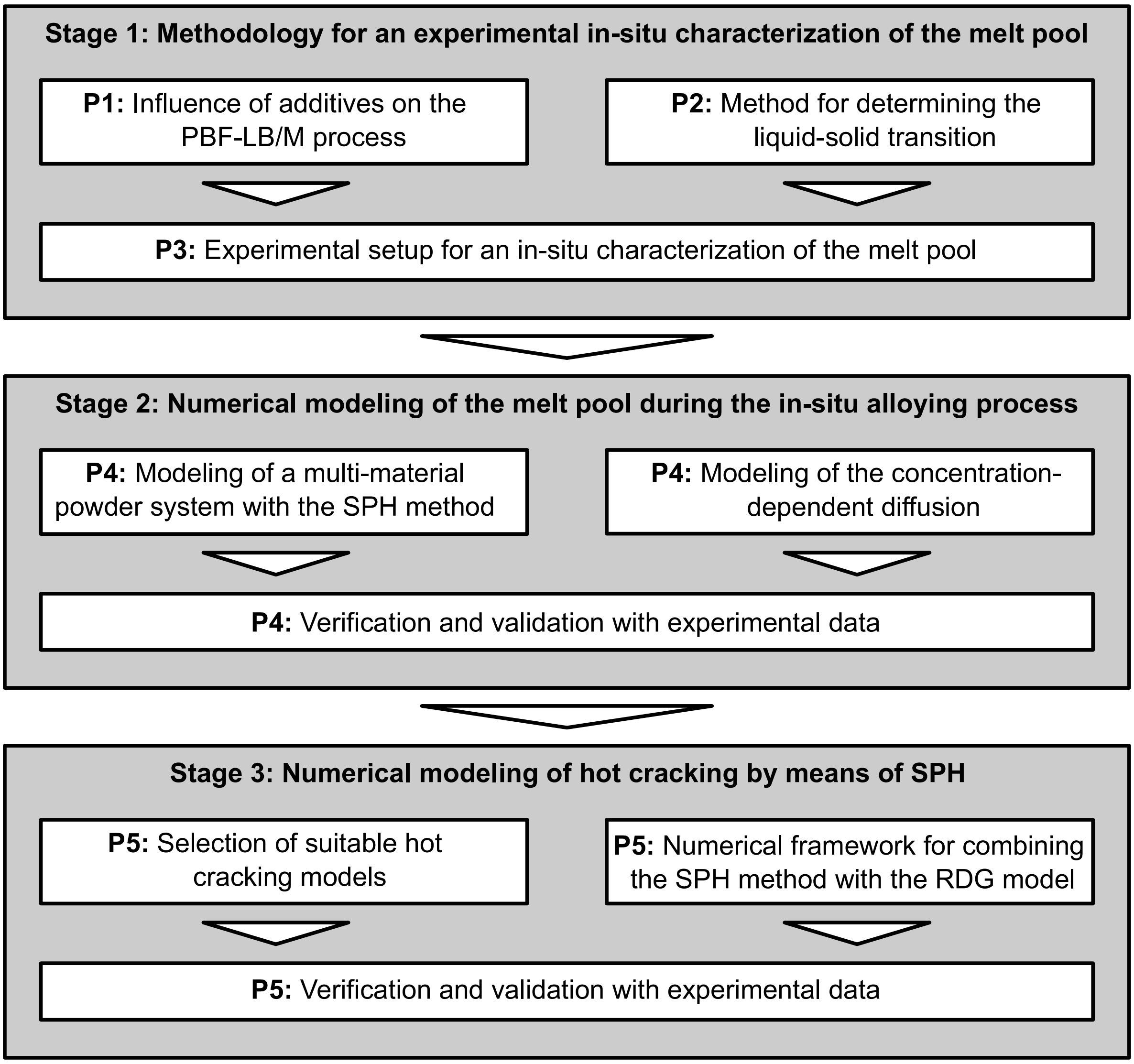

Figure 4.1: Methodological approach, sequentially arranged steps to achieve the SOs described in Section 4.2, and thematic focus of the publications P1 to P5

4.4 Overview of the embedded publications

An overview of the publications P1 to P5 including the authors, the titles, and the publication media is given in Figure 4.2. The core research findings of each publication are presented in more detail in Section 5.2. A list of the supervised student research projects can be found in Appendix A, while the publications embedded in this thesis are attached in Appendix B.

Stage 1: Methodology for an experimental in-situ characterization of the melt pool

Journal of Laser Applications

Title: Investigations on the influence of adapted metal-based alloys on the process of laser beam melting

Authors: Andreas Wimmer, Cara G. Kolb, Mariam Assi, Julien Favre, Andreas Bachmann, Anna Fraczkiewicz, and Michael F. Zaeh

P1

11th CIRP Conference on Photonic Technologies

Title: Analysis of the phase transformation of AlSi10Mg during laser powder bed fusion

Authors: Andreas Wimmer, Maja Lehmann, Adrian Schuler, and Michael F. Zaeh

P2

Progress in Additive Manufacturing

Title: In situ alloying: investigation of the melt pool stability during powder bed fusion of metals using a laser beam in a novel experimental set-up

Authors: Andreas Wimmer, Fabian Hofstaetter, Constantin Jugert, Katrin Wudy, and Michael F. Zaeh

P3

Stage 2: Numerical modeling of the melt pool during the in-situ alloying process

Metals

Title: Experimental and numerical investigations of in-situ alloying during powder bed fusion of metals using a laser beam

Authors: Andreas Wimmer, Baturay Yalvac, Christopher Zoeller, Fabian Hofstaetter, Stefan Adami, Nikolaus A. Adams, and Michael F. Zaeh

P4

Stage 3: Numerical modeling of hot cracking by means of SPH

Progress in Additive Manufacturing

Title: Experimental and numerical investigations of the hot cracking susceptibility during the powder bed fusion of AA 7075 using a laser beam

Authors: Andreas Wimmer, Hannes Panzer, Christopher Zoeller, Stefan Adami, Nikolaus A. Adams, and Michael F. Zaeh

P5

Figure 4.2: Overview of the publications contributing to the three stages of the methodology described in Section 4.3

In all five publications, the author of this dissertation was also the main author. Cara G. Kolb, Maja Lehmann, and Hannes Panzer are or were research associates at the Institute for Machine Tools and Industrial Management (*iwb*) at the Technical University of Munich (TUM). They contributed to brainstorming, experimental work, programming activities, and editing. Dr.-Ing. Andreas Bachmann was head of the Department for Additive Manufacturing at the *iwb* and contributed to brainstorming and editing. Mariam Assi, Prof. Dr. Julien Favre, and Prof. Dr. Anna Fraczkiewicz are researchers of the Department for Materials Science and Mechanical Engineering at the Institut Mines-Télécom (IMT), France, and contributed to brainstorming, microstructure analysis, and editing. Christopher Zoeller, Dr.-Ing. Stefan Adami, and Prof. Dr.-Ing. Nikolaus A. Adams are researchers at the Chair of Aerodynamics and Fluid Mechanics at the TUM. They contributed to brainstorming, programming activities, and editing. Adrian Schuler, Baturay Yalvac, Fabian Hofstaetter, and Constantin Jugert were university students who supported the experimental work and programming activities. Prof. Dr.-Ing. Katrin Wudy holds the Professorship for Laser-based Additive Manufacturing at the TUM and supported the work by brainstorming and editing. Prof. Dr.-Ing. Michael F. Zaeh is head of the *iwb* and supervisor of this work. His support has included review and editing of the publications, provision of resources, and funding acquisition as well as supervision. A more detailed description of the individual contributions of the main author to the five publications embedded in this dissertation is provided in Section 5.2.

5 Research findings

5.1 Chapter overview

In this chapter, the research results are presented that were obtained following the methodological approach according to Section 4.3. The findings are described in the form of short recapitulations of the publications P1 to P5. In addition, the respective contributions of the authors are briefly explained for each publication. A final discussion and evaluation of the results with respect to the scientific objects defined in Section 4.2 and to the state of the art (cf. Chapter 3) is provided in Section 5.3. Please note that the findings of the respective publications refer to the state of the art at that time.

5.2 Recapitulation of the embedded publications

5.2.1 Publication 1: *Influence of powder additives on physical properties of the melt pool and the microstructure* according to WIMMER ET AL. (2020a)

In publication P1, a comprehensive investigation of the influence of a powder additive on melt pool properties and the microstructure was performed. As powder materials, SS 316L was chosen as the base powder, and the AA AlSi10Mg as the additive. Both powders were selected due to their well-known processability during the PBF-LB/M process and their availability as commercial powders. From the addition of AlSi10Mg, significant effects were expected on the three topics described in the following.

- Stability of the melt pool: In the liquid state, Al has a surface tension that is half that of steel. A reduced Marangoni convection was assumed, which was expected to stabilize the melt pool.
- Thermal behavior of the powder bed and of the part: Due to the different physical properties, a decrease of the average thermal conductivity was expected.
- Phase stability and microstructure: Al is known for promoting the body-centered cubic (BCC) phase. It was expected that the addition of Al would affect the stability of the face-centered cubic (FCC) phase, and it would result in two-phased duplex structures with an increasing fraction of the BCC phase.

Prior to the experimental investigations, the powder compositions with a varying proportion of additives (0 wt.%, 1 wt.%, and 5 wt.%) were prepared by using a double-rotating cylindrical vessel. SEM analyses of the powder blends confirmed that the utilized mixing method was suitable for preparing powder compositions, as the heat input did not lead to any sintering, and the powder was homogeneously mixed.

The powder blends were then processed with a commercial PBF-LB/M machine, and the temperature field around the molten track during the PBF-LB/M process was determined using high-speed thermographic imaging with a door inlet in a way similar to the one in KRAUSS ET AL. (2012). The data showed that the higher the amount of AlSi10Mg is, the higher the temperature was that persisted along the single track (see Figure 5.1 (a)).

To describe this observation mathematically, a two-dimensional Rosenthal model was calibrated with the data from the experiment. However, the Rosenthal model was not able to predict the thermal field of the experiment in every section. As a reason for that, it was stated that the latent heat of the solidification and the specific thermal properties of a powder bed, i.e., the low thermal conductivity acting as an insulator, are neglected in the Rosenthal model.

A microstructure analysis demonstrated that a higher concentration of AlSi10Mg increased the formation of the BCC phase. The solidification proceeded with the BCC phase only, and Al was homogeneously included in this phase. To investigate the mixing behavior of the powder blends, chemical variations were revealed by Backscattered Electron Imaging (BSE) and subsequent Energy Dispersive X-ray (EDX) mapping. The blend containing 1 wt.% of AlSi10Mg showed no heterogeneities for the main elements (Fe, Cr, Ni, and Mo), but a variation of the Al concentration was detected at the bottom of the solidified melt pool (see Figure 5.1 (b)). By using Scheil-Gulliver simulations (GULLIVER 1915), which describe the solute redistribution during the solidification of an alloy, the observation was explained by the formation of the BCC phase that starts at the bottom of the melt pool leading to a higher concentration of Al in this region. Specimens containing 5 wt.% of AlSi10Mg exhibited a higher number of cracks than pure SS 316L powder. This indicates that the change of the solidification path severely increases the emergence of thermal distortions and residual stresses, resulting in the cracking of the material during solidification.

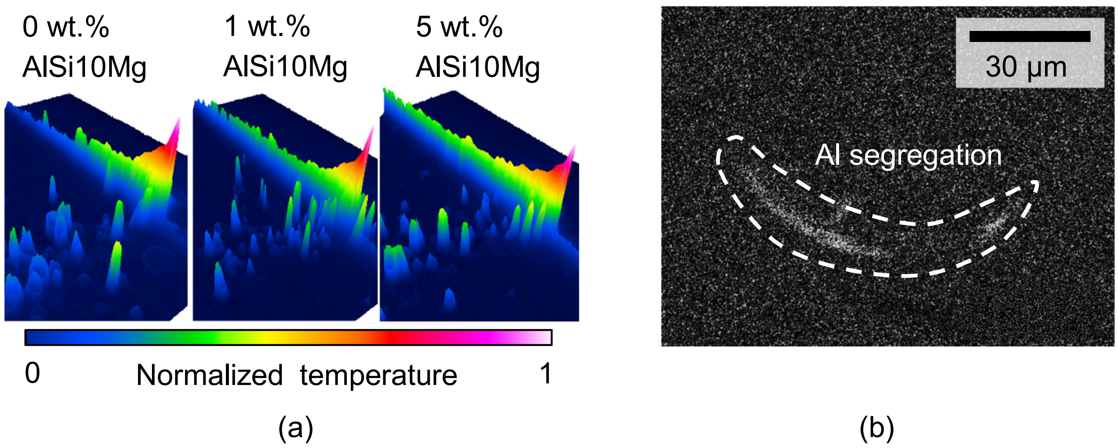

Figure 5.1: (a): Three-dimensional thermographic illustration of a scan track for pure SS 316L and for blends containing AlSi10Mg; (b): EDX mapping of Al for a sample produced from SS 316L containing 1 wt.% AlSi10Mg

Main findings

The conclusions and research findings (RFs) presented in WIMMER ET AL. (2020a) were as follows:

RF1: A rotatory cylindrical container is suitable for preparing a homogeneous powder blend without pre-sintering the particles.

RF2: High-speed thermographic imaging is capable of observing the influence of additives on the thermal field of the melt pool. Smaller temperature gradients were observed with higher amounts of Al.

RF3: The analytical Rosenthal model is only partially suitable for describing the in-situ alloying process.

RF4: The composition containing 1 wt.% of AlSi10Mg showed a segregation of Al within the melt pool.

Contributions of the authors

Andreas Wimmer, the author of this thesis, developed the idea to investigate the influence of additives on melt pool properties. He planned and performed the manufacturing of the samples and the thermographic experiments, evaluated the measurement data, and conducted the analytical modeling. Cara G. Kolb contributed significantly to the structure and the overall methodology of this publication. She was also responsible for the powder preparations and investigations. Mariam Assi and Julien Favre elaborated on the Scheil-Gulliver simulations and the microstructure analysis. The manuscript was written by Andreas Wimmer, Cara G. Kolb, and Julien Favre, and edited by Andreas Bachmann, Mariam Assi, Anna Fraczkiewicz, and Michael F. Zaeh. All authors discussed and commented on the findings.

5.2.2 Publication 2: *Methodology for determining the liquid-solid phase transition by means of high-speed infrared imaging* according to WIMMER ET AL. (2020b)

The results of P1 showed that additives have a significant influence on the melt pool characteristics. For a more quantitative analysis of the melt pool, particularly the melt pool dimensions that form during the process and are associated with the melt pool dynamics, a method was developed in P2 to determine the phase transition with high detail. By that, the spatial location at which the material solidifies can be determined without knowing the exact emission coefficient. This paved the way to quantify the influence of additives on the melt pool dynamics in P3.

Similarly to P1, a commercial PBF-LB/M machine was modified for an off-axis observation of the process zone. The high-speed camera was equipped with a 100 mm focal length optics and 63.5 mm extension rings with a simultaneous adjustment of the focal length for a high spatial resolution. A frame rate of 9,762 Hz was chosen to allow for a high temporal resolution.

One of the main advantages of high-speed in-situ measurements is the reduction of several disturbance variables, the influence of which may be found in microsections, e.g., the variation of the laser spot size, the process gas flow, the heat distribution of the building platform, or the layer thickness. The spatial calibration for the horizontal and the vertical axis was performed on the building platform inside the process chamber with the help of a glass scale. A pixel width of 16.7 µm and a height of 25.0 µm were determined.

A data analysis algorithm was developed to handle the high number of recorded frames and reproducibly analyze the phase transition. In the first step, rotational and shifting operations were performed to extract the temperature profile of a single pixel line. In the second step, the single pixel lines were evaluated by identifying the phase transition at the solidus temperature. Similarly to the method of HEIGEL & LANE (2018), the first minimum of the second spatial derivative that occurs during the cooling process of the melt pool was used as an indicator (see Figure 5.2 (a)).

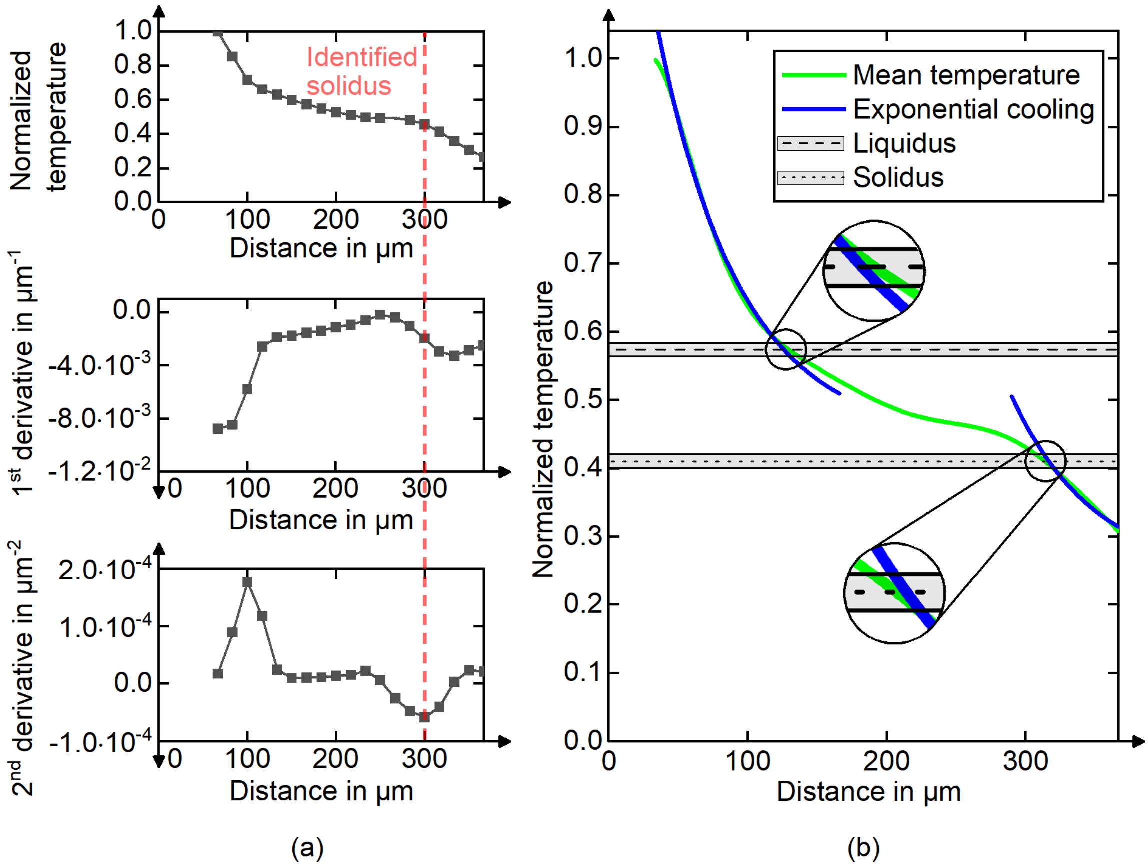

Figure 5.2: (a): Identification of the solidus of an example single pixel line by means of the first minimum of the second spatial derivative; (b): mean temperature profile with fitted exponential cooling; the points at which the exponential cooling model deviates from the mean temperature (magnifications), were assigned to the liquidus and solidus temperature, respectively.

The frames with an identified phase transition were further used in the data processing algorithm. To determine the solidus and liquidus temperatures more reliably, the average of 364 images was determined. Since the effect of cooling in the liquid and the solid phase can be described with physical models depending on an exponential decay, the mean temperature was fitted with an exponential decay function in the liquid and solid sections, respectively. The points where the exponential functions deviate from the mean temperature were assigned to the liquidus and solidus temperatures (see Figure 5.2 (b)).

With the help of this method, the phase transition of AlSi10Mg was investigated, and the difference between the solidus and the liquidus temperature, i.e., the ΔT, was determined. The analysis showed that an increasing energy input leads to a decreasing ΔT. Therefore, a low energy input results in a higher undercooling during the non-equilibrium solidification process.

Main findings

The conclusions and RFs presented in WIMMER ET AL. (2020b) were as follows:

RF1: The experimental setup enabled pixel sizes that were half of those compared to the state of the art and allowed for a detailed investigation of the phase transition.

RF2: A novel data analysis method was developed that is capable of determining the difference between the liquidus and the solidus temperature.

RF3: The methodology allowed for investigating the undercooling of AlSi10Mg processed with PBF-LB/M. A clear tendency of a decreasing ΔT with an increasing energy input was observed.

Contributions of the authors

Andreas Wimmer was the main author of the published conference article and developed the idea for the methodology. He planned, coordinated, and executed the experiments. Adrian Schuler supported the experiment execution and the programming activities within the framework of his master thesis. Maja Lehmann supported the discussion of the findings, particularly material scientific aspects such as the undercooling behavior. The manuscript was written by Andreas Wimmer and Maja Lehmann, and edited by Michael F. Zaeh. All authors discussed and commented on the findings. Andreas Wimmer presented the results in a talk at the 11th CIRP Conference on Photonic Technologies (LANE) in Erlangen, Germany, in 2020.

5.2.3 Publication 3: *Methodology for characterizing the melt pool during the in-situ alloying process* according to WIMMER ET AL. (2022)

P1 and P2 showed that additives can alter the melt pool characteristics, and the methods developed within these publications are suitable to quantify these observations. However, the methods were not capable of measuring the melt pool depth in in-situ mode, which is a key characteristic for emerging defects (cf. Subsection 2.2.3). Since commercial PBF-LB/M machines allow only limited access for process monitoring, a custom PBF-LB/M test bench was built (see Figure 5.3).

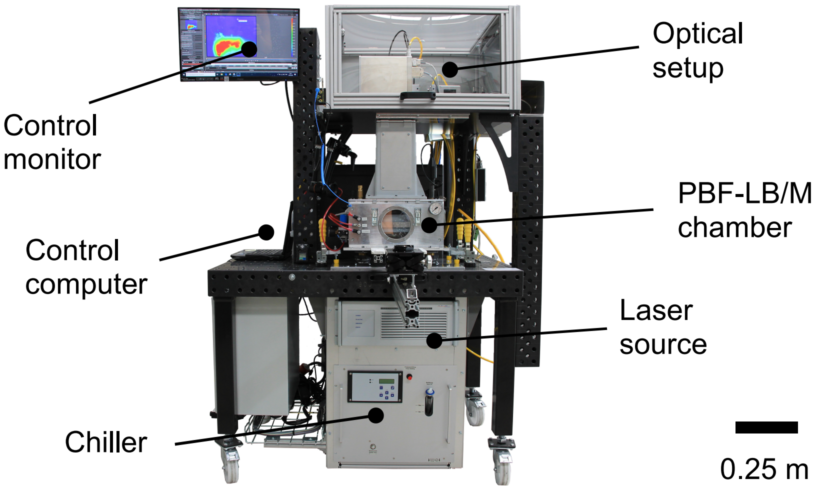

Figure 5.3: Custom PBF-LB/M machine for the melt pool monitoring

Using the methods and findings of P1 and P2, P3 presented a methodology for systematically analyzing the melt pool in the longitudinal section to determine the in-situ variation of the melt pool depth for SS 316L powder blended with the AA AlSi10Mg. Therefore, the laser path was shifted to the edge of the building platform. Microsection analyses showed that the weld seams in the middle of the building platform exhibited a similar depth as the ones on the border of the platform. To quantify the melt pool depth using the thermographic images, over 60 frames were used for each powder blend. The depth showed a slight increase with increasing AlSi10Mg content. The higher laser absorptivity of Si compared to the SS 316L powder presumably led to a deepening of the melt pool. The relative standard deviation of the melt pool depth decreased as the AlSi10Mg content increased.

A 48 % smaller relative standard deviation for the SS 316L powder containing 20 wt.% AlSi10Mg was determined compared to SS 316L without additives. As a measure of the melt pool stability, the change in the relative standard deviation indicated that an AlSi10Mg content above 5 wt.% significantly changed the melt pool dynamics and led to a higher stability. The effect was attributed to the surface tension of the liquid, as the reduced temperature dependence most probably stabilizes the melt pool (cf. Subsection 2.2.3). The observation is consistent with the findings of P1 that lower temperature gradients occur in the molten track when adding Al to SS 316L powder. The Marangoni convection is reduced since smaller temperature gradients lead to a lower Marangoni convection. In contrast, the low vaporization point of Al increases the recoil pressure, possibly reducing the melt pool stability. However, the results show that the effect of the vaporization might play a subordinate role. The in-situ measuring and evaluation principle was validated with micrographs of the solidified tracks. The tendency of decreasing relative standard deviations of the melt pool depth with increasing content of AlSi10Mg agreed well between the results of the thermographic measurements and the micrographs. However, the mean melt pool depth displayed a difference for 0 wt.% and 1 wt.% AlSi10Mg between both approaches. It was explained by the different spatial resolutions of the systems since the in-situ data were obtained over a length of approx. 1 mm, while the ex-situ data were obtained over a length of approx. 20 mm.

The test bench can be used to determine cooling rates, validate simulation results, and investigate the heat transfer between the gas, the liquid, and the solid. In addition to the findings of P3, the test bench was used to gain calibration and validation data for P4 and P5.

Main findings

The conclusions and RFs presented in WIMMER ET AL. (2022) were as follows:

RF1: Unlike the melt pool monitoring possibilities of commercial PBF-LB/M machines, the novel test bench is suitable for observing the longitudinal section of the melt pool.

RF2: Compared to pure SS 316L powder, the variation of the melt depth was found to be 48 % lower when adding 20 wt.% of AlSi10Mg to the SS 316L powder. By that, the melt pool behavior was significantly stabilized.

RF3: The results indicate that the Marangoni convection may play a major role for the melt pool stability, while the recoil pressure plays a subordinate role.

RF4: The methodology allows quantifying the melt pool dynamics of any material combination without requiring time-consuming ex-situ investigations. Furthermore, it reduces the number of several disturbance variables that may influence the results.

Contributions of the authors

Andreas Wimmer proposed the development of an experimental test bench to evaluate the melt pool in the longitudinal section and was the main author of this published journal article. He planned and coordinated the development of the experimental setup and executed the experiments. Fabian Hofstaetter supported the design of the building chamber, the experiment execution, and the programming activities within the frameworks of his semester's and master's thesis. The thermographic data was analyzed by Andreas Wimmer and Fabian Hofstaetter, who also elaborated the manuscript together. Constantin Jugert performed the microstructure evaluation within the framework of his bachelor's thesis. Katrin Wudy and Michael F. Zaeh edited the manuscript. All authors discussed and commented on the findings.

5.2.4 Publication 4: *Numerical modeling of the melt pool during the in-situ alloying process* according to WIMMER ET AL. (2021)

Although some mechanisms of action have been analyzed and discussed in P1, P2, and P3, a comprehensive understanding of the in-situ alloying process was still lacking. Thus, P4 presented a holistic approach, i.e., an interplay of simulation studies with experimental data to analyze the basic phenomena of the in-situ alloying process.

The meshless SPH method (cf. Section 2.5) was employed for the numerical simulation of a multi-component powder system considering both thermodynamics and fluid mechanics in the solid and melt phase. The approach was to extend the existing framework of WEIRATHER ET AL. (2019) to account for the in-situ alloying by solving an additional advection-diffusion equation for the concentration of additives:

$$\frac{\mathrm{d}C_i}{\mathrm{d}t} = \frac{1}{\rho_i}\sum_{j=1}^{N} V_j \frac{4D_iD_j}{D_i + D_j}\left(\rho_i + \rho_j\right)\frac{r_{ij}\nabla_i W_{ij}}{r_{ij}^2 + \eta^2}\left(C_i - C_j\right). \tag{38}$$

Here, η is the dynamic viscosity, V_j is the volume of particle j, W_{ij} is the kernel function, $r_{ij} = |\mathbf{r}_i - \mathbf{r}_\mathrm{j}|$ is the distance between two particles, ρ_i and ρ_j are the densities, C_i and C_j are the concentrations, and D_i and D_j denote the diffusivities of the respective SPH particles. The fully coupled material model used mixture quantities for all relevant physical properties. The concentration equation was added to the velocity-verlet time-integration scheme of the fluid solver. As a verification of the alloy transport equation, the diffusion process of a concentration jump in a non-moving solute was presented. Already for the moderate numerical resolution with the particle spacing $\Delta x = 1$ µm, a good agreement between the analytical data and the numerical solution was found. This comparison verified the accuracy of the SPH approximation of the analytical model and indicated a correct model implementation.

The numerical framework was validated by comparing the simulated melt pool lengths with the experimental data from single melt tracks for powder blends containing SS 316L as base material and AlSi10Mg as an additive. To implement a temperature-dependent diffusivity in the numerical model, the alloy combination was simplified to an Fe-Al system due to the lack of material data for the alloys mentioned above. The experimental data of the melt pool length was gained by using the methodology presented in P3. The experimental results showed a clear monotonic increase in the melt pool length with increasing additive content. The simulation confirmed this tendency, as the virtual melt pool lengths for the powder blends matched with the experimental results within the standard deviation. However, comparing the simulation and the experimental results for the SS 316L without additives showed that the data overlapped only with two times the standard deviation as tolerance. This was explained by possible inaccuracies in the material models used.

Furthermore, the simulation showed longer-lasting liquid areas within the melt pool for the powders containing additives (see Figure 5.4). These observations were attributed to the fact that the liquidus temperature of AlSi10Mg is much lower than the liquidus temperature of SS 316L. In addition, the simulation showed powder particles of the additives that were not completely molten. For a quantitative comparison with the experiment, a longitudinal microsection of the weld seam was analyzed via SEM and EDS mapping and showed a similar mixing behavior as in the simulation. Due to the marginal advection of a powder particle at the edges of the melt pool, it was concluded that the concentration profile of the partially molten AlSi10Mg particle was dominated by diffusion effects.

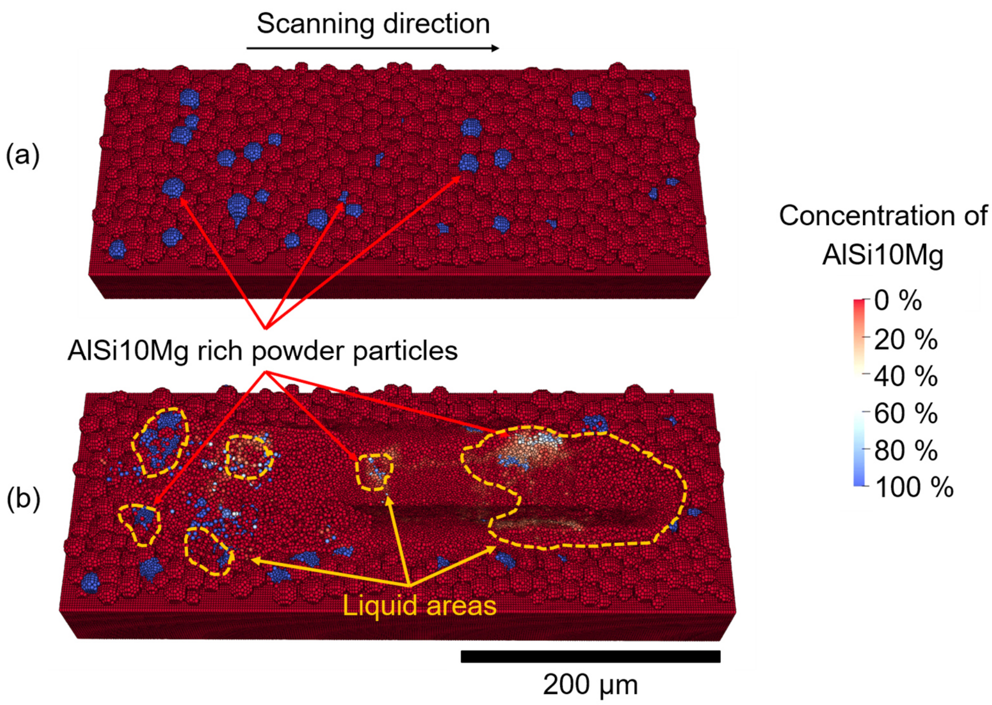

Figure 5.4: (a): Initial powder bed prior to the laser exposure; (b): resulting melt pool during the exposure for SS 316L blended with AlSi10Mg

Main findings

The conclusions and RFs presented in WIMMER ET AL. (2021) were as follows:

RF1: The powder blends consisting of SS 316L and AlSi10Mg were appropriately simplified by taking an Fe-Al system using curve-fitted material parameters.

RF2: As a global validation quantity, the melt pool length showed an increasing trend with a higher AlSi10Mg content for both the simulation and the experiment.

RF3: The simulation results showed a good agreement with experimental SEM-EDS results for the concentration profile of a partially melted AlSi10Mg particle.

RF4: Since the numerical framework is purely physically-based, any material combination can be investigated in terms of, among others, the mixing behavior, the melt pool dimensions, and the temperature field.

Contributions of the authors

Andreas Wimmer was the main author of this published journal paper and had the idea of a numerical model to analyze the melt pool during the in-situ alloying. He planned, coordinated, and executed the programming activities as well as the experiments, and he wrote the article while receiving feedback from the co-authors. Baturay Yalvac contributed significantly to the programming activities regarding the multi-component system within the framework of his master's thesis. Fabian Hofstaetter performed the experiments and the data evaluation within the framework of his master's thesis. Christopher Zoeller and Stefan Adami supported the implementation and bug-fixing within the SPH framework. The manuscript was edited by Stefan Adami, Nikolaus A. Adams, and Michael F. Zaeh. All authors discussed and commented on the findings.

5.2.5 Publication 5: *Numerical and experimental investigations of the hot cracking susceptibility* according to WIMMER ET AL. (2023)

The experimental methodology of P3 and the numerical model of P4 formed the basis for P5, where a numerical framework was elaborated to predict the *HCS* during the PBF-LB/M process and to analyze the influence of additives on the *HCS*.

For the base material, the research-relevant AA 7075 was chosen due to its high *HCS* during the PBF-LB/M process. According to the state of the art, adding Si to AAs is highly effective for reducing hot cracking when the original Si content is too low (cf. Subsection 3.4.1). In the experiments and simulations of P5, the AA 7075 and blends with 2 wt.%, 4 wt.%, and 6 wt.% of Si were processed via PBF-LB/M. The RDG model and the Kou model (cf. Subsection 3.4.2) were selected because both account for a change in the hot cracking behavior due to changes in the chemical composition and are physics-based. They were investigated regarding their capability of predicting the hot cracking behavior of the AA 7075 and the three powder blends.

Since the RDG model needs the thermal gradient as a model parameter, the numerical framework of P4 was used to model the melt pool during the in-situ alloying until solidification. For both hot cracking models, the solidification path was determined using the CALPHAD method (SAUNDERS & MIODOWNIK 1998). The implementation of the RDG model was verified by assuming a non-linear function as an analytical model, since it considers errors in the numerical integration when using the method of the middle Riemann sum (RIEMANN 1867). A linear function would cancel out the errors with this integration method and would, therefore, not be representative for empirical values of f_{S}. For the analytical function $f_{\mathrm{S}}(T) = 1 - T^2$, the numerical implementation and the analytical model agreed very well, indicating a correct model implementation.

For the validation, single-track simulations of pure AA 7075 with three different parameter settings were compared with experimental data obtained by the experimental setup of P3 regarding the geometrical melt pool dimensions. For all parameter settings, the areas of the standard deviations of the experimentally determined melt pool width and depth overlapped with the simulation results. By using the validated numerical process model, the *HCS* was investigated for the AA 7075 and the three blends. The microsections of the cuboids manufactured with the experimental setup showed a high number of hot cracks for the pure AA 7075, a few hot cracks for the blend containing 2 wt.% Si, and no hot cracks for the blends with 4 wt.% Si and 6 wt.% Si. In addition, the cuboids were examined regarding the location of the hot cracks. It was observed that hot cracks tend to form in the center of a single-track. The results of the two models agreed with the results of the experiment, as both predicted a significant decrease of the *HCS* with an increasing Si content in the base powder (see Figure 5.5). In addition, the RDG model was capable of predicting the correct location of possible hot cracks since the highest cracking values were attributed to SPH particles located in the center of the melt pool tail.

Due to the good agreement with the experimental observation, it was concluded that both models are capable of predicting a decreasing *HCS* with an increasing Si content during the PBF-LB/M process. As opposed to the simple hot cracking index from Kou, the RDG model additionally provides information about the location of the hot crack.

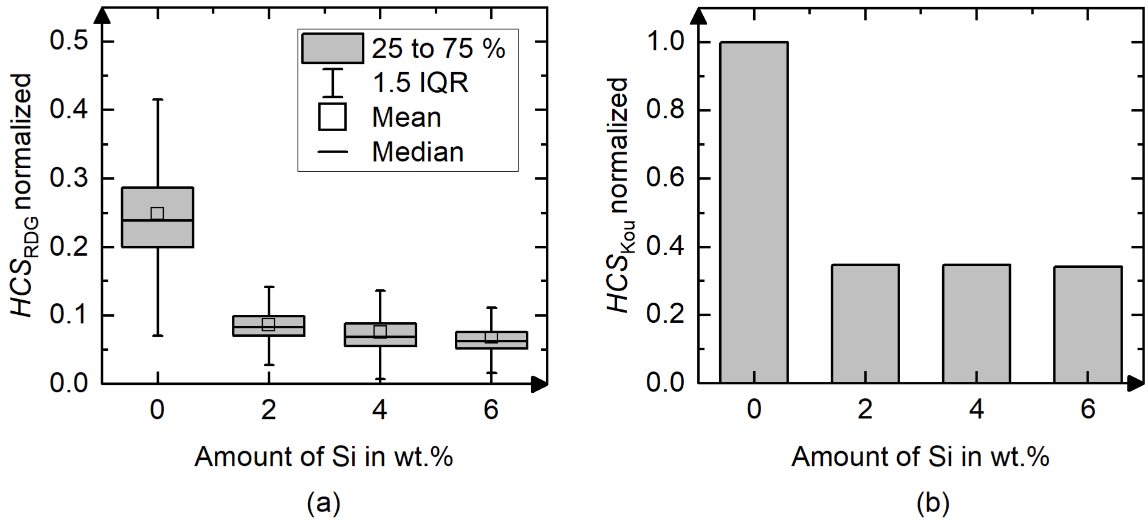

Figure 5.5: (a): HCS predicted by the RDG model; (b): HCS predicted by the Kou model; the error bars indicate the interquartile range (IQR).

Further experimental investigations were conducted to study the type of cracking mechanism (cf. Section 2.4) of the AA 7075 processed with PBF-LB/M. For this reason, a PBF-LB/M manufactured sample was ground and polished to locate the hot crack, rotated by 90°, and again ground and polished up to the hot crack. The crack was examined by Scanning Transmission Electron Microscopy (STEM) and EDX analyses, which showed curved crack flanks and segregations of Mg and Zn in close proximity to the flanks. Since Mg and Zn have a lower melting temperature than Al, the hot crack formation may be attributable to the penetration or the segregation mechanism (cf. Subsection 2.4.3). It was concluded that the various microscopic observations indicate the presence of liquation cracking. The RDG model and the Kou model may therefore be capable of predicting both solidification and liquation cracking.

Main findings

The conclusions and RFs documented in WIMMER ET AL. (2023) were as follows:

RF1: When adding ≥4 wt.% Si to the AA 7075, crack-free samples can be produced.
RF2: The approach of incorporating the RDG model into the SPH simulation was successful, as the prediction of the *HCS* and the predicted location of occurring hot cracks agreed with the experimental results.
RF3: If only the processability of an alloy with a changing chemical composition needs to be investigated, the Kou model provides satisfactory results with less computational effort.
RF4: During the PBF-LB of the AA 7075, several indications suggested the presence of liquation cracking. Therefore, the Kou model and the RDG model may be applicable for both solidification and liquation cracking.

Contributions of the authors

Andreas Wimmer was the main author of this journal publication. Together with Hannes Panzer, he developed the idea to combine the SPH simulation with hot cracking models to investigate the influence of additives on the *HCS*. Andreas Wimmer was responsible for planning, controlling, and executing the experiments, as well as for the numerical modeling. Hannes Panzer contributed significantly to sample preparations, microstructure investigations, and model implementations within the framework of his semester thesis. Christopher Zoeller supported the implementations within the SPH framework and helped to evaluate the simulation results. The manuscript was written by Andreas Wimmer and Hannes Panzer, and edited by Christopher Zoeller, Stefan Adami, Nikolaus A. Adams, and Michael F. Zaeh. All authors discussed and commented on the findings.

5.3 Assessment of the achievements of the scientific objectives

The main objective of this thesis was to create a methodology that is capable of investigating any material combination regarding its processability, its influence on the melt pool dynamics, and its susceptibility to defects (cf. Section 4.2). To evaluate the overall objective, the achievements of the three SOs are elaborated on the following:

SO1 The influence of additives on the temperature field, the mixing behavior, and the melt pool geometry was determined with experimental and analytical methods. The first insights of P1 laid the basis for the subsequent experimental methodology to determine the phase transition with a high temporal and spatial resolution (P2). A quantification of the melt pool depth and length was then performed using a custom PBF-LB/M setup (P3). The capability of the overall methodology was demonstrated by the in-situ alloying of SS 316L powder blended with AlSi10Mg. SO1 can therefore be considered as achieved.

SO2 In P4, a numerical simulation model was presented to investigate the in-situ alloying within the melt pool. The multi-component framework was verified with a suitable scenario. The comparison of melt pool characteristics with experimentally determined in-situ data showed a good agreement. Due to the physics-based approach, any material combination can be analyzed regarding its influence on the melting, the mixing, the thermal behavior, and the Marangoni convection, among others. Thus, SO2 was fulfilled.

SO3 The presented framework of combining the PBF-LB/M process simulation with hot cracking models in P5 was able to correctly predict the material behavior. In particular, the change in the chemical composition of the powder blend and its effect on the *HCS* agreed very well with the experimental findings. The applicability of the framework also seems to be appropriate for liquation cracks, which would allow universal use during the PBF-LB/M process. It can therefore be concluded that SO3 was achieved.

6 Summary, discussion, and outlook

6.1 Summary

In-situ alloying is a promising method to accelerate the design of new alloys for the PBF-LB/M process. Commercially available powders can be mixed prior to the PBF-LB/M process to achieve parts with tailored properties. However, the full potential of this method is not yet utilized, since the experimental effort for investigating suitable material combinations is high, and the mechanisms of action are still not completely explored.

The underlying idea of the research performed within this thesis was to improve the in-situ alloying process by creating a methodology that is capable of investigating any material combination regarding its processability, its influence on the melt pool dynamics, and its susceptibility to hot cracks. The research approach pursued in this dissertation was based on three stages. In the first stage, the influence of additives on the melt pool during the PBF-LB/M process was investigated. An experimental methodology was developed to characterize the melt pool with a high spatial and temporal resolution for different material combinations. The most important findings from stage 1 were the following:

- High-speed thermographic imaging is suitable to quantify the influence of additives on the thermal field of the melt pool. A higher AlSi10Mg content in the SS 316L base powder led to smaller temperature gradients.
- Aluminum segregation within the solidified tracks was observed for 1 wt.% of AlSi10Mg, indicating that the process understanding of the mixing behavior during the liquid phase is crucial for achieving a homogeneous distribution of the elements.
- Analytical modeling, i.e., using the Rosenthal model, is only partially suitable for describing the in-situ alloying process within the melt pool.
- By means of a custom PBF-LB/M machine and a data analysis algorithm, the influence of additives on the melt pool dynamics was quantified. The methodology allowed for determining the melt pool depth and length in in-situ mode.
- Adding AlSi10Mg to SS 316L led to a significant stabilization of the melt pool. The Marangoni convection was believed to be the driving force for the melt pool stability, while the recoil pressure played only a subordinate role.

In stage 2, a numerical framework was set up to comprehensively simulate the physical processes during the in-situ alloying of AlSi10Mg and SS 316L in the melt pool. The model was validated with experimental in-situ data from the previous stage. The main RFs and conclusions in stage 2 were the following:

- A comparison of the melt pool length between the simulation and the experiment showed good agreement. The numerical framework was able to predict increasing melt pool lengths with an increasing additive content.

- The concentration profile of a partially melted AlSi10Mg particle was analyzed in the experiment and in the simulation, and indicated a correct behavior of the concentration-dependent material diffusion in the simulation model.
- The physically-based numerical framework allows to investigate any material combination regarding the mixing behavior, the melt pool dimensions, and the temperature field.

Stage 3 complemented the research approach with a numerical framework that is able to predict the occurrence of hot cracks during the PBF-LB/M process and accounts for a change in the chemical composition. The most important findings were the following:

- Crack-free samples could be produced when adding ≥ 4 wt.% Si to the AA 7075.
- The prediction of the *HCS* and the location of occurring hot cracks agreed with data from the experiments. The combination of the physically-based process model with the RDG model was, thus, successful. If the location of hot cracks is not relevant, the Kou model provides satisfactory results with less computational effort.
- The experimental findings indicated that the Kou model and the RDG model might be applicable for both solidification and liquation cracking.

6.2 Discussion

The scientific contribution of this dissertation and the research progress (RP) concerning the state of the art (cf. Chapter 3) is reflected in the following:

RP1 The experimental setups from the state of the art using visual or infrared imaging focused on observing the melt pool from the co-axial perspective (HOOPER 2018) or the off-axial perspective (KRAUSS ET AL. 2012). The determination of the in-situ melt pool depth was only possible with X-ray imaging (ZHAO ET AL. 2017, MARTIN ET AL. 2019b). However, the systems presented are cost-intensive, allow only the manufacturing of one layer, and are experimental test benches without a proof of transferability to commercial PBF-LB/M machines. In addition, a simultaneous temperature measurement is only possible with a second system. The approach of GOOSSENS & VAN HOOREWEDER (2021) is attractive because it allows for determining the melt pool depth by using coaxial imaging with analytical modeling. However, the deviations from metallographic examinations are high at almost 10 %. The validated experimental method presented in this dissertation using high-speed infrared thermography to analyze the melt pool in the longitudinal section (cf. Subsection 5.2.3) combined with an algorithm that determines the in-situ melt pool geometry (cf. Subsection 5.2.2) is novel. To the best of the knowledge of the author, the influence of additives on the melt pool dynamics, particularly the melt pool depth, was quantified for the first time.

RP2 A comprehensive understanding of the mechanisms of action during the in-situ alloying process within the melt pool was not present in the state of the art. Only a few publications investigated the phenomena, whereby these publications neglected the modeling of the mixing in the liquid phase (CHEN ET AL. 2019, DONG ET AL. 2021), did not consider composition-dependent physical quantities, such as the surface tension

(GAN ET AL. 2017), reflect only two dimensions (KÜNG ET AL. 2021, RUSSELL ET AL. 2018), or were not or only partially validated by experiments (CHOUHAN ET AL. 2022, GU ET AL. 2020). The presented physically-based three-dimensional PBF-LB/M process model of this dissertation (cf. Subsection 5.2.4) can handle a multi-phase and multi-material situation and was validated with in-situ melt pool data. By means of this framework, any material combination can be analyzed regarding, among others, the mixing behavior, the thermal behavior, or the melt pool dimensions. Thus, significant scientific progress was achieved.

RP3 A research deficit in the prior state of the art was present for predicting emerging hot cracks during the PBF-LB/M process. The high potential of the in-situ alloying method for reducing the *HCS* during PBF-LB/M was demonstrated extensively in the experiments. However, no physically-based process model was yet used to predict the influence of additives on the *HCS*. Current research activities aiming at predictive methods focus on the analytical modeling of the temperature field (SONAWANE ET AL. 2021) or on phase-field modeling in combination with the CALPHAD database (CHEN ET AL. 2021, SHAONING ET AL. 2018). Since the temperature field in the mushy zone depends on the phenomena that happen prior to the respective point in time, such as the laser energy absorption, melting, vaporization, convection, diffusion, or thermal radiation, the accuracy of those approaches might lack accuracy due to simplifications. The good agreement of the experimental and simulative results (cf. Subsection 5.2.5) demonstrates the capability of the proposed framework of this dissertation.

6.3 Outlook

This section provides a proposal for an industrial application (IA) using the knowledge gained and an outlook on possible future research activities (RA).

IA According to BANDYOPADHYAY ET AL. (2022), the current alloy design process of metal powder producers usually consists of three steps, see Figure 6.1 (a). After the application considerations in step 1, the alloy design process starts in step 2. Here, the base alloy and the elements are chosen by empirical knowledge or by computational methods using CALPHAD or statistical learning. The possible target alloy is then produced and processed via PBF-LB/M in step 3. With high experimental effort, the target alloy is evaluated regarding its processability and mechanical properties. Occasionally, the defined properties are not achieved and an iterative process between step 2 and step 3 has to be initiated. The experimental effort in step 3 can be significantly reduced by using the methodology presented in this thesis: An intermediate step, marked in orange in Figure 6.1 (b), may be used to predict the processability and to analyze occurring defects, followed by a simulative parameter optimization. If the simulation results confirm the assumptions of the previous step, the evaluation of the mechanical properties will be performed in step 4. If the results do not match the assumptions, an iterative process will be conducted between step 2 and step 3 until the results are satisfactory. By using a validated and reliable simulation framework, the experimental effort can be reduced to the evaluation of the mechanical properties.

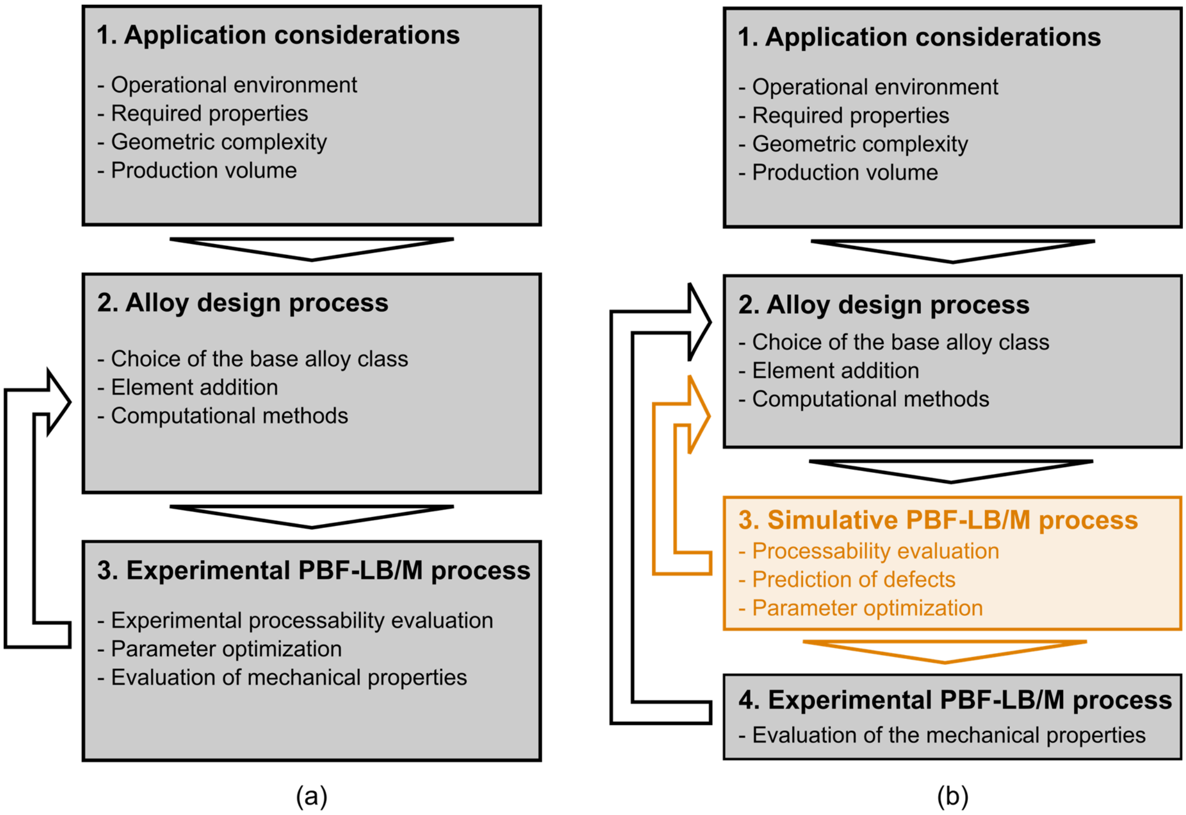

Figure 6.1: (a): Current workflow for the alloy design process for laser-based additive manufacturing processes (adapted from BANDYOPADHYAY ET AL. (2022)); (b): possible workflow in the future using the framework presented in this thesis

RA1 The characteristics of the melt pool in a single track can give initial clues on the final part quality. However, since the PBF-LB/M process is a multi-track and multi-layer process, the subsequent tracks may influence these characteristics. In particular, a re-melting of additives due to the heat input of a second neighboring track may yield different results than in a single track. Moreover, if a whole part should be analyzed regarding hot cracks, the *HCS* has to be calculated for every layer. The phenomenon of crack healing effects due to re-melting needs to be investigated to quantify the cracking behavior in PBF-LB/M parts. To account for that, the computational effort of the SPH simulation tool must be significantly reduced. Before studying the multi-layer process, an intermediate step should be performed, as the second track is influenced by the first one, resulting in fluid mechanical conditions that differ significantly. The framework proposed by ZHANG ET AL. (2021a), termed as SPHinXsys, is able to discretize the fluid and solid equations by different spatial-temporal resolutions. In the case of the in-situ alloying process, the relevant regions could be simulated with a higher resolution and the less interesting regions could be resolved coarser to save computational time. Since the choice of these regions is not straightforward, research work must be performed to create a systematic procedure.

RA2 The validity and reliability of simulation frameworks significantly depend on the quality of experimentally determined validation data. In contrast to the majority of the validation approaches in the literature, this work used in-situ data from the melt pool. However, as future simulation tools will attempt to model more and more phenomena and will try to increase their predictive capabilities, the melt pool geometry may no longer be sufficient as a global validation quantity. By using a multi-sensor data fusion approach, as presented by HARBIG ET AL. (2022), in combination with the experimental methodology of stage 1, the information of the single monitoring system could be extended. Since different monitoring systems will produce a high amount of data, indicators representing process characteristics need to be developed. These indicators should be tailored for a specific validation quantity, e.g., the in-situ melt pool geometry and process anomalies such as elevated temperatures that trigger a defect generation. By means of deterministic models, the data fusion between different monitoring systems may improve the defect detection. The determined data can then be used to validate or calibrate the simulation framework.

RA3 With an improved code parallelization combined with the use of graphical processing units or with the approach of RA1, the implementation into a multi-objective optimization algorithm, i.e., into the algorithm of DREANO ET AL. (2022), might be promising. The implementation of a physically-based process simulation at appropriate positions in the algorithm could significantly improve the predictive quality of a target alloy. In particular, the combination of the analytical modeling, the empirical knowledge, the statistical learning, and the process simulation utilizes the strengths of each method.

Finally, with the results of this dissertation, a decisive step has been taken toward a reliable and cost-effective methodology for designing new alloys suitable for the PBF-LB/M process.

7 References

Please note that wherever no bibliographic indices are given, the information is not available or not known to the author.

ADAMI 2014

Adami, S.: Modeling and Simulation of Multiphase Phenomena with Smoothed Particle Hydrodynamics. Dissertation. TECHNISCHE UNIVERSITÄT MÜNCHEN. München (2014).

ANTONYSAMY ET AL. 2013

Antonysamy, A. A.; Meyer, J.; Prangnell, P. B.: Effect of build geometry on the β-grain structure and texture in additive manufacture of Ti6Al4V by selective electron beam melting. Materials Characterization 84 (2013), pp. 153–168.

AVERSA ET AL. 2019

Aversa, A.; Marchese, G.; Saboori, A.; Bassini, E.; Manfredi, D.; Biamino, S.; Ugues, D.; Fino, P.; Lombardi, M.: New Aluminum Alloys Specifically Designed for Laser Powder Bed Fusion: A Review. Materials 12 (2019) 7.

BANDYOPADHYAY ET AL. 2022

Bandyopadhyay, A.; Traxel, K. D.; Lang, M.; Juhasz, M.; Eliaz, N.; Bose, S.: Alloy design via additive manufacturing: Advantages, challenges, applications and perspectives. Materials Today 52 (2022), pp. 207–224.

BARTKOWIAK ET AL. 2011

Bartkowiak, K.; Ullrich, S.; Frick, T.; Schmidt, M.: New Developments of Laser Processing Aluminium Alloys via Additive Manufacturing Technique. Physics Procedia 12 (2011), pp. 393–401.

BOBEL ET AL. 2019

Bobel, A.; Hector, L. G.; Chelladurai, I.; Sachdev, A. K.; Brown, T.; Poling, W. A.; Kubic, R.; Gould, B.; Zhao, C.; Parab, N.; Greco, A.; Sun, T.: In situ synchrotron X-ray imaging of 4140 steel laser powder bed fusion. Materialia 6 (2019), p. 100306.

BOSIO ET AL. 2022

Bosio, F.; Manfredi, D.; Lombardi, M.: Homogenization of an Al alloy processed by laser powder bed fusion in-situ alloying. Journal of Alloys and Compounds 904 (2022), p. 164079.

BOURELL ET AL. 2017

Bourell, D.; Kruth, J. P.; Leu, M.; Levy, G.; Rosen, D.; Beese, A. M.; Clare, A.: Materials for additive manufacturing. CIRP Annals 66 (2017) 2, pp. 659–681.

BRACKBILL ET AL. 1992

Brackbill, J.; Kothe, D.; Zemach, C.: A continuum method for modeling surface tension. Journal of Computational Physics 100 (1992) 2, pp. 335–354.

CALTA ET AL. 2018

Calta, N. P.; Wang, J.; Kiss, A. M.; Martin, A. A.; Depond, P. J.; Guss, G. M.; Thampy, V.; Fong, A. Y.; Weker, J. N.; Stone, K. H.; Tassone, C. J.; Kramer, M. J.; Toney, M. F.; van Buuren, A.; Matthews, M. J.: An instrument for in situ time-resolved X-ray imaging and diffraction of laser powder bed fusion additive manufacturing processes. The Review of scientific instruments 89 (2018) 5, p. 55101.

CHALMERS B. 1964

Chalmers B.: Principles of Solidification. New York: Wiley 1964. ISBN: 0471143251.

CHEN ET AL. 2019

Chen, C.; Gu, D.; Dai, D.; Du, L.; Wang, R.; Ma, C.; Xia, M.: Laser additive manufacturing of layered TiB2/Ti6Al4V multi-material parts: Understanding thermal behavior evolution. Optics & Laser Technology 119 (2019), p. 105666.

CHEN ET AL. 2021

Chen, D.; Wang, J.; Zhang, C.: Coupling phase-field model and CFD for hot cracking predictions of Al-Li alloys. Computational Materials Science 192 (2021), p. 110361.

CHENG ET AL. 2018

Cheng, B.; Lydon, J.; Cooper, K.; Cole, V.; Northrop, P.; Chou, K.: Melt pool sensing and size analysis in laser powder-bed metal additive manufacturing. Journal of Manufacturing Processes 32 (2018), pp. 744–753.

CHOUHAN ET AL. 2022

Chouhan, A.; Hesselmann, M.; Toenjes, A.; Mädler, L.; Ellendt, N.: Numerical modelling of in-situ alloying of Al and Cu using the laser powder bed fusion process: A study on the effect of energy density and remelting on deposited track homogeneity. Additive Manufacturing 59 (2022), p. 103179.

CICALĂ ET AL. 2005

Cicală, E.; Duffet, G.; Andrzejewski, H.; Grevey, D.; Ignat, S.: Hot cracking in Al–Mg–Si alloy laser welding – operating parameters and their effects. Materials Science and Engineering: A 395 (2005) 1, pp. 1–9.

CIRAUD 1973

Property right DE2263777A1. LeOne Isaure Marie Ciraud. Ciraud, P.: Verfahren und Vorrichtung zur Herstellung beliebiger Gegenstände aus beliebigem schmelzbarem Material.

CLIJSTERS ET AL. 2014

Clijsters, S.; Craeghs, T.; Buls, S.; Kempen, K.; Kruth, J.-P.: In situ quality control of the selective laser melting process using a high-speed, real-time melt pool monitoring system. The International Journal of Advanced Manufacturing Technology 75 (2014) 5, pp. 1089–1101.

CLYNE & DAVIES 1979
Clyne, T. W.; Davies, G. J.: Solidification and Casting of Metals. The Metals Society (1979), pp. 275–278.

COLLINS ET AL. 2016
Collins, P. C.; Brice, D. A.; Samimi, P.; Ghamarian, I.; Fraser, H. L.: Microstructural Control of Additively Manufactured Metallic Materials. Annual Review of Materials Research 46 (2016) 1, pp. 63–91.

CONIGLIO & CROSS 2013
Coniglio, N.; Cross, C. E.: Initiation and growth mechanisms for weld solidification cracking. International Materials Reviews 58 (2013) 7, pp. 375–397.

CUNNINGHAM ET AL. 2019
Cunningham, R.; Zhao, C.; Parab, N.; Kantzos, C.; Pauza, J.; Fezzaa, K.; Sun, T.; Rollett, A. D.: Keyhole threshold and morphology in laser melting revealed by ultrahigh-speed x-ray imaging. Science (New York, N.Y.) 363 (2019) 6429, pp. 849–852.

DADBAKHSH ET AL. 2018
Dadbakhsh, S.; Mertens, R.; Vanmeensel, K.; Vleugels, J.; van Humbeeck, J.; Kruth, J.-P.: In situ alloying and reinforcing of Al6061 during selective laser melting. Procedia CIRP 74 (2018), pp. 39–43.

DAHLE & STJOHN 1998
Dahle, A. K.; StJohn, D. H.: Rheological behaviour of the mushy zone and its effect on the formation of casting defects during solidification. Acta Materialia 47 (1998) 1, pp. 31–41.

DECKARD 1989
Property right US4863538A. University of Texas System. Deckard, C. R.: Method and apparatus for producing parts by selective sintering.

DIN EN ISO/ASTM 52900:2022-03
DIN EN ISO/ASTM 52900:2022-03: Additive manufacturing - General principles - Fundamentals and vocabulary. Berlin, Germany: Beuth 2022.

DONG ET AL. 2021
Dong, Y. P.; Li, Y. L.; Zhou, S. Y.; Zhou, Y. H.; Dargusch, M. S.; Peng, H. X.; Yan, M.: Cost-affordable Ti-6Al-4V for additive manufacturing: Powder modification, compositional modulation and laser in-situ alloying. Additive Manufacturing 37 (2021), p. 101699.

DOUBENSKAIA ET AL. 2013
Doubenskaia, M.; Pavlov, M.; Grigoriev, S.; Smurov, I.: Definition of brightness temperature and restoration of true temperature in laser cladding using infrared camera. Surface and Coatings Technology 220 (2013), pp. 244–247.

DREANO ET AL. 2022
Dreano, A.; Favre, J.; Desrayaud, C.; Chanin-Lambert, P.; Wimmer, A.; Zaeh, M. F.: Computational design of a crack-free aluminum alloy for additive manufacturing. Additive Manufacturing 55 (2022), p. 102876.

DUTRA FRAGA FILHO 2019
Dutra Fraga Filho, C. A.: Smoothed Particle Hydrodynamics. Fundamentals and Basic Applications in Continuum Mechanics. Cham: Springer International Publishing 2019. ISBN: 9783030007737.

EGOROV ET AL. 2020
Egorov, S. A.; Khmyrov, R. S.; Korotkov, A. D.; Gusarov, A. V.: Experimental study and modeling of melt pool in laser powder-bed fusion of thin walls. Procedia CIRP 94 (2020), pp. 372–377.

FEURER 1977
Feurer, U.: Influence of alloy composition and solidification conditions on dendrite arm spacing, feeding and hot tearing properties of aluminum alloys. Proceedings International Symposium on Engineering Alloys, Delft, The Netherlands (1977), pp. 131–145.

FLINT ET AL. 2020
Flint, T. F.; Scotti, L.; Basoalto, H. C.; Smith, M. C.: A thermal fluid dynamics framework applied to multi-component substrates experiencing fusion and vaporisation state transitions. Communications Physics 3 (2020) 1, p. 196.

FRIEDLANDER & SERRE 2003
Friedlander, S.; Serre, D.: Handbook of Mathematical Fluid Dynamics. Amsterdam, The Netherlands: North-Holland 2003. ISBN: 1874-5792.

FUHRICH ET AL. 2001
Fuhrich, T.; Berger, P.; Hügel, H.: Marangoni effect in laser deep penetration welding of steel. Journal of Laser Applications 13 (2001) 5, pp. 178–186.

FURUMOTO ET AL. 2022
Furumoto, T.; Oishi, K.; Abe, S.; Tsubouchi, K.; Yamaguchi, M.; Clare, A. T.: Evaluating the thermal characteristics of laser powder bed fusion. Journal of Materials Processing Technology 299 (2022), p. 117384.

GAN ET AL. 2017
Gan, Z.; Yu, G.; He, X.; Li, S.: Numerical simulation of thermal behavior and multicomponent mass transfer in direct laser deposition of Co-base alloy on steel. International Journal of Heat and Mass Transfer 104 (2017), pp. 28–38.

GILLESPIE ET AL. 2021
Gillespie, J.; Yeoh, W. Y.; Zhao, C.; Parab, N. D.; Sun, T.; Rollett, A. D.; Lan, B.; Kube, C. M.: In situ characterization of laser-generated melt pools using synchronized ultrasound and high-speed X-ray imaging. The Journal of the Acoustical Society of America 150 (2021) 4, p. 2409.

GINGOLD & MONAGHAN 1977
Gingold, R. A.; Monaghan, J. J.: Smoothed particle hydrodynamics: theory and application to non-spherical stars. Monthly Notices of the Royal Astronomical Society 181 (1977) 3, pp. 375–389.

GIORJAO ET AL. 2021
Giorjao, R.; Sutton, B.; Ramirez, A.: New Composition Based Technique for Solidification Cracking Resistance Evaluation. Metallurgical and Materials Transactions A 52 (2021) 6, pp. 2512–2521.

GOOSSENS & VAN HOOREWEDER 2021
Goossens, L. R.; van Hooreweder, B.: A virtual sensing approach for monitoring melt-pool dimensions using high speed coaxial imaging during laser powder bed fusion of metals. Additive Manufacturing 40 (2021), p. 101923.

GORSSE ET AL. 2017
Gorsse, S.; Hutchinson, C.; Gouné, M.; Banerjee, R.: Additive manufacturing of metals: a brief review of the characteristic microstructures and properties of steels, Ti-6Al-4V and high-entropy alloys. Science and Technology of Advanced Materials 18 (2017) 1, pp. 584–610.

GOULD ET AL. 2021
Gould, B.; Wolff, S.; Parab, N.; Zhao, C.; Lorenzo-Martin, M. C.; Fezzaa, K.; Greco, A.; Sun, T.: In Situ Analysis of Laser Powder Bed Fusion Using Simultaneous High-Speed Infrared and X-ray Imaging. JOM 73 (2021) 1, pp. 201–211.

GU ET AL. 2020
Gu, H.; Wei, C.; Li, L.; Han, Q.; Setchi, R.; Ryan, M.; Li, Q.: Multi-physics modelling of molten pool development and track formation in multi-track, multi-layer and multi-material selective laser melting. International Journal of Heat and Mass Transfer 151 (2020), p. 119458.

GULLIVER 1915
Gulliver, G. H.: The quantitative effect of rapid cooling upon the constitution of binary alloys. Journal of the Institute of Metals 13 (1915), pp. 263–291.

GUMPINGER ET AL. 2021
Gumpinger, J.; Seifi, M.; Shamsaei, N.; Seidel, C.; Russell, R. W.: Recent progress on global standardization. In: Yadroitsev, I. et al. (Eds.): Fundamentals of Laser Powder Bed Fusion of Metals : Additive Manufacturing Materials and Technologies. Amsterdam, The Netherlands: Elsevier 2021, pp. 563–582. ISBN: 978-0-12-824090-8.

GUO ET AL. 2022
Guo, Q.; Qu, M.; Escano, L. I.; Hojjatzadeh, S. M.; Young, Z.; Fezzaa, K.; Chen, L.: Revealing melt flow instabilities in laser powder bed fusion additive manufacturing of aluminum alloy via in-situ high-speed X-ray imaging. International Journal of Machine Tools and Manufacture 175 (2022), p. 103861.

HANEMANN ET AL. 2019

Hanemann, T.; Carter, L. N.; Habschied, M.; Adkins, N. J.; Attallah, M. M.; Heilmaier, M.: In-situ alloying of AlSi10Mg+Si using Selective Laser Melting to control the coefficient of thermal expansion. Journal of Alloys and Compounds 795 (2019), pp. 8–18.

HARBIG ET AL. 2022

Harbig, J.; Wenzler, D. L.; Baehr, S.; Kick, M. K.; Merschroth, H.; Wimmer, A.; Weigold, M.; Zaeh, M. F.: Methodology to Determine Melt Pool Anomalies in Powder Bed Fusion of Metals Using a Laser Beam by Means of Process Monitoring and Sensor Data Fusion. Materials 15 (2022) 3, p. 1265.

HEIGEL & LANE 2018

Heigel, J. C.; Lane, B. M.: Measurement of the Melt Pool Length During Single Scan Tracks in a Commercial Laser Powder Bed Fusion Process. Journal of Manufacturing Science and Engineering 140 (2018) 5, p. 51012.

HILLS ET AL. 1983

Hills, R. N.; Loper, D.; Roberts, P. H.: A thermodynamically consistent model of a mushy zone. The Quarterly Journal of Mechanics and Applied Mathematics 36 (1983) 4, pp. 505–540.

HOLZER ET AL. 2016

Holzer, M.; Hofmann, K.; Mann, V.; Hugger, F.; Roth, S.; Schmidt, M.: Change of Hot Cracking Susceptibility in Welding of High Strength Aluminum Alloy AA 7075. Physics Procedia 83 (2016), pp. 463–471.

HOOPER 2018

Hooper, P. A.: Melt pool temperature and cooling rates in laser powder bed fusion. Additive Manufacturing 22 (2018), pp. 548–559.

HOUSHOLDER 1981

Property right US4247508A. DTM Corporation. Housholder, R. F.: Molding process.

HU & ADAMS 2006

Hu, X. Y.; Adams, N. A.: A multi-phase SPH method for macroscopic and mesoscopic flows. Journal of Computational Physics 213 (2006) 2, pp. 844–861.

HUBER 2014

Huber, S.: In-situ-Legierungsbestimmung beim Laserstrahlschweißen. Dissertation. TECHNISCHE UNIVERSITÄT MÜNCHEN. München (2014).

HUBER ET AL. 2021

Huber, F.; Rasch, M.; Schmidt, M.: Laser Powder Bed Fusion (PBF-LB/M) Process Strategies for In-Situ Alloy Formation with High-Melting Elements. Metals 11 (2021) 2, p. 336.

HYER ET AL. 2021

Hyer, H.; Le, Z.; Mehta, A.; Park, S.; Huynh, T.; Song, S.; Bai, Y.; Cho, K.;

McWilliams, B.; Sohn, Y.: Composition-dependent solidification cracking of aluminum-silicon alloys during laser powder bed fusion. Acta Materialia 208 (2021), p. 116698.

INFRATEC GMBH 2004
Infratec GmbH: Einführung in die Theorie und Praxis der Infrarot-Thermografie. 2004.

ION 2000
Ion, J. C.: Laser beam welding of wrought aluminium alloys. Science and Technology of Welding and Joining 5 (2000) 5, pp. 265–276.

ISO/ASTM 52900:2015
ISO/ASTM 52900:2015: Additive manufacturing — General principles — Terminology. Berlin, Germany: Beuth 2015.

KANG ET AL. 2017
Kang, N.; Coddet, P.; Dembinski, L.; Liao, H.; Coddet, C.: Microstructure and strength analysis of eutectic Al-Si alloy in-situ manufactured using selective laser melting from elemental powder mixture. Journal of Alloys and Compounds 691 (2017), pp. 316–322.

KANNENGIESSER & BOELLINGHAUS 2014
Kannengiesser, T.; Boellinghaus, T.: Hot cracking tests—an overview of present technologies and applications. Welding in the World 58 (2014) 3, pp. 397–421.

KATZ-DEMYANETZ ET AL. 2020
Katz-Demyanetz, A.; Koptyug, A.; Popov, V. V.: In-situ Alloying as a Novel Methodology in Additive Manufacturing. (Eds.): 2020 IEEE 10th International Conference Nanomaterials: Applications & Properties (NAP) 2020, p. 02SAMA05.

KHAIRALLAH ET AL. 2016
Khairallah, S. A.; Anderson, A. T.; Rubenchik, A.; King, W. E.: Laser powder-bed fusion additive manufacturing: Physics of complex melt flow and formation mechanisms of pores, spatter, and denudation zones. Acta Materialia 108 (2016), pp. 36–45.

KHAIRALLAH & ANDERSON 2014
Khairallah, S. A.; Anderson, A.: Mesoscopic simulation model of selective laser melting of stainless steel powder. Journal of Materials Processing Technology 214 (2014) 11, pp. 2627–2636.

KHANZADEH ET AL. 2019
Khanzadeh, M.; Chowdhury, S.; Tschopp, M. A.; Doude, H. R.; Marufuzzaman, M.; Bian, L.: In-situ monitoring of melt pool images for porosity prediction in directed energy deposition processes. IISE Transactions 51 (2019) 5, pp. 437–455.

KING ET AL. 2014
King, W. E.; Barth, H. D.; Castillo, V. M.; Gallegos, G. F.; Gibbs, J. W.; Hahn, D. E.;

Kamath, C.; Rubenchik, A. M.: Observation of keyhole-mode laser melting in laser powder-bed fusion additive manufacturing. Journal of Materials Processing Technology 214 (2014) 12, pp. 2915–2925.

KISS ET AL. 2019
Kiss, A. M.; Fong, A. Y.; Calta, N. P.; Thampy, V.; Martin, A. A.; Depond, P. J.; Wang, J.; Matthews, M. J.; Ott, R. T.; Tassone, C. J.; Stone, K. H.; Kramer, M. J.; van Buuren, A.; Toney, M. F.; Nelson Weker, J.: Laser-Induced Keyhole Defect Dynamics during Metal Additive Manufacturing. Advanced Engineering Materials 21 (2019) 10, p. 1900455.

KÖRNER ET AL. 2011
Körner, C.; Attar, E.; Heinl, P.: Mesoscopic simulation of selective beam melting processes. Journal of Materials Processing Technology 211 (2011) 6, pp. 978–987.

KOU 2015a
Kou, S.: A simple index for predicting the susceptibility to solidification cracking. Weld. J 94 (2015) 12, pp. 374–388.

KOU 2015b
Kou, S.: A criterion for cracking during solidification. Acta Materialia 88 (2015), pp. 366–374.

KRAUSS ET AL. 2012
Krauss, H.; Eschey, C.; Zaeh, M. F.: Thermography for Monitoring the Selective Laser Melting Process. International Solid Freeform Fabrication Symposium, Austin, Texas (USA) (2012), pp. 999–1014.

KREITH ET AL. 2000
Kreith, F.; Timmerhaus, K.; Lior, N.; Shaw, H.; Shah, R. K.; Bell, K. J.: The CRC Handbook of Thermal Engineering. Heidelberg, Germany: Springer 2000. ISBN: 3662131560.

KÜNG ET AL. 2021
Küng, V. E.; Scherr, R.; Markl, M.; Körner, C.: Multi-material model for the simulation of powder bed fusion additive manufacturing. Computational Materials Science 194 (2021), p. 110415.

LANE ET AL. 2016
Lane, B.; Moylan, S.; Whitenton, E. P.; Ma, L.: Thermographic measurements of the commercial laser powder bed fusion process at NIST. Rapid Prototyping Journal 22 (2016) 5, pp. 778–787.

LE ET AL. 2021
Le, T.-N.; Lee, M.-H.; Lin, Z.-H.; Tran, H.-C.; Lo, Y.-L.: Vision-based in-situ monitoring system for melt-pool detection in laser powder bed fusion process. Journal of Manufacturing Processes 68 (2021), pp. 1735–1745.

LEUNG ET AL. 2018

Leung, C. L.; Marussi, S.; Atwood, R. C.; Towrie, M.; Withers, P. J.; Lee, P. D.: In situ X-ray imaging of defect and molten pool dynamics in laser additive manufacturing. Nature Communications 9 (2018) 1, p. 1355.

LI ET AL. 2020

Li, L.; Li, R.; Yuan, T.; Chen, C.; Zhang, Z.; Li, X.: Microstructures and tensile properties of a selective laser melted Al–Zn–Mg–Cu (Al7075) alloy by Si and Zr microalloying. Materials Science and Engineering: A 787 (2020), p. 139492.

LIMMANEEVICHITR & KOU 2000

Limmaneevichitr, C.; Kou, S.: Simulated weld pools containing a surface active agent. Weld. J 79 (2000) 11, pp. 325–331.

LIPPOLD 2015

Lippold, J. C.: Welding Metallurgy and Weldability. Hoboken, New Jersey: Wiley 2015. ISBN: 9781118230701.

LIU ET AL. 2017

Liu, J.; Duarte, H. P.; Kou, S.: Evidence of back diffusion reducing cracking during solidification. Acta Materialia 122 (2017), pp. 47–59.

LIU & LIU 2003

Liu, G. R.; Liu, M. B.: Smoothed Particle Hydrodynamics: A Meshfree Particle Method: WORLD SCIENTIFIC 2003. ISBN: 978-981-4365-57-4.

LUCY 1977

Lucy, L. B.: A numerical approach to the testing of the fission hypothesis. The astronomical journal 82 (1977), pp. 1013–1024.

MAIR ET AL. 2021

Mair, P.; Kaserer, L.; Braun, J.; Weinberger, N.; Letofsky-Papst, I.; Leichtfried, G.: Microstructure and mechanical properties of a TiB2-modified Al–Cu alloy processed by laser powder-bed fusion. Materials Science and Engineering: A 799 (2021), p. 140209.

MANI ET AL. 2015

Mani, M.; Lane, B.; Donmez, A.; Feng, S.; Moylan, S.; Fesperman, R.: Measurement Science Needs for Real-time Control of Additive Manufacturing Powder Bed Fusion Processes. NIST Interagency/Internal Report (NISTIR) (2015) 8036.

MARTIN ET AL. 2017

Martin, J. H.; Yahata, B. D.; Hundley, J. M.; Mayer, J. A.; Schaedler, T. A.; Pollock, T. M.: 3D printing of high-strength aluminium alloys. Nature 549 (2017) 7672, pp. 365–369.

MARTIN ET AL. 2019a

Martin, A. A.; Calta, N. P.; Hammons, J. A.; Khairallah, S. A.; Nielsen, M. H.; Shuttlesworth, R. M.; Sinclair, N.; Matthews, M. J.; Jeffries, J. R.; Willey, T. M.; Lee,

J. R.: Ultrafast dynamics of laser-metal interactions in additive manufacturing alloys captured by in situ X-ray imaging. Materials Today Advances 1 (2019), p. 100002.

MARTIN ET AL. 2019b
Martin, A. A.; Calta, N. P.; Khairallah, S. A.; Wang, J.; Depond, P. J.; Fong, A. Y.; Thampy, V.; Guss, G. M.; Kiss, A. M.; Stone, K. H.; Tassone, C. J.; Nelson Weker, J.; Toney, M. F.; van Buuren, T.; Matthews, M. J.: Dynamics of pore formation during laser powder bed fusion additive manufacturing. Nature Communications 10 (2019) 1, p. 1987.

MARTINEZ ET AL. 2019
Martinez, R.; Todd, I.; Mumtaz, K.: In situ alloying of elemental Al-Cu12 feedstock using selective laser melting. Virtual and Physical Prototyping 14 (2019) 3, pp. 242–252.

MATSUDA ET AL. 1982
Matsuda, F.; Nakagawa, H.; Sorada, K.: Dynamic observation of solidification and solidification cracking during welding with optical microscope (I): Solidification front and behavior of cracking (materials, metallurgy & weldability). Transactions of JWRI 11 (1982) 2, pp. 67–77.

MEHRPOUYA ET AL. 2022
Mehrpouya, M.; Tuma, D.; Vaneker, T.; Afrasiabi, M.; Bambach, M.; Gibson, I.: Multimaterial powder bed fusion techniques. Rapid Prototyping Journal 28 (2022) 11, pp. 1–19.

MEINERS 1999
Meiners, W.: Direktes Selektives Laser Sintern einkomponentiger metallischer Werkstoffe. Dissertation. RWTH AACHEN. Aachen (1999).

MERTENS ET AL. 2021
Mertens, R.; Baert, L.; Vanmeensel, K.; van Hooreweder, B.: Laser powder bed fusion of high strength aluminum. Material Design & Processing Communications 3 (2021) 5.

MINKINA & DUDZIK 2009
Minkina, W.; Dudzik, S.: Infrared Thermography. Errors and Uncertainties. New York, NY: John Wiley & Sons 2009. ISBN: 9780470682234.

MOHR ET AL. 2020
Mohr, G.; Altenburg, S. J.; Ulbricht, A.; Heinrich, P.; Baum, D.; Maierhofer, C.; Hilgenberg, K.: In-Situ Defect Detection in Laser Powder Bed Fusion by Using Thermography and Optical Tomography - Comparison to Computed Tomography. Metals 10 (2020) 1, p. 103.

MONAGHAN 1992
Monaghan, J. J.: Smoothed Particle Hydrodynamics. Annual Review of Astronomy and Astrophysics 30 (1992) 1, pp. 543–574.

MONAGHAN 1994

Monaghan, J. J.: Simulating Free Surface Flows with SPH. Journal of Computational Physics 110 (1994) 2, pp. 399–406.

MONAGHAN 2005

Monaghan, J. J.: Smoothed particle hydrodynamics. Reports on Progress in Physics 68 (2005) 8, p. 1703.

MONAGHAN & KOCHARYAN 1995

Monaghan, J. J.; Kocharyan, A.: SPH simulation of multi-phase flow. Computer Physics Communications 87 (1995) 1, pp. 225–235.

MONTERO-SISTIAGA ET AL. 2016

Montero-Sistiaga, M. L.; Mertens, R.; Vrancken, B.; Wang, X.; van Hooreweder, B.; Kruth, J.-P.; van Humbeeck, J.: Changing the alloy composition of Al7075 for better processability by selective laser melting. Journal of Materials Processing Technology 238 (2016), pp. 437–445.

MUKHERJEE ET AL. 2016

Mukherjee, T.; Zuback, J. S.; De, A.; DebRoy, T.: Printability of alloys for additive manufacturing. Scientific Reports 6 (2016) 1, p. 19717.

PARAB ET AL. 2018

Parab, N. D.; Zhao, C.; Cunningham, R.; Escano, L. I.; Fezzaa, K.; Everhart, W.; Rollett, A. D.; Chen, L.; Sun, T.: Ultrafast X-ray imaging of laser-metal additive manufacturing processes. Journal of synchrotron radiation 25 (2018) Pt 5, pp. 1467–1477.

PARAB ET AL. 2019

Parab, N. D.; Zhao, C.; Cunningham, R.; Escano, L. I.; Gould, B.; Wolff, S.; Guo, Q.; Xiong, L.; Kantzos, C.; Pauza, J.; Fezzaa, K.; Greco, A.; Rollett, A.; Chen, L.; Sun, T.: High-speed Synchrotron X-ray Imaging of Laser Powder Bed Fusion Process. Synchrotron Radiation News 32 (2019) 2, pp. 4–8.

PROKHOROV 1956

Prokhorov, N. N.: The problem of the strength of metals while solidifying during welding. Svarochnoe Proizvodstvo 6 (1956), pp. 5–11.

PROKHOROV 1971

Prokhorov, N. N.: Fundamentals of the theory for technological strength of metals while crystallising during welding. Transactions of the Japan Welding Society 2 (1971) 2, pp. 205–213.

QIU ET AL. 2019

Qiu, C.; Wang, Z.; Aladawi, A. S.; Kindi, M. A.; Hatmi, I. A.; Chen, H.; Chen, L.: Influence of Laser Processing Strategy and Remelting on Surface Structure and Porosity Development during Selective Laser Melting of a Metallic Material. Metallurgical and Materials Transactions A 50 (2019) 9, pp. 4423–4434.

RAPPAZ ET AL. 1999

Rappaz, M.; Drezet, J.-M.; Gremaud, M.: A new hot-tearing criterion. Metallurgical and Materials Transactions A 30 (1999) 2, pp. 449–455.

RIEMANN 1867

Riemann, B.: Ueber die Darstellbarkeit einer Function durch eine trigonometrische Reihe. Habilitation thesis. KOENIGLICHE GESELLSCHAFT DER WISSENSCHAFTEN ZU GOETTINGEN. Goettingen (1867).

RIENER ET AL. 2022

Riener, K.; Nagler, A.; Letofsky-Papst, I.; Leichtfried, G.: Processing of Aluminum Alloy 6182 with High Scanning Speed in LPBF by In-Situ Alloying with Zr and Ti Powder. Alloys 1 (2022) 3, pp. 277–287.

ROSENTHAL 1946

Rosenthal, D.: The Theory of Moving Sources of Heat and Its Application to Metal Treatments. Trans. ASME 68 (1946) 8, pp. 849–865.

RUSSELL ET AL. 2018

Russell, M. A.; Souto-Iglesias, A.; Zohdi, T. I.: Numerical simulation of Laser Fusion Additive Manufacturing processes using the SPH method. Computer Methods in Applied Mechanics and Engineering 341 (2018), pp. 163–187.

SAUNDERS & MIODOWNIK 1998

Saunders, N.; Miodownik, A. P.: CALPHAD (calculation of phase diagrams). A comprehensive guide. Oxford, New York: Pergamon 1998. ISBN: 9780080528434.

SAVAGE ET AL. 1976

Savage, W. F.; Nippes, E. F.; Szekeres, E. S.: Study of weld interface phenomena in a low alloy steel. Welding Journal 55 (1976) 9, p. 260.

SCIME & BEUTH 2019

Scime, L.; Beuth, J.: Using machine learning to identify in-situ melt pool signatures indicative of flaw formation in a laser powder bed fusion additive manufacturing process. Additive Manufacturing 25 (2019), pp. 151–165.

SHAONING ET AL. 2018

Shaoning, G.; Ping, J.; Xinyu, S.; Gaoyang, M.; Han, W.; Yuewei, A.; Chunming, W.; Chu, H.; Rong, C.; Wei, L.: Comparison of solidification cracking susceptibility between Al-Mg and Al-Cu alloys during welding: A phase-field study. Scripta Materialia 150 (2018), pp. 120–124.

SING ET AL. 2021

Sing, S. L.; Huang, S.; Goh, G. D.; Goh, G. L.; Tey, C. F.; Tan, J.; Yeong, W. Y.: Emerging metallic systems for additive manufacturing: In-situ alloying and multi-metal processing in laser powder bed fusion. Progress in Materials Science 119 (2021), p. 100795.

SKELTON ET AL. 2022
Skelton, J. M.; Sullivan, E. J.; Fitz-Gerald, J. M.; Floro, J. A.: Efficacy of elemental mixing of in situ alloyed Al-33wt%Cu during laser powder bed fusion. Journal of Materials Processing Technology 299 (2022), p. 117379.

SONAWANE ET AL. 2021
Sonawane, A.; Roux, G.; Blandin, J.-J.; Despres, A.; Martin, G.: Cracking mechanism and its sensitivity to processing conditions during laser powder bed fusion of a structural aluminum alloy. Materialia 15 (2021), p. 100976.

SONG ET AL. 2017
Song, L.; Wang, F.; Li, S.; Han, X.: Phase congruency melt pool edge extraction for laser additive manufacturing. Journal of Materials Processing Technology 250 (2017), pp. 261–269.

SORKIN ET AL. 2017
Sorkin, A.; Tan, J. L.; Wong, C. H.: Multi-material modelling for selective laser melting. Procedia Engineering 216 (2017), pp. 51–57.

SPIERINGS ET AL. 2017
Spierings, A. B.; Dawson, K.; Heeling, T.; Uggowitzer, P. J.; Schäublin, R.; Palm, F.; Wegener, K.: Microstructural features of Sc- and Zr-modified Al-Mg alloys processed by selective laser melting. Materials & Design 115 (2017), pp. 52–63.

SUN ET AL. 2020
Sun, Z.; Chueh, Y.; Li, L.: Multiphase mesoscopic simulation of multiple and functionally gradient materials laser powder bed fusion additive manufacturing processes. Additive Manufacturing 35 (2020), p. 101448.

TANG ET AL. 2022
Tang, C.; Yao, L.; Du, H.: Computational framework for the simulation of multi material laser powder bed fusion. International Journal of Heat and Mass Transfer 191 (2022), p. 122855.

TOLOCHKO ET AL. 2004
Tolochko, N. K.; Mozzharov, S. E.; Yadroitsev, I. A.; Laoui, T.; Froyen, L.; Titov, V. I.; Ignatiev, M. B.: Balling processes during selective laser treatment of powders. Rapid Prototyping Journal 10 (2004) 2, pp. 78–87.

VALLABH ET AL. 2022
Vallabh, C. K.; Sridar, S.; Xiong, W.; Zhao, X.: Predicting melt pool depth and grain length using multiple signatures from in-situ single camera two-wavelength imaging pyrometry for laser powder bed fusion. Journal of Materials Processing Technology 308 (2022), p. 117724.

VAVILOV 2020
Vavilov, V.: Infrared Thermography and Thermal Nondestructive Testing. Cham: Springer International Publishing AG 2020. ISBN: 9783030480028.

WANG ET AL. 2004
Wang, N.; Mokadem, S.; Rappaz, M.; Kurz, W.: Solidification cracking of superalloy single- and bi-crystals. Acta Materialia 52 (2004) 11, pp. 3173–3182.

WANG ET AL. 2018
Wang, P.; Deng, L.; Prashanth, K. G.; Pauly, S.; Eckert, J.; Scudino, S.: Microstructure and mechanical properties of Al-Cu alloys fabricated by selective laser melting of powder mixtures. Journal of Alloys and Compounds 735 (2018), pp. 2263–2266.

WANG ET AL. 2019
Wang, D.; Wang, Z.; Li, K.; Ma, J.; Liu, W.; Shen, Z.: Cracking in laser additively manufactured W: Initiation mechanism and a suppression approach by alloying. Materials & Design 162 (2019), pp. 384–393.

WANG ET AL. 2020
Wang, R.; Gu, D.; Chen, C.; Dai, D.; Ma, C.; Zhang, H.: Formation mechanisms of TiB2 tracks on Ti6Al4V alloy during selective laser melting of ceramic-metal multi-material. Powder Technology 367 (2020), pp. 597–607.

WANG ET AL. 2022a
Wang, R.; Garcia, D.; Kamath, R. R.; Dou, C.; Ma, X.; Shen, B.; Choo, H.; Fezzaa, K.; Yu, H. Z.; Kong, Z. J.: In situ melt pool measurements for laser powder bed fusion using multi sensing and correlation analysis. Scientific Reports 12 (2022) 1, pp. 1–17.

WANG ET AL. 2022b
Wang, H.; Gould, B.; Haddad, M.; Moorehead, M.; Couet, A.; Wolff, S. J.: In situ high-speed synchrotron X-ray imaging of laser-based directed energy deposition of the alloying process with dissimilar powders. Journal of Manufacturing Processes 75 (2022), pp. 1003–1011.

WARRINGTON & MCCARTNEY 1989
Warrington, D.; Mccartney, D. G.: Development of a New Hot-cracking Test for Aluminium Alloys. Cast Metals 2 (1989) 3, pp. 134–143.

WEI & LI 2021
Wei, C.; Li, L.: Recent progress and scientific challenges in multi-material additive manufacturing via laser-based powder bed fusion. Virtual and Physical Prototyping 16 (2021) 3, pp. 347–371.

WEINGARTEN ET AL. 2015
Weingarten, C.; Buchbinder, D.; Pirch, N.; Meiners, W.; Wissenbach, K.; Poprawe, R.: Formation and reduction of hydrogen porosity during selective laser melting of AlSi10Mg. Journal of Materials Processing Technology 221 (2015), pp. 112–120.

WEIRATHER ET AL. 2019
Weirather, J.; Rozov, V.; Wille, M.; Schuler, P.; Seidel, C.; Adams, N. A.; Zaeh, M. F.: A Smoothed Particle Hydrodynamics Model for Laser Beam Melting of Ni-based Alloy 718. Computers & Mathematics with Applications 78 (2019) 7, pp. 2377–2394.

WEIRATHER 2023
Weirather, J.: Prozesssimulation des Laserstrahlschmelzens mit der Smoothed-Particle-Hydrodynamics-Methode. Dissertation. TECHNISCHE UNIVERSITÄT MÜNCHEN. München (2023).

WIMMER ET AL. 2020a
Wimmer, A.; Kolb, C. G.; Assi, M.; Favre, J.; Bachmann, A.; Fraczkiewicz, A.; Zaeh, M. F.: Investigations on the influence of adapted metal-based alloys on the process of laser beam melting. Journal of Laser Applications 32 (2020) 2, p. 22029.

WIMMER ET AL. 2020b
Wimmer, A.; Lehmann, M.; Schuler, A.; Zaeh, M. F.: Analysis of the phase transformation of AlSi10Mg during Laser Powder Bed Fusion. Procedia CIRP 94 (2020), pp. 177–181.

WIMMER ET AL. 2021
Wimmer, A.; Yalvac, B.; Zoeller, C.; Hofstaetter, F.; Adami, S.; Adams, N. A.; Zaeh, M. F.: Experimental and Numerical Investigations of In Situ Alloying during Powder Bed Fusion of Metals Using a Laser Beam. Metals 11 (2021) 11, p. 1842.

WIMMER ET AL. 2022
Wimmer, A.; Hofstaetter, F.; Jugert, C.; Wudy, K.; Zaeh, M. F.: In situ alloying: investigation of the melt pool stability during powder bed fusion of metals using a laser beam in a novel experimental set-up. Progress in Additive Manufacturing 7 (2022) 2, pp. 351–359.

WIMMER ET AL. 2023
Wimmer, A.; Panzer, H.; Zoeller, C.; Adami, S.; Adams, N. A.; Zaeh, M. F.: Experimental and Numerical Investigations of the Hot Cracking Susceptibility during the Powder Bed Fusion of AA 7075 using a Laser Beam. Progress in Additive Manufacturing (2023).

WOHLERS ET AL. 2020
Wohlers, T.; Campbell, R. I.; Diegel, O.; Huff, R.; Kowen, J.: Wohlers report 2020. 3D printing and additive manufacturing state of the industry. Fort Collins, Colo.: Wohlers Associates 2020. ISBN: 9780991333264.

WOLF ET AL. 2005
Wolf, M.; Schobbert, H.; Böllinghaus, T.: Influence of the Weld Pool Geometry on Solidification Crack Formation. In: Böllinghaus, T. et al. (Eds.): Hot Cracking Phenomena in Welds. Berlin: Springer 2005, pp. 245–268. ISBN: 978-3-540-27460-5.

WU ET AL. 2022
Wu, S.; Lei, Z.; Li, B.; Liang, J.; Chen, Y.: Hot cracking evolution and formation mechanism in 2195 Al-Li alloy printed by laser powder bed fusion. Additive Manufacturing 54 (2022), p. 102762.

YADROITSEV ET AL. 2021. Yadroitsev, I.; Yadroitsava, I.; Du Plessis, A.; MacDonald, E.: Fundamentals of Laser Powder Bed Fusion of Metals : Additive Manufacturing

Materials and Technologies. Amsterdam, The Netherlands: Elsevier 2021. ISBN: 978-0-12-824090-8.

YANG & EVANS 2004
Yang, S.; Evans, J. R.: A multi-component powder dispensing system for three dimensional functional gradients. Materials Science and Engineering: A 379 (2004) 1, pp. 351–359.

ZHANG ET AL. 2017
Zhang, H.; Zhu, H.; Nie, X.; Yin, J.; Hu, Z.; Zeng, X.: Effect of Zirconium addition on crack, microstructure and mechanical behavior of selective laser melted Al-Cu-Mg alloy. Scripta Materialia 134 (2017), pp. 6–10.

ZHANG ET AL. 2019
Zhang, B.; Liu, S.; Shin, Y. C.: In-Process monitoring of porosity during laser additive manufacturing process. Additive Manufacturing 28 (2019), pp. 497–505.

ZHANG ET AL. 2020
Zhang, X.; Chueh, Y.; Wei, C.; Sun, Z.; Yan, J.; Li, L.: Additive manufacturing of three-dimensional metal-glass functionally gradient material components by laser powder bed fusion with in situ powder mixing. Additive Manufacturing 33 (2020), p. 101113.

ZHANG ET AL. 2021a
Zhang, C.; Rezavand, M.; Zhu, Y.; Yu, Y.; Wu, D.; Zhang, W.; Wang, J.; Hu, X.: SPHinXsys: An open-source multi-physics and multi-resolution library based on smoothed particle hydrodynamics. Computer Physics Communications 267 (2021), p. 108066.

ZHANG ET AL. 2021b
Zhang, P.; Jia, Z.; Yu, Z.; Shi, H.; Li, S.; Di Wu; Yan, H.; Ye, X.; Chen, J.; Wang, F.; Tian, Y.: A review on the effect of laser pulse shaping on the microstructure and hot cracking behavior in the welding of alloys. Optics & Laser Technology 140 (2021), p. 107094.

ZHAO ET AL. 2017
Zhao, C.; Fezzaa, K.; Cunningham, R. W.; Wen, H.; Carlo, F.; Chen, L.; Rollett, A. D.; Sun, T.: Real-time monitoring of laser powder bed fusion process using high-speed X-ray imaging and diffraction. Scientific Reports 7 (2017) 1, p. 3602.

ZHENG ET AL. 2019
Zheng, L.; Zhang, Q.; Cao, H.; Wu, W.; Ma, H.; Ding, X.; Yang, J.; Duan, X.; Fan, S.: Melt pool boundary extraction and its width prediction from infrared images in selective laser melting. Materials & Design 183 (2019), p. 108110.

ZHOU ET AL. 2020a
Zhou, B.; Lu, S.; Xu, K.; Xu, C.; Wang, Z.; Wang, B.: Hot cracking tendency test and simulation of 7075 semi-solid aluminium alloy. Transactions of Nonferrous Metals Society of China 30 (2020) 2, pp. 318–332.

ZHOU ET AL. 2020b

Zhou, S. Y.; Su, Y.; Wang, H.; Enz, J.; Ebel, T.; Yan, M.: Selective laser melting additive manufacturing of 7xxx series Al-Zn-Mg-Cu alloy: Cracking elimination by co-incorporation of Si and TiB2. Additive Manufacturing 36 (2020), p. 101458.

Appendix

A. List of supervised student research projects

In the context of this dissertation, various student research projects (see Table A.1) were intensively supervised with regard to the methodology, problem statements, objectives, and the approach, along with the interpretation and documentation of the results. The supervision took place at the *iwb* of the TUM. The findings and results of the student research projects listed below have contributed to this dissertation. The author would like to express his sincere gratitude for the remarkable commitment of all supervised students and their interesting and important contributions.

Table A.1: Summary of supervised student research projects

Name of the student	Title and date of the student research project
Mannhardt, F.	German (original): Schmelzbaduntersuchungen beim Laserstrahl-schmelzen mittels optischer Kohärenztomographie English: Melt pool investigations in laser beam melting by optical coherence tomography, submitted in June 2019
Jugert, C. A.	German (original): Analyse des Laser-Strahlschmelzprozesses mittels einer Hochgeschwindigkeits-Kamera sowie metallographischen Untersuchungen English: Analysis of the laser beam melting process using a high-speed camera and metallographic investigations, submitted in March 2021
Panzer, H.	English (original): Characterization of micro crack formation during the PBF-LB/M process by means of SPH, submitted in May 2021
Ramirez Hoenack, P. F.	English (original): Quantification of the influence of additives on the laser beam melting process, submitted in May 2021
Schuler, A.	German (original): Spritzeranalyse beim Laserstrahlschmelzen mittels Hochgeschwindigkeits-Infrarotthermographie English: Spatter analysis during laser beam melting via high-speed thermographic imaging, submitted in May 2019
Stoffels, O. A.	German (original): Entwicklung einer für den Forschungszweck angepassten Laser-Strahlschmelzanlage English: Development of a laser beam melting system adapted to the purpose of research, submitted in November 2020

Hofstaetter, F.	English (original): Designing and building of a modular laser beam melting system for in-situ process monitoring and high-speed infrared thermographic imaging, submitted in November 2019
Franz, T.	German (original): Off-axis-Prozessüberwachung beim Laser-Strahlschmelzen: Analyse von Schmelzbadeffekten mit Hilfe von Hochgeschwindigkeitsaufnahmen English: Off-axis process monitoring during laser beam melting: analysis of melt pool effects with the help of high-speed recordings, submitted in March 2019
Hansbauer, F.	German (original): Thermische Analyse der Prozesskette des Laserstrahlschmelzens English: Thermal analysis of the process chain during laser beam melting, submitted in May 2019
Hofstaetter, F.	English (original): Influence of powder additives on the laser beam melting process, submitted in December 2020
Hunyadi, P.	English (original): Simulation of the melt pool during laser beam melting, submitted in June 2020
Langhans, G.	German (original): Konzeptionierung eines Versuchsstands zur Schmelzbaduntersuchung beim Laserstrahlschmelzen English: Conceptual design of a test rig for melt pool analysis during laser beam melting, submitted in June 2020
Schuler, A.	German (original): Schmelzbadanalyse beim metallischen Laser-Strahlschmelzen mittels Hochgeschwindigkeits-Infrarotthermografie English: Melt pool analysis during metallic laser beam melting via high-speed thermographic imaging, submitted in February 2020
Yalvac, B.	English (original): Simulative representation and investigation on the influence of additives during laser beam melting, submitted in October 2020

B. Publications of the author

This section lists the publications that were embedded into this dissertation. Please note that wherever no bibliographic indices are given, the information is not available or not known to the author.

Publication 1 (P1): Wimmer, A.; Kolb, C. G.; Assi, M.; Favre, J.; Bachmann, A.; Fraczkiewicz, A.; Zaeh, M. F.: Investigations on the influence of adapted metal-based alloys on the process of laser beam melting. Journal of Laser Applications 32 (2020) 2, p. 22029.

Publication 2 (P2): Wimmer, A.; Lehmann, M.; Schuler, A.; Zaeh, M. F.: Analysis of the phase transformation of AlSi10Mg during Laser Powder Bed Fusion. Procedia CIRP 94 (2020), pp. 177–181.

Publication 3 (P3): Wimmer, A.; Hofstaetter, F.; Jugert, C.; Wudy, K.; Zaeh, M. F.: In situ alloying: investigation of the melt pool stability during powder bed fusion of metals using a laser beam in a novel experimental set-up. Progress in Additive Manufacturing 7 (2022) 2, pp. 351–359.

Publication 4 (P4): Wimmer, A.; Yalvac, B.; Zoeller, C.; Hofstaetter, F.; Adami, S.; Adams, N. A.; Zaeh, M. F.: Experimental and numerical investigations of in situ alloying during powder bed fusion of metals using a laser beam. Metals 11 (2021) 11, p. 1842.

Publication 5 (P5): Wimmer, A.; Panzer, H.; Zoeller, C.; Adami, S.; Adams, N. A.; Zaeh, M. F.: Experimental and numerical investigations of the hot cracking susceptibility during the powder bed fusion of AA 7075 using a laser beam. Progress in Additive Manufacturing (2023)